

ENERGY TRANSFER DYNAMICS AND DOPANT LUMINESCENCE IN Mn-
DOPED CdS/ZnS CORE/SHELL NANOCRYSTALS

A Dissertation

by

HSIANG-YUN CHEN

Submitted to the Office of Graduate Studies of
Texas A&M University
in partial fulfillment of the requirements for the degree of

DOCTOR OF PHILOSOPHY

Approved by:

| | |
|---------------------|----------------------|
| Chair of Committee, | Dong Hee Son |
| Committee Members, | Timothy R. Hughbanks |
| | Simon W. North |
| | Joseph H. Ross |
| Head of Department, | David H. Russell |

December 2012

Major Subject: Chemistry

Copyright 2012 Hsiang-Yun Chen

ABSTRACT

Mn-doped II-VI semiconductor nanocrystals exhibit bright dopant photoluminescence that has potential usefulness for light emitting devices, temperature sensing, and biological imaging. The bright luminescence comes from the ${}^4T_1 \rightarrow {}^6A_1$ transition of the Mn^{2+} d electrons after the exciton-dopant energy transfer, which reroutes the exciton relaxation through trapping processes. The driving force of the energy transfer is the strong exchange coupling between the exciton and Mn^{2+} due to the confinement of exciton in the nanocrystal. The exciton-Mn spatial overlap affecting the exchange coupling strength is an important parameter that varies the energy transfer rate and the quantum yield of Mn luminescence. In this dissertation, this correlation is studied in radial doping location-controlled Mn-doped CdS/ZnS nanocrystals. Energy transfer rate was found decreasing when increasing the doping radius in the nanocrystals at the same core size and shell thickness and when increasing the size of the nanocrystals at a fixed doping radius.

In addition to the exciton-Mn energy transfer discussed above, two consecutive exciton-Mn energy transfers can also occur if multiple excitons are generated before the relaxation of Mn (lifetime $\sim 10^{-4}$ - 10^{-2} s). The consecutive exciton-Mn energy transfer can further excite the Mn^{2+} d electrons high in conduction band and results in the quenching of Mn luminescence. The highly excited electrons show higher photocatalytic efficiency than the electrons in undoped nanocrystals.

Finally, the effect of local lattice strain on the local vibrational frequency and local thermal expansion was observed via the temperature-dependent Mn luminescence spectral linewidth and peak position in Mn-doped CdS/ZnS nanocrystals. The local lattice strain on the Mn^{2+} ions is varied using the large core/shell lattice mismatch ($\sim 7\%$) that creates a gradient of lattice strain at various radial locations. When doping the Mn^{2+} closer to the core/shell interface, the stronger lattice strain softens the vibrational frequency coupled to the ${}^4\text{T}_1 \rightarrow {}^6\text{A}_1$ transition of Mn^{2+} (Mn luminescence) by $\sim 50\%$. In addition, the lattice strain also increases the anharmonicity, resulting in larger local thermal expansion observed from the nearly an order larger thermal shift of the Mn luminescence compared to the Mn-doped ZnS nanocrystals without the core/shell lattice mismatch.

To my family

ACKNOWLEDGEMENTS

I would like to thank my advisor, Dr. Son, for his guidance, care, patience, and trust. He not only teaches us the way and the attitude to do research, but also guides us according to our individual situation and helps us rectify problems. He makes sure everyone has constant progress, so we never have to worry about not learning or not having anything done. I truly appreciate his patience—that he gave me time to improve myself. Thanks to him, after five years, I can proudly call myself a chemist.

I would also like to thank my committee members, Dr. Hughbanks, Dr. Goodman, Dr. Ross, and Dr. North, for their advice. Dr. Hughbanks is a knowledgeable teacher, and he gave me directions to find the answers on my research. Dr. Goodman and Dr. Ross helped me think more deeply on my proposed research. Dr. North is nice that he agreed to join my advisory committee at the last stage. Dr. Hughbanks and Dr. North also helped me correct a mis-posted grade that bothered me for a long time.

I also want to thank the Department of Chemistry, Texas A&M University for giving me the opportunity to be a graduate student. The departmental staff is very helpful and responsible so that I can focus on my study. The university writing center is also very helpful. I acquired help from it on and off during the time at A&M. I am thankful to my consultants, Brandie and Lauren, who helped me correct the problems and improve the completeness of my dissertation.

I appreciate our collaborators, Cory Nelson and Prof. Xiaoyang Zhu at Department of Chemistry, University of Texas, Austin. Thanks for their help with the

temperature-dependent Mn luminescence measurement, we can complete the data acquisition and publish the results. I also want to thank Liang Yin and Prof. Choongho Yu at Department of Mechanical Engineering, Texas A&M University, and Tzu-Hao Jen and my father, Prof. Show-An Chen, at Department of Chemical Engineering, National Tsing Hua University, Taiwan for helping and allowing me to use their instruments for the initial testing.

I am grateful for my seniors and juniors in our lab for all the good and difficult times we have shared. Tai-Yen is a wonderful mentor who patiently and unselfishly taught and helped me everything about the laser and data analysis. He pointed out how I could improve my research and was hard on me with just the right amount. Chih-Hao trained and advised me on everything in the synthesis and characterization of nanocrystals, so that I had the capability to make the samples for my research. His efforts also make all the chemistry going on in this lab possible. Stacey was extremely helpful on everyone's presentation. She would volunteer to check if I needed help and showed me how to organize and explain the contents better. Erick helped me pass through the most difficult summer. He also taught me to think outside the box and never be limited by what we don't have. Create it using anything reachable, even with a bookshelf. Yerok was like a big brother. He checks if we are fine. His active attitude in making things happen inspires me to be positive when facing the obstacles. Sourav ran uncountable hours of laser experiment with me when we were hungry and cold. The discussion we had during these long hours of experiments became very useful in

explaining the results and also motivated ideas for the new project. Thanks to these great people, I enjoyed the time here.

I also want to thank my boyfriend Tzu-Pin for the mental support. He made me feel everything will be fine and gave me the power to keep moving.

Finally, I want to thank my father, mother, and my sister for their expectation, understanding, and forgiveness of me. My parents gave me the best education and environment to grow up. They pushed me to achieve more than what I thought I could, so that I have the opportunity to be here. My sister has great courage and will to achieve what many people do not even dare to try, despite of all the unimaginable difficulties she has been through. She makes me realize that all my obstacles are nothing. I can always try harder, and I should thank how lucky I am.

NOMENCLATURE

| | |
|---------------------------------|---|
| $\langle n_{\text{Mn}} \rangle$ | Average number of Mn^{2+} ions per nanocrystals |
| $\langle n_{\text{ex}} \rangle$ | Average number of excitons generated per pulse per nanocrystals |
| τ_{ET} | Energy transfer time |
| τ_{tr} | Hole trapping time |
| τ_{Mn} | Mn luminescence lifetime |
| d | Radial doping location of the Mn^{2+} ions, or the distance between the core/shell interface and the Mn^{2+} ions |
| EPR | Electron paramagnetic resonance |
| ODE | 1-Octadecene |
| OAm | Oleylamine |

TABLE OF CONTENTS

| | Page |
|---|------|
| ABSTRACT | ii |
| DEDICATION | iv |
| ACKNOWLEDGEMENTS | v |
| NOMENCLATURE..... | viii |
| TABLE OF CONTENTS | ix |
| LIST OF FIGURES..... | xii |
| LIST OF TABLES | xix |
| CHAPTER | |
| I INTRODUCTION..... | 1 |
| II BACKGROUND AND LITERATURE OVERVIEW | 5 |
| 2.1 Electronic Structure of II-VI Semiconductor Nanocrystals and the Exciton Dynamics..... | 5 |
| 2.2 Doped II-VI Semiconductor Nanocrystals..... | 8 |
| 2.3 Mechanism of Energy Transfer and the Measurement of Energy Transfer Dynamics | 20 |
| III SYNTHESIS OF Mn-DOPED NANOCRYSTALS AND EXPERIMENTAL METHODS..... | 30 |
| 3.1 Synthesis of Nanocrystals | 30 |
| 3.2 Absorption and Luminescence Spectra Measurement | 42 |
| 3.3 Time-Dependent Mn Luminescence Intensity Measurement .. | 44 |
| 3.4 Determination of Radial Doping Location in Mn- Doped CdS/ZnS Nanocrystals..... | 44 |
| 3.5 Determination of the Doping Concentration and Extinction Coefficient | 48 |
| 3.6 Crystal Structure of the Nanocrystals..... | 49 |
| 3.7 Transient Absorption Measurement | 50 |

| CHAPTER | Page |
|--|------|
| 3.8 Calculation of Excitation Density | 52 |
| IV MEASUREMENT OF ENERGY TRANSFER TIME IN COLLOIDAL Mn-DOPED SEMICONDUCTOR NANOCRYSTALS | 55 |
| 4.1 Introduction | 55 |
| 4.2 Results and Discussion..... | 58 |
| 4.3 Conclusions | 70 |
| 4.4 Experimental Section | 71 |
| V DOPING LOCATION- AND SIZE- DEPENDENT ENERGY TRANSFER IN Mn-DOPED CdS/ZnS NANOCRYSTALS | 73 |
| 5.1 Introduction | 73 |
| 5.2 Results and Discussion..... | 76 |
| 5.3 Conclusions | 96 |
| 5.4 Experimental Section | 97 |
| VI HOT ELECTRONS FROM CONSECUTIVE EXCITON- Mn ENERGY TRANSFER IN Mn-DOPED SEMICONDUCTOR NANOCRYSTALS..... | 98 |
| 6.1 Introduction | 98 |
| 6.2 Results and Discussion..... | 100 |
| 6.3 Conclusions | 112 |
| 6.4 Experimental Section | 113 |
| VII CONTROLLED LOCAL LATTICE STRAIN TUNES TEMPERATURE DEPENDENCE OF Mn LUMINESCENCE IN Mn-DOPED CORE/SHELL CdS/ZnS NANOCRYSTALS | 117 |
| 7.1 Introduction | 117 |
| 7.2 Results and Discussion..... | 119 |
| 7.3 Conclusion..... | 134 |
| 7.4 Experimental Section | 134 |
| VIII SUMMARY | 141 |
| 8.1 Exciton-Mn Energy Transfer Dynamics | 141 |

| | |
|--|-------|
| | Rci g |
| | |
| 8.2 Hole Trapping Dynamics | 142 |
| 8.3 Hot Electron Generated after Multiple Exciton-Mn Energy Transfer | 143 |
| 8.4 Strain Effect on the Temperature-Dependence of Mn Luminescence Spectrum | 144 |
| 8.5 Future Works..... | 144 |
| REFERENCES..... | 147 |
| APPENDIX A | 158 |

LIST OF FIGURES

| | | Page |
|----------|--|------|
| Figure 1 | (Left) Absorption (black) and emission (gray) spectra of CdSe nanocrystals and (right) the corresponding state-to-state electronic transition. (Reprint with permission from Sewall, S. L.; Cooney, R. R.; Anderson, K. E. H.; Dias, E. A.; Kambhampati, P. <i>Phys. Rev. B</i> 2006 , <i>74</i> , 235328. Copyright 2006 American Physical Society) ⁴⁰ | 6 |
| Figure 2 | Chemical synthesis methods of colloidal doped semiconductor nanocrystals. | 10 |
| Figure 3 | (a) Exciton relaxation pathways in undoped nanocrystals. (b) Energy transfer between exciton and dopant state in Mn-doped nanocrystals and resulting sensitized Mn luminescence. (c) Hole trapping followed by radiative charge carrier recombination in Cu-doped semiconductor nanocrystals. | 14 |
| Figure 4 | Energy level diagram of Mn-doped nanocrystals and photograph of photoluminescence from undoped (top right) and Mn-doped CdS/ZnS (bottom right) nanocrystals. | 17 |
| Figure 5 | Relevant processes to energy transfer occur from (1) to (5). $ \varphi_d\rangle$ and $ \varphi_d'\rangle$ are the donor ground and excited states, respectively. $ \varphi_a\rangle$ and $ \varphi_a'\rangle$ are the acceptor ground and excited states, respectively. The crosses indicate the states of the donor and the acceptor. The arrows indicate the change of states described at the top of each sub-figure..... | 21 |
| Figure 6 | (a) Spectral overlap between donor absorption and acceptor emission spectrum, $g_D(E)$ and $g_A(E)$, respectively. (b) Illustration of spatial correlation between donor nucleus (D), acceptor nucleus (A), donor electron (i), and acceptor electron (j). ⁸⁶ | 22 |
| Figure 7 | (a) Dynamics of band-edge bleach recovery in Mn-doped CdS/ZnS core/shell nanocrystals with varying doping concentrations ($\langle n_{Mn} \rangle$) and a fixed radial doping location. (b) The linear correlation of the energy transfer rate extracted from (a) on Mn doping concentration. | 27 |
| Figure 8 | Absorption (solid) and luminescence (dashed) spectra of (a) CdS and (b) CdSe nanocrystals. The gray dashed line indicates the zero intensity. The luminescence spectra were taken using a CCD | |

| | Page |
|---|------|
| spectrometer (USB 2000, Ocean Optics) without intensity calibration. A 370 nm light emitting diode was used as the excitation light source. . | 32 |
| Figure 9 Absorption spectra of Mn-doped CdS/ZnS nanocrystals with (sample 1, solid) and without (sample 2, dashed) Ostwald ripening with the same CdS core, the amount of Mn, and the amount of ZnS precursor. The gray dashed line indicates 0 absorbance. | 37 |
| Figure 10 Absorption and luminescence (peaked at ~440 nm) spectra of the undoped CdS/ZnS nanocrystals with core size and shell thickness of 3.6 and ~1.8 nm, respectively. The luminescence spectra were taken using a CCD spectrometer (USB2000, Ocean Optics) without intensity calibration using a 370 nm light emitting diode as the excitation light source. The sample codes in the legends correspond to the synthesis conditions summarized in Table 1. The gray dashed line indicates 0 absorbance. | 42 |
| Figure 11 TEM images of (a) CdS core and (b) and (c) CdS/ZnS nanocrystals before doping Mn ²⁺ ions for doping locations $d = 0.6$ and 1.2 nm, respectively. Scale bar is the same for all three images. | 47 |
| Figure 12 Absorption spectra of CdS core, CdS/ZnS nanocrystals before doping the Mn ²⁺ ions), final Mn-doped CdS/ZnS nanocrystals. (a) and (b) are for doping location $d = 0.6, 1.2$ nm, respectively. Spectra are normalized to the same nanocrystal concentration. | 47 |
| Figure 13 Comparison of x-ray diffraction patterns of (b) CdS nanocrystals and (c) undoped and (d), (e) Mn-doped CdS/ZnS nanocrystals with Mn ²⁺ ions doped at the core/shell interface. Bulk (a) CdS and (f) ZnS from database. | 50 |
| Figure 14 Experimental setup of the transient absorption measurement. BS: beam splitter, HWP: half waveplate, L: lens, P: polarizer, PD: photodiode, PS: prism, and β -BBO: beta-barium borate crystal. The solid and dashed lines are the pump and probe beams, respectively. | 52 |
| Figure 15 Estimation of pump fluence using 2D Gaussian profile. | 54 |
| Figure 16 (a) TEM images of Mn-doped CdS/ZnS nanocrystals. (b) Dimensions of Mn-doped CdS/ZnS core/shell nanocrystals. CdS core radius and ZnS shell thickness is 1.8 nm and 0.7 nm respectively. Mn ²⁺ ions are doped at $d = 2.1$ nm. | 58 |

- Figure 17 (a) Absorption (solid) and luminescence spectra (dashed) of Mn-doped CdS/ZnS core/shell nanocrystals with different Mn doping level. The arrow indicates the pump wavelength for transient absorption measurements. (b) Time dependent Mn phosphorescence intensity following 337 nm excitation. $\langle n_{Mn} \rangle$ is labeled in the figure. 59
- Figure 18 Transient absorption data for (a) undoped and (b) Mn-doped ($\langle n_{Mn} \rangle = 7.7$) CdS/ZnS core/shell nanocrystals measured with pump wavelength 390 nm at $\langle n_{Mn} \rangle = 24$ and probe at 700 - 880 nm as indicated in the legend. The data probed at 700 - 880 nm shows similar decaying feature, indicating the induced absorption signal is independent of probing wavelength in this spectral region. 61
- Figure 19 Transient absorption data of undoped CdS/ZnS core/shell nanocrystals under various exciton densities ($\langle n_{ex} \rangle$) obtained with 390 nm pump and 880 nm probe. The inset displays the peak amplitude of ΔOD data vs. $\langle n_{ex} \rangle$ 62
- Figure 20 (a) Transient absorption data of undoped and Mn-doped CdS/ZnS nanocrystals obtained with 390 nm pump and 880 nm probe at $\langle n_{ex} \rangle = 1$. Experimental data (symbol) and fit to exponential functions (solid line). (b) $\Delta\Delta OD$ data of $\langle n_{Mn} \rangle = 5.1$ and 22 samples. 64
- Figure 21 Transient absorption data of Mn-doped CdS/ZnS core/shell nanocrystals measured with pump wavelength 390 nm at $\langle n_{ex} \rangle = 1$ and probe wavelength 455 nm, which is slightly longer than the band edge absorption. $\langle n_{Mn} \rangle$ is shown in the legend. The bleach signal at zero time delay was partially canceled by an absorptive component, especially in the sample with a high level of Mn doping. 64
- Figure 22 (a) Kinetic scheme used for modeling of energy transfer competing with radiative and nonradiative relaxation (trapping) of exciton in Mn-doped CdS/ZnS nanocrystals. [gs], [ex] and [ex_{tr}] represent ground state, excited state (exciton), and trapped excited state (trapped exciton). The fitting parameters are τ_{ET} , τ_{tr} and σ_r . See the text. (b) Experimental data (symbol) and fit (solid line) of the data to the kinetic model. 67
- Figure 23 Transient absorption data of undoped and Mn-doped CdS/ZnS core/shell nanocrystals with $\langle n_{ex} \rangle = 14$. Experimental data (symbol) and fit (solid lines) are shown for $\langle n_{Mn} \rangle = 0$ (circle) and 22 (triangle).

| | Page |
|---|------|
| The time constants τ_1 and τ_2 were obtained from multi exponential fitting of the data. | 69 |
| Figure 24 Transient absorption data for CdS/ZnS core/shell nanocrystals doped with various $\langle n_{Mn} \rangle$ (as indicated in the legend) measured with pump/probe wavelength 390/880 nm at $\langle n_{ex} \rangle = 14$ and 22 ((a) and (b)). The early signal decays faster as $\langle n_{Mn} \rangle$ increases, indicating the exciton to Mn^{2+} energy transfer effectively competes with Auger recombination process even at high excitation density. | 70 |
| Figure 25 (a) TEM of typical Mn-doped CdS/ZnS nanocrystals. (b) Schematic diagram of the structure of the Mn-doped CdS/ZnS nanocrystals and exciton wavefunction distribution. d is the radial doping location of Mn^{2+} ions (yellow dots). VB and CB are valence and conduction band. | 77 |
| Figure 26 Absorption (solid) and photoluminescence (dashed) spectra of undoped and Mn-doped CdS/ZnS nanocrystals with different doping location (d) with $\langle n_{Mn} \rangle = \sim 6$. a1 , b1 , c1 are for $d = 0, 0.6, 1.2$ nm, respectively. | 79 |
| Figure 27 (a) - (c) Bleach recovery probed at 420 nm and (d) - (f) induced absorption probed at 880 nm of undoped and Mn-doped CdS/ZnS nanocrystals of varying doping locations and densities. Doping location $d = 0, 0.6, 1.2$ nm are labeled as a , b , c , respectively. Each panel compares the samples belonging to the same doping concentration group as noted on top of each column. | 80 |
| Figure 28 Photophysical processes following the excitation of exciton in Mn-doped semiconductor nanocrystals. CB and VB are conduction and valence band. Dashed lines within the gap represent trap states. | 81 |
| Figure 29 Comparison of the normalized $ \Delta OD $ data probed at 420 (solid) and 880 nm (dashed). | 82 |
| Figure 30 Comparison of transient absorption data (dots) and the fits (lines) to time window of 750 ps. (a)-(c) Bleach recovery probed at 420 nm and (d)-(f) induced absorption probed at 880 nm of undoped and Mn-doped CdS/ZnS nanocrystals of varying doping locations and densities. Doping location $d = 0, 0.6, 1.2$ nm are labeled as a , b , c , respectively. Each panel compares the samples belonging to the same doping concentration group as noted on top of each column. | 84 |

| | Page |
|---|------|
| Figure 31 Doping location-dependent energy transfer rate constant ($1/\tau_{ET}$). The solid lines are trend lines assuming the energy transfer rate is linear to the average Mn doping concentration. | 89 |
| Figure 32 Bleach recovery of undoped (dashed) and Mn-doped (solid) CdSe/ZnS nanocrystals at 590 nm. | 93 |
| Figure 33 (a) TEM images of the Mn-doped CdS/ZnS nanocrystals with different core radius, 1.8 and 2.5 nm for small and large nanocrystals. Doping radii and concentrations are identical in the two nanocrystals. (b) UV-Vis absorption spectra of the two Mn-doped nanocrystals in (a). | 94 |
| Figure 34 (a), (b) Comparison of the dynamics of band-edge bleach recovery in undoped and doped nanocrystals of small and large core sizes. (c) Normalized $\Delta\Delta OD$ data obtained by subtracting the slow-recovery component ($\sim ns$) from the data of Mn-doped nanocrystals. | 96 |
| Figure 35 Absorption (solid) and luminescence (dashed) spectra of undoped and Mn-doped CdS/ZnS nanocrystals. Excitation wavelength is 370 nm. | 101 |
| Figure 36 Possible pathways for hot electron excitation in Mn-doped CdS/ZnS nanocrystals (a) Hot electron excitation via two consecutive exciton-Mn energy transfer process in Mn-doped CdS/ZnS semiconductor nanocrystals. (b) Hot electron excitation via exciton-Mn energy transfer followed by a direct resonant excitation of 4T_1 ligand field state of Mn^{2+} ion. VB and CB are valence and conduction band respectively. Thick downward arrows in orange color indicate Mn luminescence. The lifetime of 4T_1 state is 5 ms. | 102 |
| Figure 37 Excitation density-dependent luminescence of undoped and Mn-doped CdS/ZnS core/shell nanocrystals. The lines are the visual guidance. The inset compares the Mn luminescence decay curves at the excitation density of 2.5, 5 and 15 photons/particle. | 105 |
| Figure 38 Excitation density-dependent luminescence intensity of Mn-doped and undoped nanocrystals under one-pulse (solid) and two-pulse (dashed) excitation. For the two-pulse excitation, the pulses are separated by 200 ps. The lines are the visual guidance. | 108 |
| Figure 39 Photocatalytic reduction of MB in undoped (square) and Mn-doped (circle) solution under (a) 760 and (b) 1.2 mW/cm ² 405 nm cw excitation. The solid lines are the visual guidance. The dashed lines are the initial absorbance of MB. | 111 |

- Figure 40 (a) Experimental setup for the measurement of excitation density-dependent luminescence intensity. L, M, W, and F are lens, dielectric mirror, wedge beam splitter, and filter respectively. (b) 2-dimensional intensity profile of the excitation pulse at a low excitation fluence. The top and right panels compare the line profiles of the excitation (solid) and Mn luminescence intensities (dashed) in two directions indicated with the dashed line. 114
- Figure 41 (a) Schematic diagram of the structure of the Mn-doped CdS/ZnS nanocrystals. d is the distance between the core/shell interface and the Mn^{2+} ions (yellow dots). (b) Strain profile of the CdS/ZnS core/shell nanocrystal with core radius and shell thickness of 1.8 and 1.8 nm, respectively. 121
- Figure 42 Temperature-dependent Mn luminescence spectra of Mn-doped CdS/ZnS nanocrystals with varying radial doping locations (d) and doping concentrations ($\langle n_{\text{Mn}} \rangle$). Different doping locations are labeled as **a**, **b**, and **c** for $d = 0, 2$ and 4 monolayers (ML) of ZnS above the core/shell interface, respectively. Different doping concentrations are labeled as **1** and **3** for $\langle n_{\text{Mn}} \rangle = \sim 6$ and ~ 22 , respectively. 123
- Figure 43 Temperature-dependent Mn luminescence spectral lineshape of Mn-doped CdS/ZnS nanocrystals with varying radial doping locations (d) and doping concentrations ($\langle n_{\text{Mn}} \rangle$). Different doping locations are labeled as **a**, **b**, and **c** for $d = 0, 2$ and 4 monolayers (ML) of ZnS above the core/shell interface, respectively. Different doping concentrations are labeled as **1** and **3** for $\langle n_{\text{Mn}} \rangle = \sim 6$ and ~ 22 , respectively. 124
- Figure 44 (a), (b) Temperature-dependent Mn luminescence bandwidth, $\Gamma(T)$, for $\langle n_{\text{Mn}} \rangle = \sim 6$ and ~ 22 , respectively. (c), (d) Temperature dependence of $\Gamma(T)/\Gamma(5 \text{ K})$ for $\langle n_{\text{Mn}} \rangle = \sim 6$ and ~ 22 with the same color code as (a) and (b), respectively. Dots and lines are experimental data and the fit to $[\coth(\hbar\omega/2kT)]^{1/2}$, respectively. Error bars are indicated only in (a) and (b). 127
- Figure 45 (a), (b) Temperature-dependent relative Mn luminescence 0-0 transition energy (ΔE_{0-0}) for $\langle n_{\text{Mn}} \rangle = \sim 6$ and ~ 22 , respectively. ΔE_{0-0} for Mn-doped ZnS has is also shown in (b). The curves are the visual guidance only. 131

| | Page |
|---|------|
| Figure 46 Comparison of Mn luminescence spectra taken at 90 K (right and narrow peaks in each panel except for c1) and 300 K (left and broad peaks in each panel) with QE65000 (dashed) and Fluorolog 3 (solid). Excitation wavelength for all the data is 403 nm. | 136 |
| Figure 47 Comparison of Mn luminescence spectral lineshape (solid lines) and the fit (dashed lines) using eq 32. (a) and (c) are taken at 5 and 320 K of sample a1 , respectively. (b) and (d) are taken at 5 and 320 K of sample b3 , respectively. | 140 |
| Figure A1 (a), (b) Comparison of $\langle n_{\text{Mn}} \rangle$ added to the synthesis vs the $\langle n_{\text{Mn}} \rangle$ in the final Mn-doped CdS/ZnS nanocrystals for precursor A and B, respectively. | 158 |
| Figure A2 Mn luminescence lifetime vs $\langle n_{\text{Mn}} \rangle$ in Mn-doped CdS/ZnS nanocrystals. The legend indicates the number of monolayers of ZnS before/after doping the Mn^{2+} ions. | 161 |

LIST OF TABLES

| | | Page |
|-----------|---|------|
| Table 1 | Quantity of Sulfur and Zinc Precursor of Each Addition when Layering ZnS Shell..... | 40 |
| Table 2 | Radius of Core (r_{core}), CdS/ZnS before Doping (r^*) and Final Mn-Doped CdS/ZnS Nanocrystals (r_{total}). Comparison of Cation Molar Ratio ($[\text{Zn}^{2+}]/[\text{Cd}^{2+}]$) and ZnS Volume Ratios ($V_{\text{ZnS}^*}/V_{\text{ZnS}}$)..... | 47 |
| Table 3 | Exciton (Φ_{ex}) and Mn (Φ_{Mn}) Luminescence Quantum Yield and Mn Luminescence Lifetime (τ_{Mn}) of Doped CdS/ZnS Nanocrystals of Varying Doping Location (d) and Concentration ($\langle n_{\text{Mn}} \rangle$)..... | 78 |
| Table 4 | Multi-Exponential Fitting Parameters of ΔOD Data Probed at 420 nm to $-\sum r_i \cdot \exp(-t/\tau_i)$ | 84 |
| Table 5 | Multi-Exponential Fitting Parameters of ΔOD Data Probed at 880 nm to $\sum r_i \cdot \exp(-t/\tau_i)$ | 92 |
| Table 6 | Vibrational Frequency (ω) at Varying Doping Location (d) and Concentration ($\langle n_{\text{Mn}} \rangle$) from the Fit of Mn Luminescence Bandwidth vs. Temperature. | 127 |
| Table 7 | Parameters Used for the Calculation of Strain Profile. | 138 |
| Table 8 | Parameters Used for the Fit of E_{0-0} | 140 |
| Table A1. | Comparison of $\langle n_{\text{Mn}} \rangle$ Added to the Synthesis vs the $\langle n_{\text{Mn}} \rangle$ in the Final Mn-Doped CdS/ZnS Nanocrystals for Precursor A..... | 159 |
| Table A2. | Comparison of $\langle n_{\text{Mn}} \rangle$ Added to the Synthesis vs the $\langle n_{\text{Mn}} \rangle$ in the Final Mn-Doped CdS/ZnS Nanocrystals for Precursor B..... | 160 |
| Table A3. | $\langle n_{\text{Mn}} \rangle$ and Sample Structure-Dependent Mn Luminescence Lifetime in Mn-doped CdS/ZnS Nanocrystals..... | 162 |

CHAPTER I

INTRODUCTION

Transition metal doped II-VI semiconductor nanocrystals have attracted a great deal of attention due to the unique optical, electronic, and magnetic properties that are potentially useful in light emitting devices, biological imaging, and spintronics.¹⁻⁸ These properties originate from the exciton-dopant electronic coupling that is stronger than in the bulk due to the confinement of the exciton in the nanocrystals.⁸⁻¹³

The doped nanocrystals exhibit distinctively different properties compared to their undoped counterpart. For instance, the Mn-doped nanocrystals have long-lived (10^{-4} - 10^{-2} s) dopant luminescence from the *d-d* transition of the Mn^{2+} ions after the exciton-dopant energy transfer.^{6,14} The Mn luminescence intensity and wavelength is much less dependent on the surface of the nanocrystals or solvent.¹⁵ Such independence comes from the efficient exciton-dopant energy transfer that reroutes the exciton relaxation to the localized *d* electrons from trapping, the energetic and density of which strongly depend on the large surface imperfection and the type of surfactant on the nanocrystals.^{16,17} The Mn luminescence wavelength is not size-tunable like the exciton.⁴ However, the combined luminescence color of Mn and exciton may vary with temperature due to the change of relative luminescence intensity caused by the thermal energy-assisted Mn-exciton back energy transfer.^{4,18-20}

In addition, the dopants can also function as charge carrier acceptors. For example, the Cu^{2+} ions in Cu-doped nanocrystals can accept electrons from the

conduction band with the luminescence lifetime of few 10^{-7} - 10^{-6} s.^{21,23} The Cu luminescence energy is tunable by varying the band edge energy of the conduction band over the entire visible region to near-IR, depending on the material and diameter of the host nanocrystals.²¹⁻²³ Nonetheless, Cu-doped nanocrystals are relatively under-investigated because the synthesis method just became mature recently. For instance, the mechanism of the Cu luminescence has not reached agreement yet. Debates exist over whether electron-Cu²⁺ charge transfer luminescence occurs first followed by the localization of the hole to Cu⁺, or if they occur in the opposite order.²³⁻²⁵ In addition to Cu ions, Ag⁺ ions also can change the luminescence properties of the nanocrystals via donating electrons to the host. The Ag ion can either passivate the hole trap and enhance the exciton luminescence intensity or act as a hole trap and result in electron-dopant charge transfer luminescence.²⁶

In addition to energy transfer and charge transfer, the ferromagnetic coupling between the exciton and dopant spins in Mn-doped and Co-doped nanocrystals can effectively induce the formation of exciton-magnetic polaron.^{10,27-35} Due to the small size of exciton, exciton cannot migrate and has sufficient time to align the dopant spins.³³ The exciton can completely polarize the dopant spins, which is equal to the effect of tens of tesla of external magnetic field at temperature higher than that in the bulk. Partial polarization is observable even up to room temperature. The efficient formation of exciton-magnetic polaron at elevated temperature makes the Mn-doped nanocrystals promising materials for optical-magnetic device applications.

All of the above unique properties of the doped nanocrystals come from the exciton-dopant coupling that depends on their spatial wavefunction overlap. Studies on the dependence of exciton giant Zeeman effect on the exciton-Mn wavefunction overlap was achieved by varying the spatial distribution of exciton in the core/shell nanocrystal with various shell thickness.^{12,36} However, despite the large interest in using the Mn luminescence, studies on the structurally-correlated energy transfer dynamics has not been investigated. The goal of this dissertation is to study the correlation between the exciton-Mn wavefunction overlap, energy transfer rate, and dopant luminescence quantum yield. The change of exciton-dopant wavefunction overlap is achieved by changing the doping radius or the size of the nanocrystals in the radial doping location-controlled nanocrystals.³⁷ Studying the dynamics between excitons and dopants in structurally-controlled doped nanocrystals will provide valuable information to understand the exciton-dopant interaction for both fundamental and application purposes.

This dissertation is organized as follows. Chapter II briefly overviews the electronic structure and exciton-dopant energy transfer and charge transfer in undoped and doped II-VI semiconductor nanocrystals. Chapter III describes the experimental details of the synthesis, characterization, and transient absorption measurement methods of the nanocrystal samples prepared in this dissertation. Chapter IV and V discuss the effect of exciton-Mn wavefunction overlap on exciton-Mn energy transfer time by varying the doping radius at the fixed core size and shell thickness and by increasing the diameter of the nanocrystal while fixing the doping radius in Mn-doped CdS/ZnS nanocrystals. The correlation between doping radius, energy transfer yield, Mn

luminescence lifetime, and Mn luminescence quantum yield will be discussed. Chapter VI focuses on the generation of hot electrons from two consecutive exciton-Mn energy transfers and the potential applications on photocatalysis. Chapter VII discusses the strain effect on the local vibrational frequency that is coupled to the ${}^4T_1 \rightarrow {}^6A_1$ transition of Mn^{2+} ions and local thermal expansion in the doping location-controlled Mn-doped CdS/ZnS nanocrystals studied via temperature-dependent Mn luminescence spectra. Chapter VIII summarizes this dissertation with a brief discussion on future works.

CHAPTER II

BACKGROUND AND LITERATURE OVERVIEW

2.1 Electronic Structure of II-VI Semiconductor Nanocrystals and the Exciton Dynamics

2.1.1 Electronic Structure of II-VI Semiconductor Nanocrystals

II-VI semiconductor nanocrystals are interesting in their size tunable bandgap, resulting in tunable luminescence color. With the decreasing radius of the nanocrystals below the exciton Bohr radius, the bandgap becomes wider and the electronic band structure becomes discrete,^{38,39} giving rise to the distinct electronic transition features as observed in the absorption spectrum of CdSe nanocrystals in Figure 1.⁴⁰ The electronic transitions are assigned according to the effective mass theory considering the mixing of the three valence bands under spherical confinement.⁴¹ The resulting electron and hole states are labeled as S, P, D, which represents the angular momentum of the envelope wavefunction, $l = 0, 1, 2$. The subscript “e” indicates the electron state. The subscript for the hole denotes the total angular momentum of the envelope wavefunction and the Bloch-function. The allowed interband transitions only occur between the electron and hole state that has the same angular momentum of the envelope wavefunction. The valence and conduction band of the II-VI semiconductor are mainly composed of the p and s orbitals of the chalcogen ions and group 12 ions, respectively. Therefore, the valence band has *p* character, and the bandedge ($1S_{3/2}$) has 6-fold ($J = 3/2$ and $1/2$) degeneracy. The conduction band has *s* character, and the bandedge ($1S_e$) has 2-fold degeneracy ($J = 1/2$).

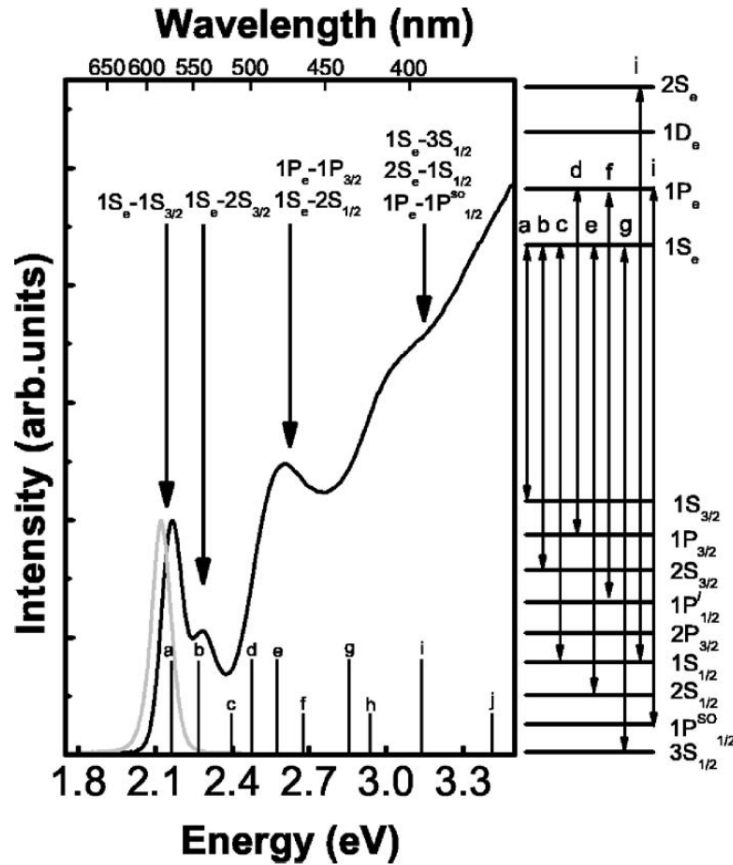


Figure 1. (Left) Absorption (black) and emission (gray) spectra of CdSe nanocrystals and (right) the corresponding state-to-state electronic transition. (Reprint with permission from Sewall, S. L.; Cooney, R. R.; Anderson, K. E. H.; Dias, E. A.; Kambhampati, P. *Phys. Rev. B* **2006**, *74*, 235328. Copyright 2006 American Physical Society)⁴⁰

Once the nanocrystals are optically excited, the electron and hole relaxes to the bandedge in <1 ps, followed by exciton emission upon recombination.^{42,43} (Gray curve in Figure 1) The intraband relaxation of the hole is through releasing energy to phonons. The energy between two nearest hole states is ~ 100 meV (energy difference between transition a and b in Figure 1), which is reasonably close to the LO phonon energy in CdSe nanocrystals of ~ 26 meV.⁴⁴ On the other hand, the electron cannot directly relax

through the phonon-assisted mechanism due to the large energy gap (>200 meV) between the nearest two electron states for the CdSe nanocrystals with diameter of 5 nm.⁴⁴ The intraband relaxation of electron has to go through an Auger mechanism by giving the energy to the hole and exciting the intraband transition of the hole. This mechanism requires a strong electron-hole coupling in the nanocrystals.^{45,46} The intraband relaxation time of electron and hole are few hundreds fs in quantum dots. However, by spatially separating the electron and hole using the band offset in a type II quantum well structure or using the hole trapping surfactant, the electron intraband relaxation time can increase to few ps and >1 ns, respectively.^{47,48}

2.1.2 Transient Absorption Measurement of Exciton Dynamics

Exciton dynamics of semiconductor nanocrystals can be obtained via pump-probe transient absorption measurement.⁴⁹ Transient absorption measurement uses a pump pulse that generates excitons in the nanocrystals, and a probe pulse measures the population of the exciton state at various pump-probe delay time. The quantity measured is the change of optical density of the probe beam with and without pump excitation as a function of time ($\Delta OD(t)$). By appropriately choosing the pump and probe wavelengths, dynamics of the electron and hole at a given state can be measured. For instance, bleach recovery probed at bandedge exclusively represents the relaxation dynamics of the bandedge electron.^{46,48,50-52} Probing at near IR gives the combined electron and hole dynamics via the intraband transition of the electron and hole.⁵³ Furthermore, by shifting the probe wavelength to the IR region at 1-3 μm , intraband transition of the electron or

hole to an electronic energy level higher can also exclusively measure the electron or hole dynamics.^{50,54,55}

A large number of studies have reported the exciton dynamics of undoped nanocrystals using the methods discussed above. Although the timescale varies with the sample quality, the timescale for the electron and hole trapping is in the order of few hundreds ps and few to ~50 ps, respectively.^{46,48,50-52} In fact, a recent study indicated that the surface trap introduces a false signal to the bleach recovery data due to the *absorption* of the trapped charge carrier that generates a *positive* ΔOD signal. Adding to the *negative* ΔOD signal of the recovery of the bandedge absorption, the bleach signal recovers faster than the actual recovery of the bandedge absorption. This issue can be avoided by overlaying a wide bandgap material on the surface of the nanocrystals to minimize the surface traps.¹⁷

2.2 Doped II-VI Semiconductor Nanocrystals

2.2.1 Synthesis and Characterization of Doped II-VI Semiconductor Nanocrystals

In the early studies, preparation of high quality Mn-doped nanocrystals was achieved by adapting the synthesis procedures for the undoped nanocrystals with the addition of Mn precursors. However, low doping yield, surface doping, and low luminescence quantum yield issues were encountered. Bhargava *et al.* prepared Mn-doped ZnS nanocrystals at low (room) temperature to avoid the exclusion of the dopants.^{56,57} To realize the location of the dopants, Bawendi and co-workers reported a careful study on the doping location through the hyperfine coupling

constant of the Mn electron paramagnetic resonance and etching experiment in the Mn-doped CdSe nanocrystals prepared via the hot injection method, well-developed for the undoped nanocrystals, with additional Mn precursors.⁵⁸ However, the dopants were found near the surface of the nanocrystals. Later, Norris *et al.* reported a successful synthesis of Mn-doped ZnSe nanocrystals also employing the hot injection method, as depicted in Figure 2a. The resulting nanocrystals have good size distribution and high quantum yield without the surface doping issue.⁵⁹ They reasoned that their success came from the stronger adsorption of the dopants to the (001) crystal surface in the zinc blende ZnSe over the wurtzite CdSe.² On the other hand, self-purification also has been used to explain the difficulty to dope the Mn ions. Dalpian and Chelikowsky performed DFT calculations that indicate the formation energy of the dopant site, which is also a defect, becomes higher with decreasing size of the nanocrystals.⁶⁰ The exclusion of the dopants can minimize the free energy.

Despite the controversy in the explanation of the doping mechanism, several new strategies, such as decreasing the synthesis temperature using cluster precursors and separating the crystal growth and doping processes, were developed.⁶¹ A few successful synthesis procedures are discussed here. Cluster thermolysis method performed at lower temperature has shown large tunable doping concentration in the preparation of Mn-doped CdSe nanocrystals.^{9,62,63} As shown in Figure 2a, the mixture of the cluster precursor of the host and the precursor of the dopant are heated together at the significantly lower temperatures

than the typical hot injection condition. The lower decomposition temperature of the cluster precursor of the host (e.g., ~ 215 °C) slows down the growth of the host material while increasing the probability of dopant binding on the surface of the nanocrystals during the growth process.⁶⁴ This method was also applied to the synthesis of other doped nanocrystals, such as Co-doped CdSe and Mn-doped ZnSe.^{9,18}

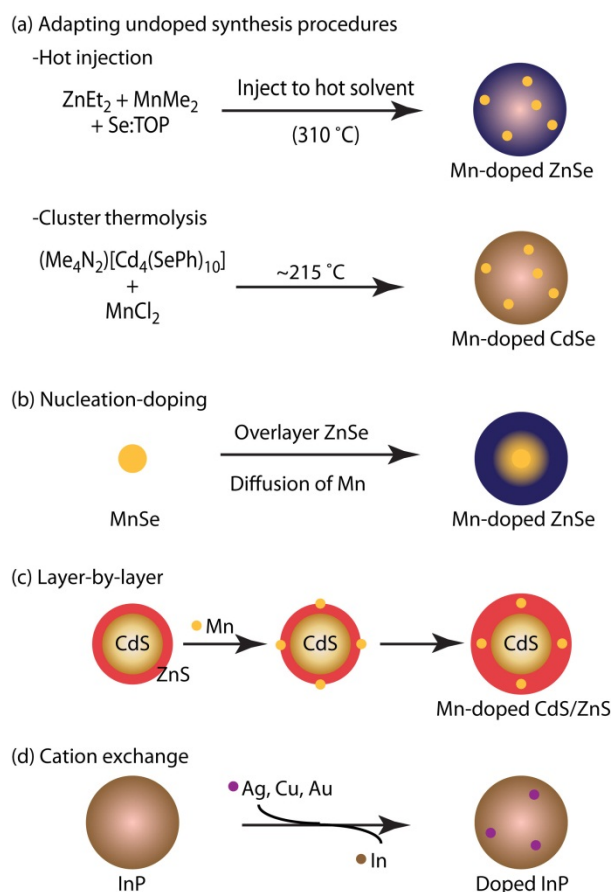


Figure 2. Chemical synthesis methods of colloidal doped semiconductor nanocrystals.

Peng's group developed "nucleation-doping" method to prepare Mn-doped ZnSe nanocrystals, as shown in Figure 2b.⁶¹ In this method, the preformed MnSe nanocrystal core was initially coated with ZnSe shell and doping was achieved via diffusion of Mn²⁺ ions from MnSe core into ZnSe shell.¹⁵ This method separates the doping process from the growth of the nanocrystals. Due to the high concentration of Mn²⁺ ions in MnSe core, the final doping concentration in ZnSe shell can be maintained high even with the loss of the dopant ions during the short period of the shell-growth process. This technique was also successfully applied to the synthesis of Mn-doped ZnS and CdS nanocrystals.^{65,66}

Another method of doping shown in Figure 2c uses layer-by-layer synthesis method.^{61,67} Initially, the core of the host nanocrystal is synthesized. Subsequently, the precursors of the host material is removed (or reduced) from the reaction mixture, and the precursor of the dopant is added to initiate doping. Such procedure suppresses the growth of the host material during the incorporation of dopant on the surface of the host nanocrystals. Once the dopant ions are bound on the surface, additional layers of the host material are over-grown at a relatively low temperature to fully imbed the dopant ions in the host without having self-purification. This method has been used successfully to synthesize both Mn- and Cu-doped II-VI semiconductor nanocrystals of various host structures, such as Cu-doped ZnSe, Mn-doped CdS/ZnS core/shell and Mn-doped ZnSe/ZnS core/shell.^{61,67,68} Adopting the layer-by-layer deposition procedure of the host materials, high level of control over the radial doping location also has been achieved by Cao's group.⁶⁹ The ability to control the doping location in the host nanocrystal is

particularly useful, since it allows the investigation of how the dynamics of the energy and charge transfer processes can be structurally tuned.^{37,70}

Cation exchange reaction has also been used to dope preformed host nanocrystals with various dopant ions. In this method, the cations in the host lattice are partially or completely exchanged with dopant cations in the solution mixture of the host nanocrystals and dopant ions.^{26,71-75} Figure 2d depicts an example of doping Ag, Cu, or Au in InP using cation exchange method reported by Banin and co-workers.⁷⁴ Thermodynamic driving force for the cation exchange is provided by the combination of the lattice energy and the solvation energy of the ions involved in the exchange reaction.^{71,76}

This method has been effective in the synthesis of Cu-, Ag-, and Mn-doped nanocrystals with a wide range of controllable doping concentration.^{26,74,75} In the case of Cu and Ag, the exchange of cations can be performed continuously from zero to complete exchange of the host cations with the dopant ions.^{26,71,73,74} A unique feature of the cation exchange reaction as the doping method is its ability to use the host nanocrystal as the structural template. The morphology of the host nanocrystal can be maintained during the exchange reaction.⁷¹ Furthermore, the reversible nature of the cation exchange reaction allowed transformation of the host nanocrystal into the structures with much higher chemical complexity.⁷⁷

The determination of whether the Mn^{2+} ions are doped in or on the nanocrystals requires electron paramagnetic resonance (EPR). A Mn^{2+} ion has nuclear spin quantum number (I) of 5/2 with natural abundance of 100%, so the Mn^{2+} EPR spectrum is a sextet.

The EPR spectral signature that reflects the location of Mn^{2+} ions is the hyperfine coupling constant, which increases at higher interaction between nucleus and unpaired electrons. As the Mn-chalcogen bond in the nanocrystal is stronger than the Mn-ligand bond on the surface of the nanocrystal, the hyperfine coupling constant is smaller when the Mn^{2+} is in the nanocrystals. The hyperfine coupling constant of the Mn^{2+} ion in and on the CdSe nanocrystals are ~ 62 gauss and ~ 80 gauss, respectively, while that in and on the ZnS nanocrystals are ~ 70 and ~ 90 gauss, respectively.^{2,4} The hyperfine coupling constant of Mn^{2+} ion found in nanocrystal is the same as that in bulk, since the hyperfine coupling constant only depends on the interaction between the nucleus and the electron localized to it. The constant is independent of the dimension of the material.

2.2.2 Dynamic Processes in Photoexcited Doped Nanocrystals

In doped semiconductor nanocrystals, there are many additional relaxation pathways of the photoexcited excitons compared to their undoped counterparts. The energy transfer between exciton and dopant or (and) the charge carrier transfer between the host and dopant can occur depending on the energetics of the donor and acceptor states in the nanocrystals. Such energy transfer and charge carrier transfer are responsible for new dopant-related emission in many doped semiconductor nanocrystals.^{21,26,64} These new dopant-related processes are also in competition with the exciton relaxation pathways operating in undoped nanocrystals. Here, we will describe several dynamic processes involved in the relaxation of excitons in a few examples of doped II-VI semiconductor nanocrystals.

Figure 3 compares the typical relaxation pathways of exciton in undoped and doped semiconductor nanocrystals. In undoped nanocrystals, the radiative recombination of excitons gives rise to the well-known band-edge exciton luminescence. Trapping of the electron and hole leads to the quenching of band-edge exciton luminescence and the emergence of the trap emission in some cases. Since the trapping is essentially a charge transfer process, the energetics and density of the trap states determine the efficiency of the trapping process that competes with the band-edge exciton luminescence.¹⁶

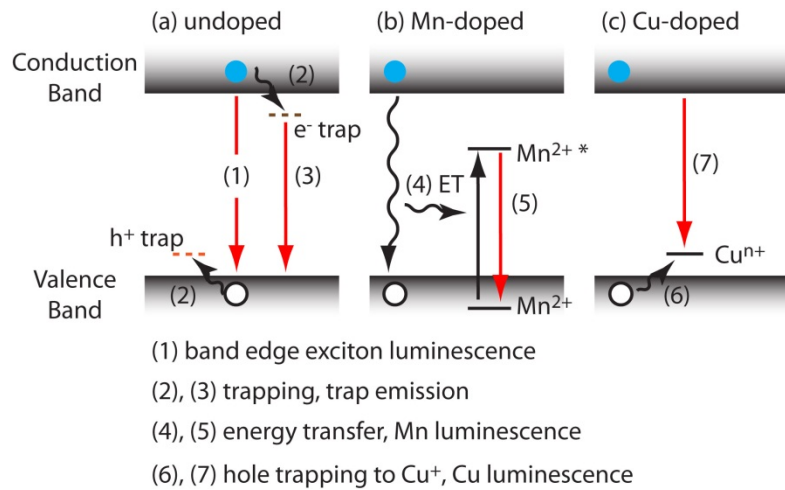


Figure 3. (a) Exciton relaxation pathways in undoped nanocrystals. (b) Energy transfer between exciton and dopant state in Mn-doped nanocrystals and resulting sensitized Mn luminescence. (c) Hole trapping followed by radiative charge carrier recombination in Cu-doped semiconductor nanocrystals.

In doped nanocrystals, the energy transfer between exciton and dopant is one of the major processes that deexcite excitons. The transition energy of the dopant should be smaller than the band-edge exciton energy to have the directional energy transfer. In such case, the sensitized dopant luminescence is observed. Examples are Mn-doped ZnS

or CdS nanocrystals, where the photoexcitation of exciton of the host results in Mn luminescence. Since the ligand field transition giving rise to Mn luminescence is dipole forbidden, its lifetime is in the range of 10^{-4} - 10^{-3} s. Due to the localized nature of the ligand field transition, the energy of Mn luminescence is sensitive only to the changes in the local ligand field unlike in exciton that shows the size-tunability via quantum confinement effect.⁶⁴

As the band-edge exciton and Mn ligand field transition energy becomes close, the back-energy transfer can also occur via thermal equilibration.⁶ Due to the large disparity in the lifetime of exciton and the excited state of Mn^{2+} ion (${}^4\text{T}_1$), Mn^{2+} ions can function as the long-lived energy reservoir for the back-energy transfer to exciton. Such process has been observed in Mn-doped nanocrystals such as CdSe or CdSSe/ZnS core/shell, where the host bandgap was only marginally larger than the Mn ligand field transition energy.^{6,18-20}

Recently, Cu-doped semiconductor nanocrystals, such as Cu-doped InP, ZnS/CdS and ZnSe/CdSe, were shown to exhibit widely tunable dopant luminescence arising from the charge carrier recombination at the dopant site.²¹⁻²³ Two different mechanisms were proposed for Cu luminescence in these materials depending on the initial oxidation state of Cu ion. One is the trapping of the hole by the Cu^+ ion followed by the radiative recombination of the electron in the conduction band with the localized hole at the dopant site.²² The second is the radiative relaxation of electron to Cu^{2+} ion followed by the localization of the hole.²³ Unlike in the sensitized luminescence in Mn-

doped nanocrystals, size-dependent conduction band-edge energy of the host nanocrystals results in tunable Cu luminescence.

In addition to adding new pathways of exciton population decay via energy or charge transfer, dopant ions can also create a new coupled state between exciton and dopant ions. In Mn-doped CdSe nanocrystals, where the bandgap is tuned smaller than Mn ligand field transition energy to suppress the energy transfer, exciton and Mn can form a coupled state called exciton magnetic polaron (EMP). At a sufficient low temperature and applied external magnetic field, the coupled state exhibits ferromagnetism, since the ferromagnetically ordered state of Mn^{2+} ions are the lowest energy state for the coupled state of exciton and Mn^{2+} ions. The exchange coupling between exciton and d electrons ($sp-d$ exchange coupling) of Mn^{2+} ions are mediating the formation of EMP.^{10,27-29} This interaction is particularly effective in nanocrystals because exciton and Mn^{2+} ions are confined within the same volume. Gamelin *et al.* reported that such spontaneous polarization of dopant spins can occur even at room temperature in doped nanocrystals due to more effective coupling between exciton and dopant ions.

2.2.3 Optical Properties of Mn-Doped II-VI Semiconductor Nanocrystals

In Section 2.2.2, the dynamics process of photoexcited Mn-doped nanocrystals was briefly compared with other dopants. In this section, more details of the optical properties, including the extinction coefficient, luminescence lifetime, spectrum, and

quantum yield of Mn-doped nanocrystals will be compared with the undoped nanocrystals.

Mn-doped II-VI semiconductor nanocrystals have a high and robust luminescence quantum yield from the ligand field transition of the Mn^{2+} ions, almost independent of the solvent environment and surface structure of the nanocrystals. As illustrated in Figure 4, Mn luminescence comes from the transition from ${}^4\text{T}_1$ to ${}^6\text{A}_1$ state of the d electrons localized at Mn^{2+} ions after exciton-Mn energy transfer. The Mn luminescence peak wavelength and bandwidth (~ 600 and ~ 70 nm, respectively) are largely red-shifted and broadened from the bandedge exciton (~ 440 and 25 nm).^{4,78,79} Directly optically exciting the Mn^{2+} electronic transition is difficult since excitation to any excited state requires a change of spin quantum number. Therefore, the extinction coefficient of the $d-d$ transition is only $1\text{-}10\text{ M}^{-1}\text{ cm}^{-1}$, much smaller than that of the host at $10^5\text{-}10^6\text{ M}^{-1}\text{ cm}^{-1}$.^{15,67}

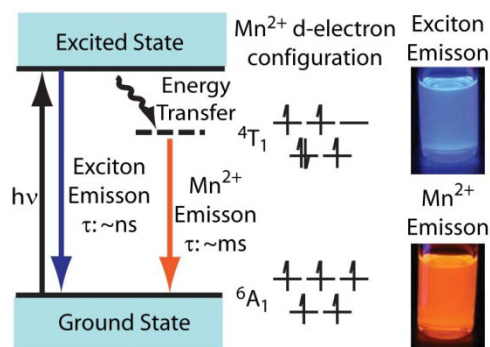


Figure 4. Energy level diagram of Mn-doped nanocrystals and photograph of photoluminescence from undoped (top right) and Mn-doped CdS/ZnS (bottom right) nanocrystals.

To achieve high dopant luminescence quantum yield, fast exciton-Mn energy transfer is required so that trapping can be avoided. In undoped nanocrystals, non-radiative processes such as charge carrier trapping to the surface state have been one of the most concerning issues. Due to the large surface-volume ratio of the nanocrystals, the surface imperfection or some of the surfactants (thiol ended surfactants, such as mercapto aliphatic acid and aliphatic thiol) of the nanocrystals can significantly quench the exciton luminescence.^{43,46,80} Trapping not only decreases the quantum yield of the nanocrystals, it also turns the luminescence on and off alternately, known as “blinking.” Blinking happens when a hole or electron is trapped, leaving an unrelaxed electron or hole in the conduction or valence band, respectively. Any additional exciton generated after trapping will relax through a non-radiative Auger deexcitation that the exciton energy transfers to the unrelaxed charge carrier until the trapped charge carrier recombines with its counterpart. Blinking has been a major obstacle in the application of nanocrystals in single molecule imaging. Many researchers have tried to solve the issue by decreasing the trap density through the nanocrystal synthesis procedures or electrically injecting electrons to the electron traps, but the problem are not completely resolved. An alternative solution is to use Mn-doped nanocrystals that the fast exciton-Mn energy transfer can reroute the exciton from trapping to the *d* electron localized to the Mn²⁺ ions. Reports and our experimental result have shown that the quantum yield of the Mn-doped nanocrystals is almost independent of the surface ligands.⁸¹

The Mn luminescence peak wavelength depends on the combination effect of the chalcogenide ligand and doping concentration. The Mn luminescence energy is

essentially the pairing energy minus the ligand field splitting as demonstrated in Figure 4, and it typically peaks at ~ 590 nm with small dependence (± 10 nm) on the host material and doping concentration.^{64,82} Also, Mn luminescence wavelength is not size-tunable like the exciton. However, the luminescence red-shifts at stronger local lattice strain that can be manipulated by the core radius, shell thickness, and the composition of the core/shell nanocrystals.^{66,83} This is explained by the larger compression on the Mn due to the lattice strain that enhances the ligand field splitting.

Furthermore, the radiative lifetime of Mn, which also depends on the ligands and doping concentration, shortens at stronger spin-orbit coupling and superexchange coupling. Mn luminescence lifetime is much longer than that of the exciton (\sim ms vs ~ 10 ns) due to the spin-forbidden nature of the relaxation. The change of spin quantum number is compensated via the spin-orbit coupling with the ligands, chalcogens. Therefore, the shortening of lifetime follows the increasing spin-orbit coupling strength with atomic weight in the order of O^{2-} , S^{2-} , Se^{2-} , and Te^{2-} . For example, the Mn luminescence lifetime with Se^{2-} and S^{2-} ligands are ~ 100 μ s and 1 ms, respectively.^{84,85} Similarly, the lifetime becomes shorter with the assist of superexchange coupling between the neighboring Mn^{2+} ions that increases with increasing doping concentration.⁸⁴

2.3 Theory and Measurement of Energy Transfer Dynamics

2.3.1 Theory of Energy Transfer^{86,87}

Energy transfer is an energy conserved and non-radiative process that the energy is transferred from an excited donor to a ground state acceptor mediated by Coulomb or exchange interaction between the donor and acceptor electron clouds.⁸⁶ Figure 5 depicts the relevant processes to energy transfer, from excitation of the donor to the relaxation of the acceptor. (1) The donor is excited optically or electrically. (2) A fast vibrational relaxation (<1 ps) brings the excited state of donor down to its lowest vibrational state. (3) The energy transfer (~ps), mediated by the Coulomb or exchange interaction, occurs from donor to the acceptor with no energy loss. (4) A fast vibrational relaxation (<1 ps) brings the excited state of the acceptor down to its lowest vibrational level at the lowest excited state. (5) The acceptor relaxes either radiatively or non-radiatively (few ns to few s). In the processes listed above, a few assumptions are made to simplify the system. These assumptions are true for most of the cases as well as for the experiments discussed in this dissertation. (a) The donor typically has absorption cross section much larger than the acceptor at the excitation wavelength so that the excitation light is absorbed by the donor. (b) Energy transfer occurs when donor and acceptor are close in distance so that their electron clouds interact with each other. (c) As the energy transfer occurs, the relaxation of donor and the excitation of acceptor happen simultaneously with energy completely transferred because these electronic transitions are too fast (sub-fs) to lose energy to the surrounding. Therefore, the transition probability depends on how well the energy of the two electronic transitions match, which can be calculated from the spectral

overlap between the donor luminescence lineshape and the acceptor absorption lineshape. (Figure 6a) (d) Back energy transfer is ignored. Energy transfer to acceptor is typically followed by a fast vibrational relaxation that releases part of the energy to the lattice. The energy of the acceptor becomes insufficient for the back energy transfer to the donor and thus this possibility can be ignored. However, if the acceptor energy level is only slightly lower than the donor energy level, back energy transfer can occur with the assist of thermal energy. Examples will be discussed in section 2.3.3.

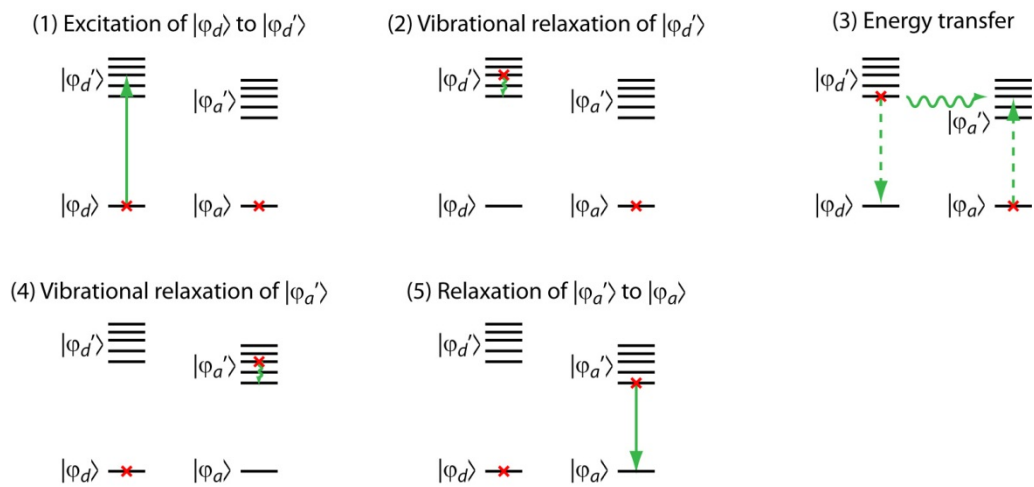


Figure 5. Relevant processes to energy transfer occur from (1) to (5). $|\varphi_d\rangle$ and $|\varphi_d'\rangle$ are the donor ground and excited states, respectively. $|\varphi_a\rangle$ and $|\varphi_a'\rangle$ are the acceptor ground and excited states, respectively. The crosses indicate the states of the donor and the acceptor. The arrows indicate the change of states described at the top of each sub-figure.

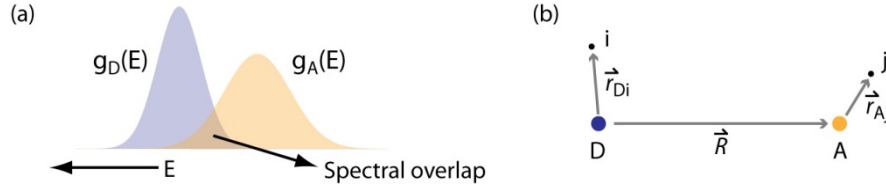


Figure 6. (a) Spectral overlap between donor absorption and acceptor emission spectrum, $g_D(E)$ and $g_A(E)$, respectively. (b) Illustration of spatial correlation between donor nucleus (D), acceptor nucleus (A), donor electron (i), and acceptor electron (j).⁸⁷

Energy transfer requires Coulomb or exchange interaction and transition energy-matching between the donor and acceptor. According to Fermi's golden rule, the energy transfer probability is

$$P_{DA} = \frac{2\pi}{\hbar} |\langle \Psi_i | \hat{H} | \Psi_f \rangle|^2 \int g_D(E) g_A(E) dE \quad (1)$$

where Ψ_i and Ψ_f are the wavefunction of the initial and final states. $g_D(E)$ is donor emission lineshape and $g_A(E)$ is acceptor absorption lineshape. This equation includes the two important parameters affecting the energy transfer probability: transition probability $|\langle \Psi_i | \hat{H} | \Psi_f \rangle|^2$, also called Fermi's golden rule, and the spectral overlap, $\int g_D(E) g_A(E) dE$.

Spectral overlap between the donor emission and acceptor absorption spectra is critical for energy transfer because energy transfer is an energy conserved process. From Franck-Condon principle, electronic transition absorbs the whole energy of a photon with small probability that the energy is lost to the lattice. Thus, the energy released by the donor and absorbed by the acceptor need to be the same. The emission spectrum of the donor is the probability distribution of the energy that the donor can release in the electronic relaxation, while the absorption spectrum of the acceptor is the probability

distribution of the energy that the acceptor can absorb in the electronic excitation. Therefore, the energy transfer probability is proportional to the spectral overlap, (Figure 6a) denoted by $\int g_D(E)g_A(E) dE$.

Transition probability $|\langle \Psi_i | \hat{H} | \Psi_f \rangle|^2$ part in eq 1 can be written as

$$\begin{aligned} \langle \Psi_i | \hat{H} | \Psi_f \rangle = & \langle \varphi_a'(r_i)\varphi_a(r_j) | \hat{H} | \varphi_a(r_i)\varphi_a'(r_j) \rangle \times \langle \chi_a'(\sigma_i)\chi_a(\sigma_j) | \chi_a(\sigma_i)\chi_a'(\sigma_j) \rangle \\ & - \langle \varphi_a'(r_i)\varphi_a(r_j) | \hat{H} | \varphi_a(r_j)\varphi_a'(r_i) \rangle \times \langle \chi_a'(\sigma_i)\chi_a(\sigma_j) | \chi_a(\sigma_2)\chi_a'(\sigma_j) \rangle \end{aligned} \quad (2)$$

φ_a and φ_a' represents the donor ground and excited state orbital wavefunctions, respectively. φ_a and φ_a' represents the acceptor ground and excited state orbital wavefunctions, respectively. r_i and r_j are the coordinates of all the charge clouds of donor and acceptor, respectively. $\chi(\sigma)$ is the spin wavefunction and the superscript and subscript has the same meaning as the orbital wavefunction. The first term and the second term of eq 2 come from the Coulomb and the exchange interaction, respectively, between the donor and acceptor charge clouds. If both the donor and acceptor have transition dipole and the spin quantum number is conserved, the Coulomb interaction term is much greater. The exchange term can be ignored. This is the Förster resonant energy transfer (FRET). On the other hand, if either the donor or acceptor does not have transition dipole, or if the spin quantum number is not conserved, Coulomb interaction term vanishes. The exchange term becomes important. This is the Dexter energy transfer.

The \hat{H} describes the Coulomb interaction between all the charges of the donor and acceptor:

$$\hat{H} = \frac{1}{4\pi\epsilon_0} \frac{1}{\kappa} \sum_{i,j} \frac{e^2}{\vec{R} + \vec{r}_{Aj} - \vec{r}_{Di}} \quad (3)$$

where ϵ_0 and κ are vacuum permittivity and dielectric constant of the medium. \vec{R} , \vec{r}_{Aj} , and \vec{r}_{Di} are the vector from donor nucleus to acceptor nucleus, from acceptor nucleus to each of the acceptor electron, from donor nucleus to each of the donor electron, as plotted in Figure 6b (p. 22). After the Taylor expansion of Eq 3, \hat{H} is split to the sum of dipole-dipole interaction, dipole-quadrupole, and higher order interaction terms. If only the dipole-dipole interaction term is considered, the energy transfer probability can be simplified to⁸⁸

$$P_{DA}^{dd} = \frac{4\pi}{3\hbar} \left(\frac{1}{4\pi\epsilon_0\kappa} \right)^2 \frac{1}{R^6} |\langle\mu_D\rangle|^2 |\langle\mu_A\rangle|^2 \int g_D(E) g_A(E) dE \quad (4)$$

where $|\langle\mu_D\rangle|^2$ and $|\langle\mu_A\rangle|^2$ are the squared transition dipole moment of the donor and acceptor, respectively. Eq 4 indicates that the dipole-dipole interaction-mediated energy transfer probability is proportional to:

- i. R^{-6} and
- ii. the squared transition dipole moment of the donor and acceptor. The squared transition dipole moment can be conveniently obtained using its proportionality with the oscillator strength measured from the optical absorption.

The above discussion is limited to both the donor and acceptor that have transition dipole without changing the spin quantum number. From eq 4, we can see dipole-dipole interaction-mediated energy transfer probability is zero if either donor or acceptor have no transition dipole, i.e., $|\langle\mu_D\rangle|^2$ or $|\langle\mu_A\rangle|^2$ is zero. From eq 2, if the donor

or acceptor changes the spin states after energy transfer, the probability of energy transfer also becomes zero. In these cases, energy transfer may occur through exchange interaction. Since exchange interaction only occurs between the electrons with spatial overlap, eq 3 is rewritten as

$$\hat{H} = \sum_{ij} \frac{e^2}{\kappa \vec{r}_{ij}} \quad (5)$$

The energy transfer probability becomes

$$P_{DA}^{ex} = \frac{2\pi e^4}{\hbar \kappa^2} \left| \left\langle \varphi_d'(r_i) \varphi_a(r_j) \left| \sum_{ij} \frac{1}{\vec{r}_{ij}} \right| \varphi_a(r_j) \varphi_d'(r_i) \right\rangle \right|^2 \int g_D(E) g_A(E) dE \quad (6)$$

One can see that the probability of energy transfer is proportional to the wavefunction overlap between the donor and acceptor. Since electron wavefunction approximately decays exponentially with distance, eq 6 is approximately

$$P_{DA}^{ex} = \frac{2\pi e^4}{\hbar \kappa^2 R_0^2} \exp(-2R/L) \int g_D(E) g_A(E) dE \quad (7)$$

where R_0 is the distance where energy transfer efficiency is 50%. L is the effective average Bohr radius of the donor-acceptor pair at the initial state.

The typical maximum distance for dipole-dipole interaction-mediated energy transfer is ~ 100 Å. However, Dexter energy transfer requires shorter distance so that the donor and acceptor wavefunction have spatial overlap, typically < 10 Å. In addition, the energy transfer probability is proportional to R^{-6} for FRET and $\exp(-R)$ for Dexter energy transfer mechanism. Sometimes the energy transfer mechanism of a given system is justified to be either FRET or Dexter by simply fitting the donor-acceptor distance (R)-energy transfer rate data to the above correlations. This may not always be true because if the distance between the donor and acceptor is small, especially when they overlap

with each other, the distance is hard to define. Also, the wavefunctions probability of the donor and acceptor are not necessarily decay exponentially with distance. Therefore, the proportionality of energy transfer with the function of distance may not be applicable.

2.3.2 Measurement of the Energy Transfer Dynamics

The exciton-Mn energy transfer rate in bulk semiconductor and self-assembled quantum dots in the earlier works were mostly studied via the time-resolved measurement of exciton luminescence.⁸⁹⁻⁹² For instance, the decay time of exciton luminescence in self-assembled ZnSe quantum dots measured with a streak camera following <5 ps excitation decreased from 200 to ~15 ps upon Mn doping, indicating that the energy transfer occurs on tens of ps time scale in the system studied.⁸⁹ However, time-resolved measurement of exciton or Mn luminescence is less useful for the measurement of the energy transfer rate in colloidal Mn-doped quantum dots due to the significant presence of charge carrier traps and trap emission. The higher density of trap states in colloidal quantum dots not only opens additional exciton relaxation pathways but also gives rise to the trap emission that interferes with the measurement of the energy transfer rate via time-dependent donor and acceptor luminescence intensities.⁹³

Pump-probe transient absorption has been used recently to measure the energy transfer rate in doped quantum dots.⁹⁴ For instance, Olano *et al.* used transient absorption technique to measure the energy transfer rate by comparing the decay of intraband absorption in conduction band that represents the decay of the electron population via exciton relaxation combined with the energy transfer. The faster decay of

the intraband absorption signal upon doping was ascribed to the energy transfer. Their result indicated the energy transfer time is tens of ps in their colloidal Mn-doped quantum dots. However, the potential spectral overlap of intraband electron absorption and other transitions, such as from the trap states or intraband hole transition, can complicate the extraction of the energy transfer rate.

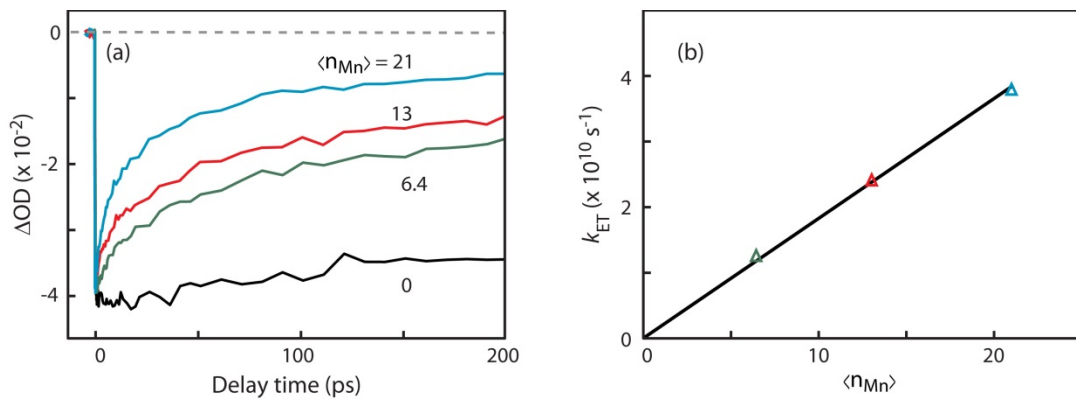


Figure 7. (a) Dynamics of band-edge bleach recovery in Mn-doped CdS/ZnS core/shell nanocrystals with varying doping concentrations ($\langle n_{Mn} \rangle$) and a fixed radial doping location. (b) The linear correlation of the energy transfer rate extracted from (a) on Mn doping concentration.

In this dissertation, the energy transfer rate is more reliably measured by probing the transient absorption at the band-edge as well as the intraband electron absorption in Mn-doped nanocrystals with the controlled radial doping location and doping concentration.^{37,95} Since the dynamics of bleach recovery at the band-edge represents only the electron dynamics,^{46,48,50-52} the energy transfer rate could be more straightforwardly extracted from the comparative analysis of the dynamics between doped and undoped nanocrystals. The fact that the energy transfer rate is linearly proportional to the doping concentration allowed more reliably extraction of the energy

transfer rate.^{37,95} (Figure 7) The rate of the competing charge carrier trapping process was also obtained from the analysis of the amplitudes of the fast and slow-recovery components as will be discussed in detail in Chapter V. Furthermore, the ability to control the radial doping location and doping concentration allowed us to correlate the energy transfer rate with the structurally-controllable wavefunction overlap between exciton and dopant that ultimately dictates the dynamics of the energy transfer. More detailed discussion on the dependence of the rate of energy transfer and other competing processes on the structure of the doped nanocrystals will be made in Chapter IV and V.

2.3.3 Energy Transfer Mechanism in Mn-Doped II-VI Semiconductor Nanocrystals

In Mn-doped semiconductor nanocrystals, we believe Dexter energy transfer is a more reasonable process although it is still under debate. As discussed in section 2.2.3, the excitation of Mn^{2+} d electrons from ground state is always a spin-forbidden transition. Although relaxation of exciton is a spin-allowed transition, Coulomb interaction-mediated energy transfer vanishes. On the other hand, exchange mechanism may occur efficiently. Especially in Mn-doped nanocrystals, the exciton Bohr radius is smaller than the radius of the nanocrystals. The exciton is delocalized over the entire nanocrystals, including where the dopants are, without migration. Exciton-Mn exchange interaction is thus strong and be a plausible driving force of energy transfer.

Cao and coworkers attempted to determine the exciton-Mn energy transfer mechanism by correlating the energy transfer yield to the radial doping locations in Mn-doped CdS/ZnS nanocrystals where Mn is doped in the ZnS shell. From the best fit of

the energy transfer yield and radial doping locations to FRET or Dexter mechanism ($P_{da} \propto 1/R^6$ or $P_{da} \propto \exp(-R)$, respectively), they conclude the energy transfer mechanism is FRET. However, determining the donor-acceptor distance (R) is difficult because the donor is on top of the acceptor. The authors used the center of mass of the exciton (which is at the center of the nanocrystal) as the location of the donor. This assumption is not entirely applicable in their study, since the exciton wavefunction in the core/shell nanocrystals is distorted from the H-like wavefunction distribution. The correlation between energy transfer probability and donor-acceptor distance in FRET and Dexter energy transfer mechanism needs to be re-established using the exciton wavefunction in the core/shell structure.

CHAPTER III
SYNTHESIS OF Mn-DOPED NANOCRYSTALS AND EXPERIMENTAL
METHODS*

3.1 Synthesis of Nanocrystals

The undoped and Mn-doped CdS/ZnS or CdSe/ZnS core/shell nanocrystals were prepared using the layer-by-layer coating and doping methods on the core nanocrystals following the published procedures with some modifications.^{69,96,97} Details on the optimization of the shape and the luminescence quantum yield of the final nanocrystal samples are also discussed.

3.1.1 Synthesis of Cadmium Sulfide (CdS) Nanocrystals

CdS nanocrystals were synthesized by injecting 1-octadecene (ODE) solution of sulfur (0.25 M, 2.0 mL) into a mixture of cadmium oxide (0.126 g), oleic acid (2.02 g),

* Reprinted in part with permission from Chen, Hsiang-Yun; Chen, Tai-Yen; Son, Dong Hee. Measurement of Energy Transfer Time in Colloidal Mn-Doped Semiconductor Nanocrystals. *J. Phys. Chem. C* **2010**, *114* (10), 4418-4423. Copyright 2010 by the American Chemical Society.

Reprinted in part with permission Chen, Hsiang-Yun; Maiti, Sourav; Son, Dong Hee, Doping Location-Dependent Energy Transfer Dynamics in Mn-Doped CdS/ZnS Nanocrystals. *ACS Nano* **2012**, *6* (1), 583-591. Copyright 2012 by the American Chemical Society.

and ODE (12.0 mL) heated at 250 °C under nitrogen atmosphere. After the injection, the growth temperature dropped to 240 °C. The diameter of the nanocrystals became larger with time, as seen from the red-shift of the absorption band edge. Once the absorption band edge shifted to 422-423 nm, the reaction was quickly cooled to room temperature to terminate the growth of the nanocrystals. To clean the nanocrystals, ~25 mL of acetone was added. The solution was centrifuged, and the supernatant was discarded. The precipitate was further rinsed twice by dissolving and precipitating with toluene and methanol. The resulting precipitate was in powder form with yellow color. The absorption and luminescence spectra of a typical CdS nanocrystal sample are shown in Figure 8a. The distinct electronic transition peaks in the absorption spectrum and the sharp exciton luminescence peak (peaked at 440 nm) indicate the narrow size distribution of the nanocrystals. The TEM of the nanocrystals is in Figure 11a. The broad luminescence at ~600 nm is from the trap emission. The concentration of the nanocrystals is estimated using the band edge absorbance with an extinction coefficient of 330,000 M⁻¹ cm⁻¹.

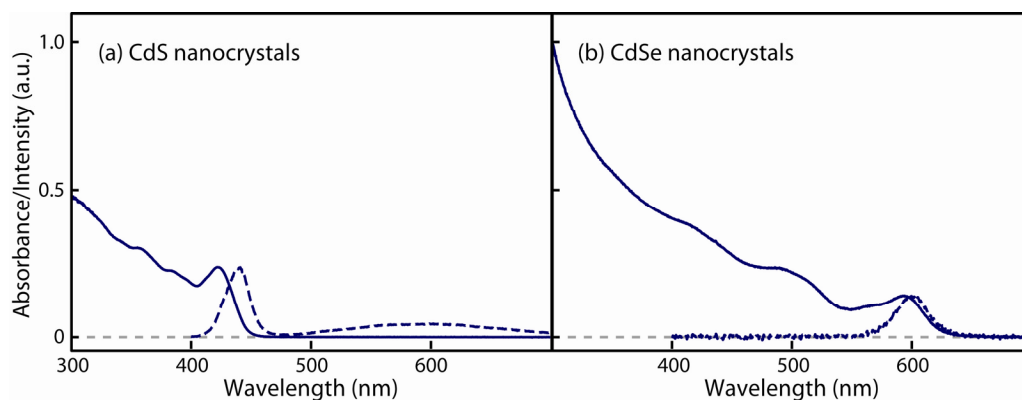


Figure 8. Absorption (solid) and luminescence (dashed) spectra of (a) CdS and (b) CdSe nanocrystals. The gray dashed line indicates the zero intensity. The luminescence spectra were taken using a CCD spectrometer (USB 2000, Ocean Optics) without intensity calibration. A 370 nm light emitting diode was used as the excitation light source.

3.1.2 Synthesis of Cadmium Selenide (CdSe) Nanocrystals

Cadmium oxide (0.250 g), hexadecylamine (2.85 g), trioctylphosphine oxide (1.15 g), and tetradecylphosphonic acid (1.09 g) were mixed in a 25 mL 3-neck flask and evacuated at 100 °C for 1 h. Under nitrogen atmosphere, the mixture was heated to 295 °C. Once the cadmium oxide completely dissolved, tributylphosphine (1.00 g) was added. After the temperature stabilized at 295 °C, tributylphosphine solution of selenium (10% w/w, 0.80 g) was swiftly injected, and the growth temperature was lowered to 275 °C. Once the desired nanocrystal diameter is reached by monitoring the wavelength of the absorption band edge, the solution was cooled to 60 °C, and a mixture of octanoic acid and toluene (~7 mL each) was added. The precipitated CdSe nanocrystals were rinsed by repeated dispersion and precipitation using toluene and methanol, respectively. The absorption and luminescence spectra of a typical CdSe nanocrystal sample are shown in Figure 8b.

3.1.3 Doping the Mn²⁺ Ions

The Mn²⁺ ions in the nanocrystals were doped via the layer-by-layer doping method.⁶⁹ In other words, the Mn²⁺ ions were doped on the surface of the nanocrystals, and extra shell material (ZnS) were layered on to embed the Mn²⁺ ions. In this section, only the steps of doping the Mn²⁺ ions on the surface of the nanocrystals are discussed. Further layering of ZnS will be discussed in the following section.

The stock solutions of Mn²⁺ precursors were prepared as follows.

Precursor A: 0.02 M manganese acetate in oleylamine (OAm) was prepared by the addition of air-free OAm (24 mL) to manganese acetate tetrahydrate (118 mg) under vacuum. After the mixture further evacuated for 5 min, the solution was heated to 120 °C for 10 min. The solution was cooled to room temperature in vacuum. To minimize the possibility of air leaking, the solution was kept under vacuum. Nitrogen was purged into the flask right before use. If the solution was not used immediately, it was transferred to a vial filled with nitrogen and stored in the nitrogen glove box.

Precursor B: 0.015 M manganese diethyldithiocarbamate in OAm was prepared by mixing sodium thiocarbamate (108 mg) and OAm (4 mL) in a 50 mL three-neck flask in the glove box. The flask was sealed and taken out of the glove box. The mixture was evacuated using the Schlenk line for 5 min at room temperature. Under vacuum, the solution was heated to 60 °C for 10 min, and 12.0 mL of Precursor A was injected. After 10 min, the solution was cooled to room temperature under vacuum. Nitrogen was purged into the flask right before use. If the solution was not used immediately, it was transferred to a vial filled with nitrogen and stored in the nitrogen glove box.

Both Precursor A and B were used within a week after preparation for the consistency of doping yield. The solutions are oxygen-sensitive. The sign of oxidation is a change of color. Precursor A should be light yellow (same color as OAm), while Precursor B is bright yellow. If the manganese is oxidized, the solution would turn to golden, light brown, or dark brown. The precursor solution should be discarded if any sign of oxidation is observed.

The choice of precursor for the doping of Mn^{2+} ions depends on the outer material of the nanocrystals. Precursor A is used for doping on the surface of ZnS, while Precursor B is used for doping on the surface of CdS. When using Precursor A, the reaction temperature is raised to 260 °C. At such a high temperature, the ZnS coated nanocrystals can avoid Ostwald ripening, but the CdS nanocrystals cannot. To avoid the Ostwald ripening of the CdS nanocrystals, the more reactive Precursor B is used at a lower reaction temperature (220 °C).

To dope Mn^{2+} ions on the surface of CdS nanocrystals ($d = 0$ nm), Precursor B was added to the CdS nanocrystals in ODE and OAm at 220 °C. The solution was cooled to room temperature after 20 min. For the Mn^{2+} ions that were doped on the surface of ZnS ($d = 0.6$ and 1.2 nm), ODE solution of sulfur and Precursor A were added to the CdS/ZnS nanocrystals in ODE and OAm at 260 °C. The solution was cooled to room temperature after 20 min.⁶⁹ The Mn-doped nanocrystals were extracted by the addition and precipitation with acetone. The nanocrystals were further dispersed and precipitated with toluene and methanol once to remove the excess Mn precursor. The nanocrystals were then dissolved in toluene and centrifuged, and the supernatant was used for further

ZnS layering. Extra precipitation of the nanocrystals is not suggested, or the doping yield would decrease, and the nanocrystals would be very difficult to precipitate. The doping yield is 20-30%.

While precipitating the nanocrystals, the supernatant should be either a colorless or brownish clear solution, depending on the amount of Mn precursor added. On the other hand, the supernatant should not be cloudy. The cloudy supernatant indicates that a significant amount of the nanocrystals still remain unprecipitated. Extra shaking of the container and longer waiting before centrifuging the solution can increase the amount of precipitation. Addition of oleic acid also accelerates the precipitation, but it washes away the surface Mn^{2+} ions as well. The recovery of nearly all the nanocrystals is critical for the consistency of the final nanocrystal samples, since the quantity of reacting nanocrystals can only be conveniently estimated once from the initial CdS cores for the entire doping and overlayering processes. After doping or overlayering on the CdS nanocrystals, the extinction coefficient at band edge, which is typically used to estimate the concentration of nanocrystals, changes from sample to sample. Estimation of the nanocrystal concentration then requires elemental analysis, which is extremely time consuming.

3.1.4 Overcoating the ZnS Shell

To coat extra ZnS shell on the surface of Mn-doped or undoped nanocrystals, the nanocrystals (from one batch synthesis in 2.1.1) in toluene was transferred to a three-neck flask, and the toluene was partially evaporated by blowing nitrogen gas. After the

addition of OAm (2 mL) and ODE (6 mL), the solution was evacuated and refilled with nitrogen gas three times and heated to 220 °C under nitrogen atmosphere. 0.25 M ODE solution of sulfur and 0.25 M toluene solution of zinc stearate were added alternately over 2-3 min and ~1.5 min, respectively, with a 10 min interval until the desired thickness of ZnS has reached. 5 min after the addition of the final layer of zinc stearate solution, extra zinc stearate solution (1-2 times of the last injection) was added to ensure the surface of the nanocrystals was zinc-rich. After 5 min, the reaction solution was cooled to room temperature. The cleaning procedures were also the same as that for CdS nanocrystals.

Please note that the nanocrystals should be properly dispersed, and the duration of the nanocrystal solution without the addition of the precursor should be short to minimize the possibility of Ostwald ripening. In detail, the solvent used to transfer the nanocrystals to the 3-neck flask should not be completely evaporated, or the nanocrystals cannot disperse into the OAm and ODE easily. Second, the initial heating of the nanocrystals solution to 220 °C should be fast (~10 min) using appropriately sized three-neck flask and heating mantle under rigorous stirring. For example, $11 > \text{flask volume} / \text{solution volume} > 6$. As soon as the solution was heated to 220 °C, the addition of sulfur solution should begin immediately at proper addition rate (2-3 min/addition). These guidelines are particularly important when the initial nanocrystals are undoped or Mn-doped CdS nanocrystals. Failing to follow these guidelines would result in Ostwald ripening of the nanocrystals and the size distribution will be broadened. Figure 9 compares samples using the same batch of CdS core, and the same amount of manganese,

sulfur, and zinc precursors under different heating and coating conditions. Sample 1 was prepared using a long heating time (~20 min) and slow sulfur addition rate (7 min/addition), while sample 2 was prepared following the heating time and sulfur addition rate in the guidelines. The band edge absorption of sample 1 becomes broader due to the Ostwald ripening, indicating the size distribution of the nanocrystals increases. The band edge absorption also extends to a longer wavelength (~480 nm), which can be visually observed from the change of color from yellow to orange. However, the change of color due to Ostwald ripening should not be confused with the color of the unreacted sulfur. Unreacted sulfur in the solution also has an orange to dark red color at temperatures higher than 220 °C. If the orange color is from the unreacted sulfur, the color of the reaction solution would turn back to yellow once the sulfur is grown on the surface of the nanocrystals. The synthesis would still be successful.

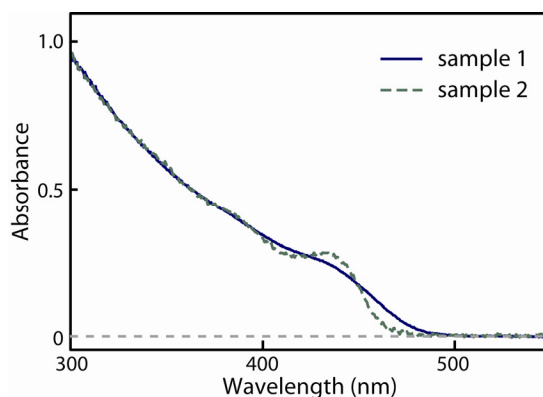


Figure 9. Absorption spectra of Mn-doped CdS/ZnS nanocrystals with (sample 1, solid) and without (sample 2, dashed) Ostwald ripening with the same CdS core, the amount of Mn, and the amount of ZnS precursor. The gray dashed line indicates 0 absorbance.

The quantity of sulfur and zinc precursor added at each addition has a critical effect on the shape and the luminescence quantum yield of the nanocrystals. In principle, the amount of sulfur precursor for each addition is calculated based on the volume of a monolayer (ML) of ZnS per nanocrystals and the total number of nanocrystals in the reaction solution. The thickness of a ML of ZnS is 0.31 nm, which is the thickness of one layer of the bulk ZnS in face-centered cubic packing. However, the reaction yield is not 100%. Also, the relative amount of sulfur and zinc precursors used for each addition and the layering steps vary the quality of the resulting nanocrystals. Here a few parameters on the layering of ZnS on the undoped CdS are discussed.

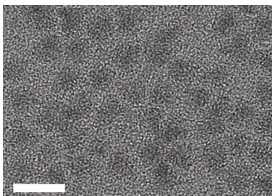
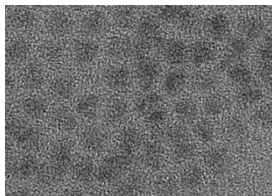
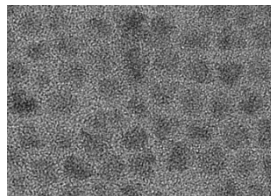
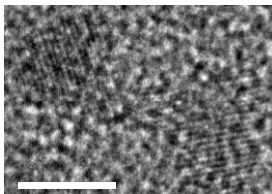
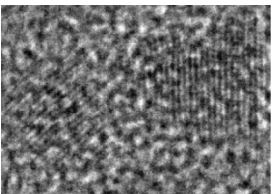
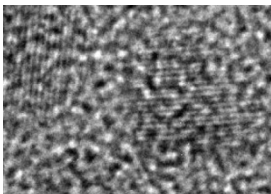
One vs. two stages. Table 1 conditions a and b used the same amount of precursor for each addition, but ZnS was overlaid in one and two stages, respectively. In condition a, all the precursors are added before cooling and precipitation of the nanocrystals, while in condition b, the reaction was cooled and the nanocrystals were cleaned after the third addition of sulfur and zinc before further layering of ZnS. The similarity of the absorption spectra (Figure 10) indicates the amount of ZnS coated on the CdS is virtually the same. However, in condition b, the TEM shows the nanocrystals are slightly more spherical, but the luminescence quantum yield is lowered by 30%. Extra charge carrier traps might be introduced due to the missing cations while washing the nanocrystals in the middle of the ZnS layering process.

Amount of zinc precursor at each addition. Table 1 conditions c and d use the same amount of sulfur, but different amounts of zinc. In condition c, the same amount of zinc and sulfur is used for the same number of precursor injections, while in condition d,

more zinc is injected. That is, for the n^{th} injection of zinc, the average amount of n^{th} and $(n+1)^{\text{th}}$ injection of sulfur is used. The absorption spectra of the nanocrystals from these two conditions are again similar, but the quantum yield is higher by ~90% in condition d. The addition of extra zinc precursors might reduce the amount of hole trap which is the main source of the non-radiative process in semiconductor nanocrystals. A similar observation has also been reported recently.⁹⁸

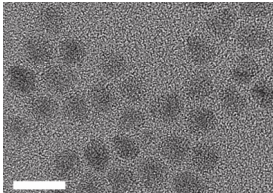
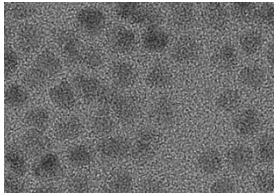
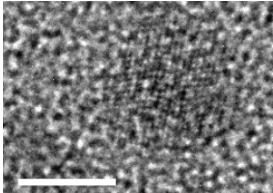
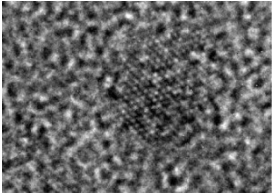
Number of precursor injections. Table 1 conditions d-f varies the number of precursor injections for similar total amount of precursors. When increasing the number of precursor injections, the quantum yield increases. Nanocrystals synthesized using condition f show the highest quantum yield with the shape of the nanocrystals closer to spherical. Condition f was used for the nanocrystals in Chapter V and VII. While the nanocrystals in our earlier studies (Chapter IV and VI) were prepared using condition a.

Table 1. Quantity of Sulfur and Zinc Precursor of Each Addition when Layering ZnS Shell.

| | a | | b | | c | |
|--|---|--|---|---------|--------|---------|
| | 0428b | | 0428c | | 0505b | |
| | S (mL) | Zn (mL) | S (mL) | Zn (mL) | S (mL) | Zn (mL) |
| Volume of precursor used for each injection ^a | 0.47 | 0.7 | 0.47 | 0.7 | 0.96 | 0.96 |
| | 0.7 | 0.95 | 0.7 | 0.95 | 1.29 | 1.29 |
| | 0.95 | 1.24 | 0.95 | 1.24 | 1.67 | 1.67 |
| | 1.24 | 1.58 | 1.24 | 1.58 | 2.1 | 4.2 |
| | 1.58 | 1.96 | 1.58 | 1.96 | | |
| Relative quantum yield | 0.70 | | 0.49 | | 0.17 | |
| TEM image (scale bar is 10 nm) |  |  |  | | | |
| Magnified TEM image (scale bar is 5 nm) |  |  |  | | | |

^aConcentrations of sulfur and zinc S and Zn precursors are both 0.25 M.

Table 1. (Continued)

| | d 0506a | | e 0506b | | f 0516i | |
|--|------------|---------|---|--|------------|---------|
| | S (mL) | Zn (mL) | S (mL) | Zn (mL) | S (mL) | Zn (mL) |
| Volume of precursor used for each injection ^a | 0.96 | 1.13 | 0.7 | 0.8 | 0.50 | 0.58 |
| | 1.3 | 1.5 | 0.9 | 1.05 | 0.67 | 0.77 |
| | 1.6 | 1.9 | 1.2 | 1.3 | 0.87 | 0.97 |
| | 2.1 | 4.2 | 1.5 | 1.65 | 1.08 | 1.20 |
| | | | 1.8 | 2 | 1.33 | 1.47 |
| | | | | 0.80 | 1.75 | |
| Relative quantum yield | 0.32 | | 0.58 | | 1.00 | |
| TEM image (scale bar is 10 nm) | N/A | |  |  | | |
| Magnified TEM image (scale bar is 5 nm) | N/A | |  |  | | |

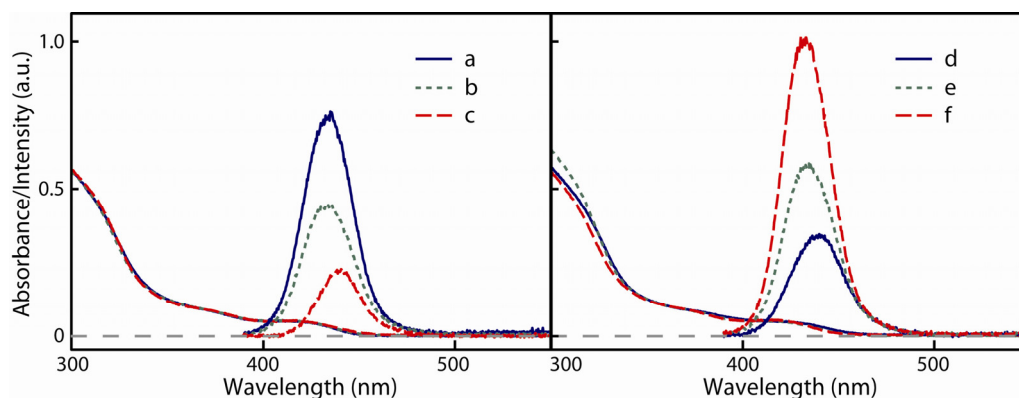


Figure 10. Absorption and luminescence (peaked at ~ 440 nm) spectra of the undoped CdS/ZnS nanocrystals with core size and shell thickness of 3.6 and ~ 1.8 nm, respectively. The luminescence spectra were taken using a CCD spectrometer (USB2000, Ocean Optics) without intensity calibration using a 370 nm light emitting diode as the excitation light source. The sample codes in the legends correspond to the synthesis conditions summarized in Table 1. The gray dashed line indicates 0 absorbance.

3.2 Absorption and Luminescence Spectra Measurement

3.2.1 Absorption Spectra

The absorption spectra were measured using a U-4100 UV-Vis-NIR spectrometer (Hitachi) or ISS-UV-VIS integrated sampling system coupled to USB2000 spectrometer (Ocean Optics). Spectra of the same sample taken with the two instruments are identical. For each measurement, the absorbance at the wavelengths necessary for the study (300 – 800 nm) is kept below 1 for linearity.

3.2.2 Photoluminescence Spectra and Quantum Yield Measurement

Unless specified, the photoluminescence spectra were taken with a Quanta Master spectrofluorometer (PTI) equipped with a xenon lamp and a photomultiplier tube. The built-in intensity calibration from PTI was used for each spectrum.

The luminescence quantum yield of the exciton (Φ_{ex}) and Mn (Φ_{Mn}) in undoped and Mn-doped nanocrystals were measured using either standard dye or CdSe/ZnS nanocrystals of known quantum yield as the reference material.⁹⁹ In all the measurements, hexane was used as the solvent for the nanocrystals, and 370 nm light was used as the excitation source. Φ_{ex} of both undoped and Mn-doped CdS/ZnS nanocrystals was measured using quinine sulfate in 1.0 N aqueous H₂SO₄ solution (quantum yield = 0.546)¹⁰⁰ as the reference dye. For the measurement of Φ_{Mn} , undoped CdSe/ZnS nanocrystals emitting at 600 nm were used as the reference material since no organic dye has a sufficiently large Stokes shift that matches the absorption and luminescence spectra of Mn-doped nanocrystals.⁹⁹ The quantum yield of undoped CdSe/ZnS reference nanocrystals was measured using rhodamine 101 dissolved in ethanol under nitrogen atmosphere (quantum yield = 1.00) with excitation at 550 nm.¹⁰¹ To confirm the validity of the quantum yield of the reference dyes, the quantum yields of the quinine sulfate and rhodamine 101 were cross-checked with coumarin 1 and cresyl violet, respectively. The quantum yield of coumarin 1 in 1:1 mixture of ethanol and water and the quantum yield of cresyl violet in methanol were obtained using quinine sulfate and rhodamine 101 as reference and were within 3% of the reported values, 0.30 and 0.66–0.67, respectively.^{102,103} The quantum yield of the samples was calculated using the relative intensity to the reference dye:

$$QY_s = QY_r \times \frac{I_s}{I_r} \times \frac{A_r}{A_s} \times \frac{n_r^2}{n_s^2} \quad (8)$$

where QY, I, A, and n are quantum yield, integrated luminescence intensity, absorbance at excitation wavelength, and refractive index of solvent, respectively. The subscripts s

and r are sample and reference, respectively. All the measurements were reproduced with less than 5% error.

3.3 Time-Dependent Mn Luminescence Intensity Measurement

The time-dependent Mn luminescence intensity was measured by exciting the Mn-doped nanocrystals dispersed in hexane with a pulsed nitrogen laser (pulse duration <3 ns, wavelength 337 nm). The Mn luminescence was selected by a monochromator, detected by a photomultiplier tube, and the signal was collected by a digital oscilloscope. Each time-dependent luminescence curve was fit to a two exponential function, and the averaged lifetime (τ_{Mn}) was calculated using the following equation, where a_1 and a_2 are the amplitude and t_1 and t_2 are the time constants of the two exponential fit.¹⁰⁴

$$\tau_{Mn} = (a_1 \times t_1^2 + a_2 \times t_2^2) / (a_1 \times t_1 + a_2 \times t_2) \quad (9)$$

3.4 Determination of Radial Doping Location in Mn-Doped CdS/ZnS Nanocrystals

The core diameter, doping location, and total diameter of Mn-doped CdS/ZnS nanocrystals were obtained by averaging the particle diameter in transmission electron micrograph (TEM) of the CdS core nanocrystals, CdS/ZnS nanocrystals before doping Mn²⁺ ions, and the final Mn-doped CdS/ZnS nanocrystals, respectively. The TEM of CdS core and CdS/ZnS nanocrystals before doping Mn²⁺ ions are in Figure 11 and the radii are summarized in Table 2.

To confirm the radii obtained from the TEM, we calculated the molar ratio of Zn²⁺ and Cd²⁺ ions per nanocrystal ($[Zn^{2+}]/[Cd^{2+}]$) from the radii of the nanocrystals and

compared with the $[\text{Zn}^{2+}]/[\text{Cd}^{2+}]$ obtained from elemental analysis (inductively coupled plasma mass spectrometry, ICP-MS). $[\text{Zn}^{2+}]/[\text{Cd}^{2+}]$ from radii was calculated using the following equations.

$$\frac{[\text{Zn}^{2+}]}{[\text{Cd}^{2+}]} = \frac{V_{\text{ZnS}} \times D_{\text{ZnS}} \div M_{\text{ZnS}}}{V_{\text{CdS}} \times D_{\text{CdS}} \div M_{\text{CdS}}} \quad (10)$$

where

$$V_{\text{ZnS}} = \frac{4}{3} \pi (r_{\text{total}}^3 - r_{\text{core}}^3)$$

$$V_{\text{CdS}} = \frac{4}{3} \pi r_{\text{core}}^3 \quad (11)$$

r_{total} and r_{core} are total and core radii of Mn-doped CdS/ZnS nanocrystals obtained from TEM. D_{ZnS} and D_{CdS} are the bulk density of ZnS and CdS (4.09 and 4.82 g/cm³, respectively).^{78,79} M_{ZnS} and M_{CdS} are molar mass of ZnS and CdS (97.47 and 144.46 g/mol, respectively). The results are compared in Table 2. The molar ratio of $[\text{Zn}^{2+}]/[\text{Cd}^{2+}]$ obtained using the two methods are reasonably close (~3% error in average).

To confirm the doping locations, we compared the volume ratio of ZnS ($V_{\text{ZnS}}^*/V_{\text{ZnS}}$) from TEM with that from absorption spectra, where V_{ZnS}^* and V_{ZnS} are the volume of ZnS per nanocrystal before doping the Mn^{2+} ions (samples in Figure 11b,c) and the final Mn-doped CdS/ZnS nanocrystals, respectively. The absorbance of nanocrystals at wavelengths much shorter than the bandgap (e.g., 300 nm) is proportional to the volume per nanocrystal due to the density of state of the energy levels involved in short wavelength excitation is nearly continuous.¹⁰⁵ The extinction coefficient is no longer affected by quantum confinement effect. Since our nanocrystal

samples are core/shell nanocrystals, the volume of ZnS shell is proportional to the absorbance of the CdS/ZnS nanocrystals subtracted by that of the CdS nanocrystals at the same nanocrystal concentration. Therefore, V_{ZnS}^*/V_{ZnS} from absorption spectra was calculated via

$$\frac{V_{ZnS}^*}{V_{ZnS}} = \frac{A_* - A_{CdS}}{A_{total} - A_{CdS}} \quad (12)$$

where A_{CdS} , A_* , and A_{total} were the absorbance of the CdS core nanocrystals, the CdS/ZnS nanocrystals before doping Mn^{2+} ions, and the final Mn-doped CdS/ZnS nanocrystals at 300 nm, respectively. The absorbance was obtained from absorption spectra normalized to the same nanocrystal concentration as shown in Figure 12.

V_{ZnS}^*/V_{ZnS} from TEM was calculated via

$$\frac{V_{ZnS}^*}{V_{ZnS}} = \frac{4/3\pi(r_*^3 - r_{core}^3)}{4/3\pi(r_{total}^3 - r_{core}^3)} \quad (13)$$

where r_* was the radius of CdS/ZnS nanocrystals before doping Mn^{2+} ions. The results are summarized in Table 2. Considering the value compared is volume, which is proportional to the cubic of radius, the differences in radius estimated from TEM, inductive coupled-plasma mass spectrometry (ICP-MS), and absorption spectra are less than 4%. The similar results from the above comparisons indicate that the determination of CdS core radius and doping location from TEM is reliable.

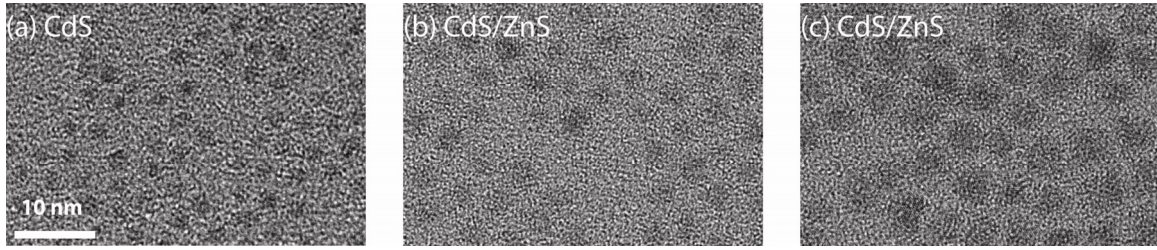


Figure 11. TEM images of (a) CdS core and (b) and (c) CdS/ZnS nanocrystals before doping Mn^{2+} ions for doping locations $d = 0.6$ and 1.2 nm, respectively. Scale bar is the same for all three images.

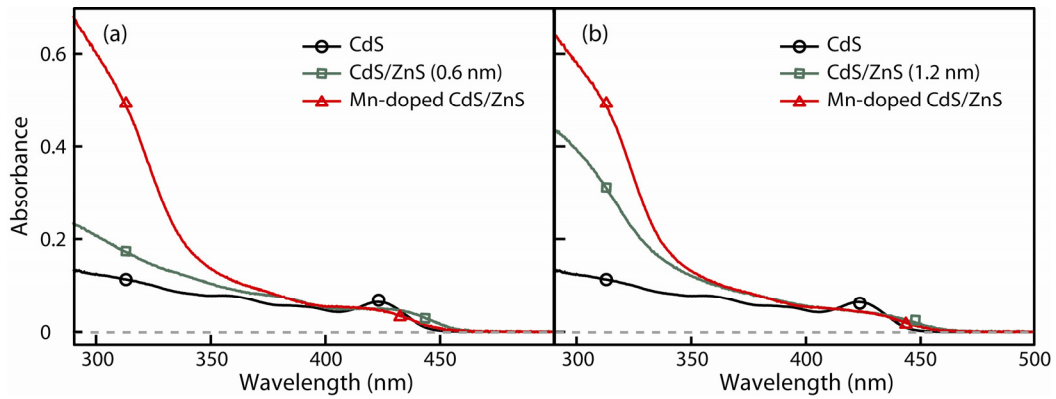


Figure 12. Absorption spectra of CdS core, CdS/ZnS nanocrystals before doping the Mn^{2+} ions, final Mn-doped CdS/ZnS nanocrystals. (a) and (b) are for doping location $d = 0.6$, 1.2 nm, respectively. Spectra are normalized to the same nanocrystal concentration.

Table 2. Radius of Core (r_{core}), CdS/ZnS before Doping (r^*) and Final Mn-Doped CdS/ZnS Nanocrystals (r_{total}). Comparison of Cation Molar Ratio ($[\text{Zn}^{2+}]/[\text{Cd}^{2+}]$) and ZnS Volume Ratios ($V_{\text{ZnS}^*}/V_{\text{ZnS}}$).

| sample | Radius from TEM | | | $[\text{Zn}^{2+}]/[\text{Cd}^{2+}]$ | | | $V_{\text{ZnS}^*}/V_{\text{ZnS}}$ | | |
|----------------|-----------------------------|-------------------------------|----------------------------|-------------------------------------|---------------------|-----------|-----------------------------------|---------------------|-----------|
| | r_{core}^a (nm) | r^* (nm) | r_{total} (nm) | TEM | ICP-MS ^b | Error (%) | TEM | Absorp-tion spectra | Error (%) |
| undoped | 1.8 ₀ | | 3.6 ₄ | 9.1 | 9.4 | -3 | | | |
| a1 | 1.8 ₀ | 1.8 ₀ | 3.5 ₁ | 8.1 | 8.9 | -10 | | | |
| b1 | 1.8 ₀ | 2.4 ₀ ^b | 3.5 ₉ | 8.7 | 8.7 | 0 | 0.20 | 0.17 | 13 |
| c1 | 1.8 ₀ | 3.0 ₀ ^c | 3.5 ₂ | 8.2 | 8.2 | 0 | 0.56 | 0.59 | -5 |

^{a-c} Samples of Figure 11a-c, respectively.

3.5 Determination of the Doping Concentration and Extinction Coefficient

The average number of Mn^{2+} ions per nanocrystal, $\langle n_{\text{Mn}} \rangle$, was determined from the elemental analysis employing ICP-MS and particle size from TEM. The best concentration range of the ICP-MS measurement is 50-100 ppb for each element. The ICP-MS sample was prepared by taking 1 mL of hexane solution of the Mn-doped CdS/ZnS nanocrystals with absorbance ~ 0.1 at 430 nm. The solution was dried under nitrogen flow, and the nanocrystals were digested in trace metal grade concentrated nitric acid (Fisher Scientific) under sonication for ~ 10 min. The nitric acid solution was centrifuged to separate the remaining organics from the solution. The solution was diluted ~ 20 times with 1% nitric acid in Millipore water for the determination of manganese ion concentration, and further diluted to ~ 300 times for the determination of cadmium and zinc ion concentration. In addition, two sets of standard solutions, cadmium ion with zinc ion (20, 50, 100, 200, and 400 ppb) and manganese ion (2, 20, 50, and 100 ppb), were prepared by diluting the 1 ppm ICP standard solution (Aldrich) to establish the calibration curves for the determination of the ion concentration. At each step, the amount of solution taken was carefully weighted with 4 decimal digits of precision to calculate the dilution factor.

After obtaining the cadmium and manganese ion molar concentration of the initial hexane solution ($[\text{Mn}^{2+}]$ and $[\text{Cd}^{2+}]$, respectively), $\langle n_{\text{Mn}} \rangle$ was calculated from

$$\langle n_{\text{Mn}} \rangle = [\text{Mn}^{2+}] / [\text{NC}]$$

$[\text{NC}]$ is the concentration of nanocrystals, calculated from $[\text{Cd}^{2+}] / \langle n_{\text{Cd}} \rangle$, where $\langle n_{\text{Cd}} \rangle$ is the average number of Cd^{2+} ions per nanocrystal. $\langle n_{\text{Cd}} \rangle$ for the CdS nanocrystals used in

all of the study is 491, which was calculated from the volume of the CdS nanocrystals. The volume was obtained from the particle diameter (3.6 nm) measurement using TEM. The ICP-MS measurement of each sample was taken at least three times, and the error of $\langle n_{Mn} \rangle$ is $\sim 8\%$.

The extinction coefficient of the nanocrystals can be calculated after obtaining the original nanocrystals concentration in the initial hexane solution described in the previous paragraph. The extinction coefficient (ϵ) is then calculated using Beer's law,

$$\epsilon = A/(b \cdot [NC])$$

where A is the absorbance of the initial hexane solution of the nanocrystals, and b is 1 cm.

3.6 Crystal Structure of the Nanocrystals

The crystal structure of the CdS nanocrystals and Mn-doped CdS/ZnS nanocrystals were determined by comparing the powder x-ray diffraction (XRD) pattern of the nanocrystals with the bulk CdS and ZnS from the database. The powder XRD was taken using radiation from Cu source with wavelength of 1.5406 Å. As seen in Figure 13, the CdS nanocrystals had the same diffraction pattern and angle as the bulk zinc blende CdS, indicating the crystal structure of CdS nanocrystals was zinc blende. After overcoating the ZnS, instead of forming separate peaks, the diffraction angle shifted to larger angles toward the bulk zinc blende ZnS. These observations indicate that ZnS grows on the CdS core and follows the crystal structure, consistent with the larger average nanocrystal diameter from TEM.

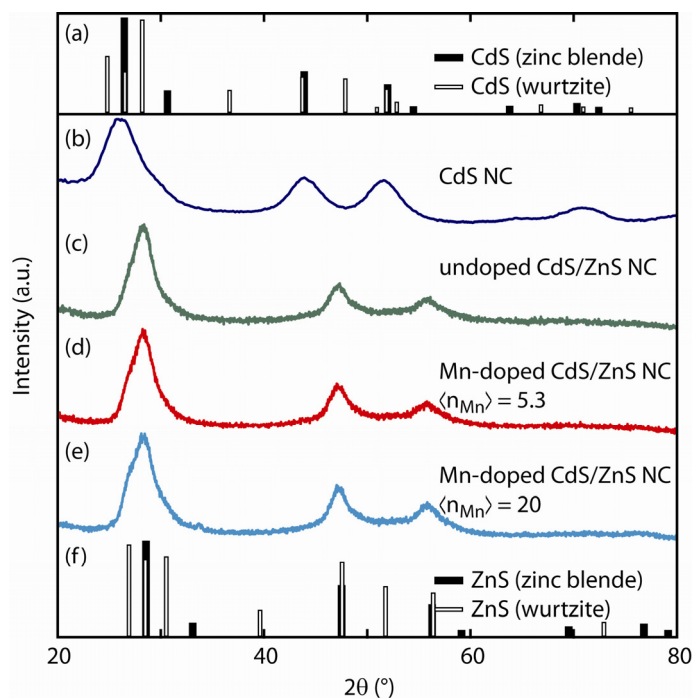


Figure 13. Comparison of x-ray diffraction patterns of (b) CdS nanocrystals and (c) undoped and (d), (e) Mn-doped CdS/ZnS nanocrystals with Mn^{2+} ions doped at the core/shell interface. Bulk (a) CdS and (f) ZnS from database.

3.7 Transient Absorption Measurement

Time-dependent transient absorption ($\Delta\text{OD}(t)$) measures the change of excited state absorbance with time from the ground state, which represents the time-dependent population of the excited state. Experimentally, the excited state is generated using a pump beam, and the absorbance was measured with a probe beam. To synchronize the two beams, the two beams are obtained by splitting a femtosecond pulse laser beam into two. The pump-probe delay time is varied using a translation stage that changes the length of the pump beam path traveled before reaching the sample. The wavelength of both the pump and probe pulses may be varied using the frequency mixing crystal, and

the interested wavelengths are selected using prisms and a slit. Depending on the wavelength of the pulses, dynamics of different processes can be monitored.

The experimental setup of the transient absorption measurement is depicted in Figure 14. The pump pulse at 395 nm was generated by frequency doubling of 790 nm output from a Ti:sapphire laser in a β -barium borate crystal at repetition rate of 3 kHz. The pulse width of the pump beam was 70 fs. The pump beam diameter at sample was varied depending on the excitation density. The pump intensity was also varied using a pair of the half waveplate and polarizer. White light continuum generated in 1 mm-thick CaF₂ or sapphire window by focusing 790 nm beam was used as the probe light (fwhm beam diameter \sim 30 μ m) at band-edge (420 nm) or near infrared (880 nm) regions, respectively. When CaF₂ was used, the window was translated rapidly to obtain a stable continuum probe light. The hexane solutions of the sample nanocrystals were circulated in a 1 mm-thick quartz liquid cell at the linear flow rate of \sim 1 m/s or as a free streaming jet at the linear flow rate of a few m/s to avoid potential photo-damage and reexcitation of the same sample area. Fast circulation is particularly important for Mn-doped nanocrystals since the lifetime of Mn excited ligand field state is several ms.

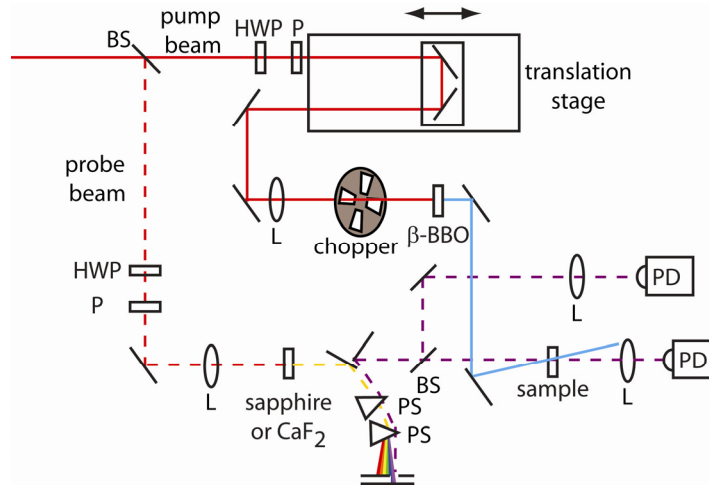


Figure 14. Experimental setup of the transient absorption measurement. BS: beam splitter, HWP: half waveplate, L: lens, P: polarizer, PD: photodiode, PS: prism, and β -BBO: beta-barium borate crystal. The solid and dashed lines are the pump and probe beams, respectively.

3.8 Calculation of Excitation Density

The exciton density is obtained from the number of photons absorbed per particle within the probe volume using the following equations.

$$\langle n_{ex} \rangle = \frac{Photon_{abs}}{\#_{Particle}}$$

$$Photon_{abs} = \frac{f_i - f_t}{E_{photon}} \times S_{probe}$$

$$\#_{Particle} = [NC] \times V_{probe} \times N_A$$

where

$\langle n_{ex} \rangle$ = average excitation density, or number of photon absorbed per nanocrystal

$Photon_{abs}$ = number of photons absorbed per pulse within the probe zone

f_i = incident pump fluence

f_t = transmitted pump fluence

E_{photon} = energy per photon (5.03×10^{-19} J/photon for 395nm)

S_{probe} = area of the probe zone = πr^2 , r (half of probe fwhm) = $15 \mu\text{m}$

V_{probe} = solution volume in the probe zone, $V_{\text{probe}} = \pi r^2 t$, t (sample thickness)

[NC] = nanocrystal concentration

N_A = Avogadro's number

The average excitation density ($\langle n_{\text{ex}} \rangle$) was defined as the number of photon absorbed divided by the number of particles within the probe volume. Here, number of photons absorbed was calculated from pump fluence absorbed by the sample (jet or flowing cell with thickness of $400 \mu\text{m}$ or 1mm , respectively) under the probe area using 2D Gaussian profile. (See Figure 15) In the measurement of transmitted pump fluence, small reflection loss ($<3\%$) was not considered in the calculation of the absorbed number of photons. The particle concentration of the nanocrystals was determined from the average diameter of the nanocrystals measured from TEM and total metal ion concentration measured from elemental analysis employing ICP mass spectrometry as discussed in section 3.5. Number of nanocrystals within the probe volume was calculated from particle concentration of the solution, [NC], and volume of probed zone, V_{probe} .

Pump beam size: 300 or 160 μm (fwhm)
Probe beam size: 31 μm (fwhm)

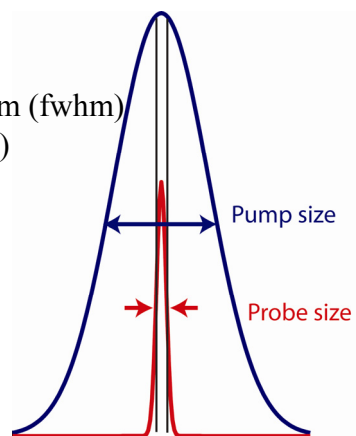


Figure 15. Estimation of pump fluence using 2D Gaussian profile.

CHAPTER IV

MEASUREMENT OF ENERGY TRANSFER TIME IN COLLOIDAL Mn-DOPED SEMICONDUCTOR NANOCRYSTALS*

4.1 Introduction

Semiconductor nanocrystals doped with paramagnetic transition metal ions, such as Mn-doped CdS nanocrystals, possess unique optical and magnetic properties distinct from their undoped counterparts that arise from the interaction of exciton with dopant ions.^{1,4,10,11} For instance, the doped Mn²⁺ ions can function as an efficient and long-lived sensitized energy reservoir for the excitons created in semiconductor host matrix via energy transfer from exciton to the ligand field state of Mn²⁺ ions.^{6,106} The energy transfer from exciton to dopant ions is essentially an intersystem crossing and results in strong phosphorescence luminescence from the ligand field transition of dopant ions.⁴ In Mn-doped II-VI semiconductor nanocrystals, phosphorescence of Mn²⁺ occurs near 600 nm with lifetime of $\sim 10^{-3}$ s.^{4,78,79} Due to the significant spatial overlap of the exciton and dopant wavefunctions in confined space of the nanocrystals, the energy of exciton can be rapidly transferred to Mn²⁺ ions competing with both radiative and nonradiative exciton relaxation pathways.^{4,70} For this reason, Mn-doped semiconductor nanocrystals often

*Reprinted in part with permission from Chen, Hsiang-Yun; Chen, Tai-Yen; Son, Dong Hee. Measurement of Energy Transfer Time in Colloidal Mn-Doped Semiconductor Nanocrystals. *J. Phys. Chem. C* **2010**, *114* (10), 4418-4423. Copyright 2010 by the American Chemical Society.

exhibit a superior luminescence quantum yield than undoped counterparts making them attractive for many applications.^{15,59,68,99}

Many earlier studies investigated the mechanisms of energy transfer and static and dynamic phosphorescence from Mn^{2+} ions resulting from the energy transfer.^{70,84,106,107} However, the rate of energy transfer from exciton to Mn^{2+} ions, a key factor determining the effectiveness of Mn-doped nanocrystals as the sensitized energy reservoir, has been investigated much less. Earlier studies employing time-resolved luminescence and transient absorption suggested the exciton-Mn energy transfer time is in the range of several tens to hundreds of ps in colloidal Mn-doped nanocrystals.^{93,94} However, difficulties in controlling the doping site and complications arising from the multiple emitting species (e.g. free and trapped exciton) posed challenges in obtaining a quantitative understanding of the energy transfer time.

Recently, studies on the radial doping position-dependent Mn luminescence intensity in Mn-doped CdS/ZnS nanocrystals showed that the quantum yield of Mn luminescence increases as the doping position gets closer to the center of the nanocrystal.⁷⁰ This result is consistent with the predictions from the possible energy transfer mechanisms (Förster, Dexter or Auger like mechanism),^{4,70,107} while the exact energy transfer mechanism is still not entirely clear. The energy transfer rate could not be obtained, however, from this steady-state quantum yield measurement due to uncertainties in the rates of other competing nonradiative processes.

In this report, we describe the time-resolved measurement of the energy transfer in Mn-doped CdS/ZnS core/shell nanocrystals with well-defined doping radius and

concentration, which will enable the correlated study of the energy transfer rate and the structure of the doped nanocrystals. To obtain information on the time scale of the energy transfer, we compared the exciton relaxation dynamics in Mn-doped and undoped nanocrystals as a function of Mn doping concentration at a known fixed radial doping position. The transient absorption signal from the photoexcited exciton decayed faster with the increase of Mn doping concentration due to the energy transfer. The energy transfer rate was linear to the Mn doping concentration at the average exciton density of 1 per particle. This allowed us to extract the energy transfer time for a single pair of exciton and Mn^{2+} ion at a given radial doping position. Exciton relaxation dynamics were obtained by probing at near IR region, where the transient absorption signal is primarily attributed to the intraband transition of excitons. Near IR probing has an advantage over visible probing of interband exciton absorption since the transient absorption signal at near IR increases linearly with exciton density within a wide range of exciton densities without saturation or cancellation of the signal. Transient absorption data of the nanocrystals with varying Mn doping concentrations (3.4 - 22 Mn^{2+} ions per particle) were analyzed to extract the energy transfer time with a simple kinetic model, where the energy transfer competes with exciton relaxation and trapping at the rate proportional to Mn doping concentration. The strategy to obtain a quantitative energy transfer time in Mn-doped semiconductor nanocrystals with a well-defined doping radius and concentration described here will be useful in obtaining an quantitative understanding of the correlation between the doping structure of the nanocrystals and the rate of energy transfer.

4.2 Results and Discussion

In order to investigate the rate of exciton-dopant energy transfer, we used spherical colloidal Mn-doped CdS/ZnS core/shell nanocrystals where Mn^{2+} ions are radially doped at a known distance from the center of the nanocrystals. The average diameter of the Mn-doped CdS/ZnS nanocrystals determined from TEM was 5.1 nm with CdS core diameter of 3.6 nm. Mn^{2+} ions were doped at 0.3 nm from the core/shell interface. (Figure 16) In all the undoped and doped nanocrystals, the diameter of CdS core, thickness of ZnS shell and Mn doping position were kept identical.

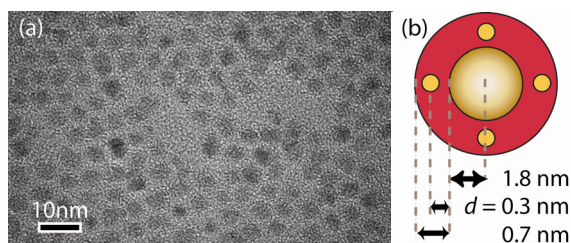


Figure 16. (a) TEM images of Mn-doped CdS/ZnS nanocrystals. (b) Dimensions of Mn-doped CdS/ZnS core/shell nanocrystals. CdS core radius and ZnS shell thickness is 1.8 nm and 0.7 nm respectively. Mn^{2+} ions are doped at $d = 0.3$ nm.

The average number of Mn^{2+} ions per particle, $\langle n_{\text{Mn}} \rangle$ was measured from the elemental analysis employing inductively coupled plasma mass spectrometry (ICP-MS). In this work, nanocrystal samples with $\langle n_{\text{Mn}} \rangle = 0, 3.1, 5.4, 6.8$ and 22 were prepared. Absorption and luminescence spectra of the undoped and Mn-doped CdS/ZnS nanocrystals are shown in Figure 17a. The absorption spectra of the nanocrystals with different $\langle n_{\text{Mn}} \rangle$ are very similar, which further indicates the uniformity of the core size and shell thickness of all the nanocrystal samples. Photoluminescence spectra of all four

samples were measured with 370 nm excitation. The lifetime of Mn phosphorescence measured with ns-pulsed excitation at 337 nm from N₂ laser was in the range of 2 - 6 ms and decreased with increasing $\langle n_{\text{Mn}} \rangle$ as shown in Figure 17b. The intensity of Mn phosphorescence increased with a concomitant decrease of band-edge exciton fluorescence as $\langle n_{\text{Mn}} \rangle$ increased at low doping concentrations. A small amount of red-shift of Mn phosphorescence with increasing $\langle n_{\text{Mn}} \rangle$ ascribed to Mn-Mn exchange interaction, is consistent with the previously reported observations.^{84,108}

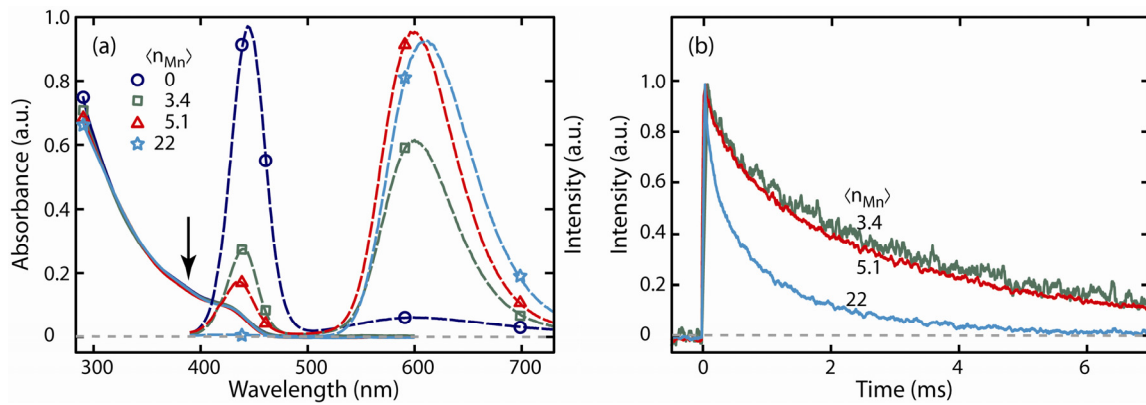


Figure 17. (a) Absorption (solid) and luminescence spectra (dashed) of Mn-doped CdS/ZnS core/shell nanocrystals with different Mn doping level. The arrow indicates the pump wavelength for transient absorption measurements. (b) Time dependent Mn phosphorescence intensity following 337 nm excitation. $\langle n_{\text{Mn}} \rangle$ is labeled in the figure.

In order to extract the energy transfer time from the comparison of the dynamics of exciton relaxation in undoped and doped nanocrystals, we obtained transient absorption data of CdS/ZnS nanocrystals with varying doping concentrations. When investigating the dynamics of exciton relaxation of CdS or CdSe nanocrystals from transient absorption measurements, typically the bleach signal of the band-edge exciton

absorption in visible spectral region is monitored at low exciton densities, e.g. less than one exciton per particle.^{44,45,49,109} At higher exciton densities, however, the bleach signal saturates and can even be partially masked by an absorptive contribution arising from multiexciton interaction or trapped exciton.^{46,110} This limits the usefulness of probing the bleach of interband exciton transition as a way to monitor the exciton relaxation dynamics to the low exciton density region. On the other hand, the pump-induced absorption in near IR region significantly below the bandgap does not suffer from the saturation of the bleach signal or cancellation of bleach by other absorptive signals. Furthermore, the initial amplitude of the pump-induced absorption near zero time delay increases more linearly to the exciton density within a wide range of exciton densities.¹¹¹ Therefore, monitoring the pump-induced absorption at near IR region can be more useful when the examination of the exciton relaxation dynamics in a wide range of exciton densities is required.

In this study, all the transient absorption (ΔOD) data were obtained at the probe wavelength of 880 nm (1.4 eV), lower in energy than the band-edge absorption of the undoped and Mn-doped CdS/ZnS nanocrystals investigated in this work (2.9 eV). Figure 19 shows ΔOD data of undoped CdS/ZnS core/shell nanocrystals probed at 880 nm at the average exciton densities of $\langle n_{ex} \rangle = 1, 14$ and 22 per particle. ΔOD data probed at other near IR wavelengths in 700-900 nm range were similar to the data obtained at 880 nm, indicating that the induced absorption in this region has a relatively flat spectral feature. (Figure 18) The comparison of ΔOD at zero time delay for the case of $\langle n_{ex} \rangle = 1$ ($\Delta OD < 0.002$) in Figure 19 and the linear absorption spectrum of the nanocrystal

sample shown in Figure 17a indicates that the transition probed at near IR is more than an order of magnitude weaker than interband exciton transition (e.g. OD = 0.1 at $\lambda = 420$ nm). The pump-induced absorption in this spectral region was previously interpreted as the intraband absorption of the exciton.¹¹¹ While the assignment of the absorption at 880 nm is more complex than the spectroscopic features in visible or mid IR region more readily associated with a particular inter or intraband transition, the dynamics at 880 nm can be interpreted as the relaxation of the excited excitons in an averaged sense.¹¹¹ Therefore, the dynamics of exciton relaxation reflected in ΔOD data of this study represents the collective dynamics of all the excitons rather than the relaxation of the band-edge exciton only.

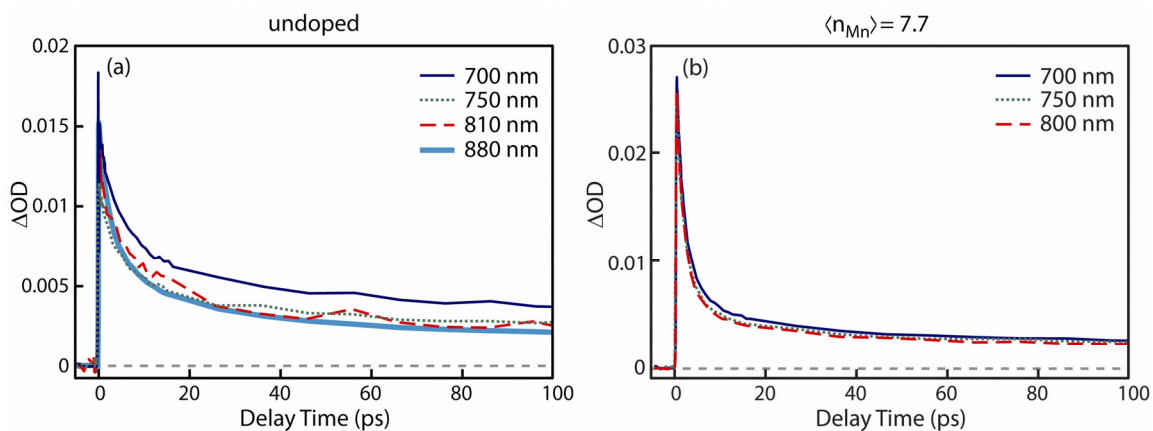


Figure 18. Transient absorption data for (a) undoped and (b) Mn-doped ($\langle n_{Mn} \rangle = 7.7$) CdS/ZnS core/shell nanocrystals measured with pump wavelength 390 nm at $\langle n_{Mn} \rangle = 24$ and probe at 700 - 880 nm as indicated in the legend. The data probed at 700 - 880 nm shows similar decaying feature, indicating the induced absorption signal is independent of probing wavelength in this spectral region.

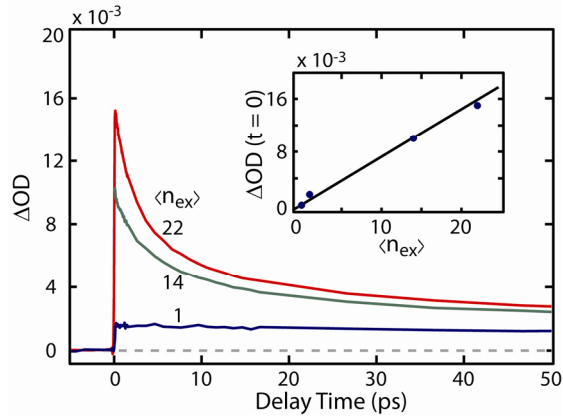


Figure 19. Transient absorption data of undoped CdS/ZnS core/shell nanocrystals under various exciton densities ($\langle n_{ex} \rangle$) obtained with 390 nm pump and 880 nm probe. The inset displays the peak amplitude of ΔOD data vs. $\langle n_{ex} \rangle$.

In Figure 19, the peak amplitude of ΔOD data near zero time delay increases near-linearly with the exciton density as shown in inset. This linearity of the signal to the exciton density allows us to monitor the exciton relaxation dynamics within a broad range of exciton densities. The highly multiexponential feature of the dynamics at higher exciton densities can be explained with Auger relaxation of excitons.^{112,113} The accurate modeling of ΔOD data in Figure 19, especially at higher exciton densities, is somewhat complex. It requires information on all the radiative and nonradiative exciton relaxation pathways (e.g. trapping of exciton) and absorption cross sections of all the processes resonant at the probe wavelength, which are not always unambiguous. However, information on the time scale of exciton-dopant energy transfer can be obtained from the comparative analysis of ΔOD data, since the energy transfer is manifested in the ‘difference’ of the exciton relaxation dynamics of doped and undoped nanocrystals. At lower exciton densities (e.g., $\langle n_{ex} \rangle < 1$), such comparative analysis is more

straightforward since the dynamics of exciton relaxation is simpler without highly nonlinear Auger relaxation.

Built upon the robustness of transient near IR absorption as the probe for the exciton relaxation dynamics as discussed above, we first investigated the energy transfer time at the average exciton density of $\langle n_{\text{ex}} \rangle = 1$. To extract the time scale of exciton-dopant energy transfer from the comparative analysis of exciton relaxation dynamics, we measured ΔOD of Mn-doped CdS/ZnS nanocrystals with varying Mn doping concentration. Figure 20a compares ΔOD data of the undoped and doped nanocrystals with $\langle n_{\text{Mn}} \rangle = 5.1, 22$ probed at 880 nm at the average exciton density of $\langle n_{\text{ex}} \rangle = 1$. The decay of ΔOD can be fit to one or two exponential functions. The amplitude of ΔOD at zero time delay is not very sensitive to Mn doping concentration $\langle n_{\text{Mn}} \rangle$, which indicates that a common spectroscopic process is probed in all nanocrystal samples. Such independence of ΔOD at zero time delay on $\langle n_{\text{Mn}} \rangle$ was maintained at higher exciton densities as will be shown later, further demonstrating the usefulness of near IR probe. (See Figure 23 on page 69.) When ΔOD data is measured in visible region ($\lambda = 455$ nm) near the band-edge exciton transition, on the other hand, the bleach signal at zero time delay exhibits a signature of an absorptive component partially cancelling the bleach signal especially in the sample with a high level of Mn doping, Figure 21) This also makes near IR probing of intraband transition more attractive for the study of exciton-dopant energy transfer.

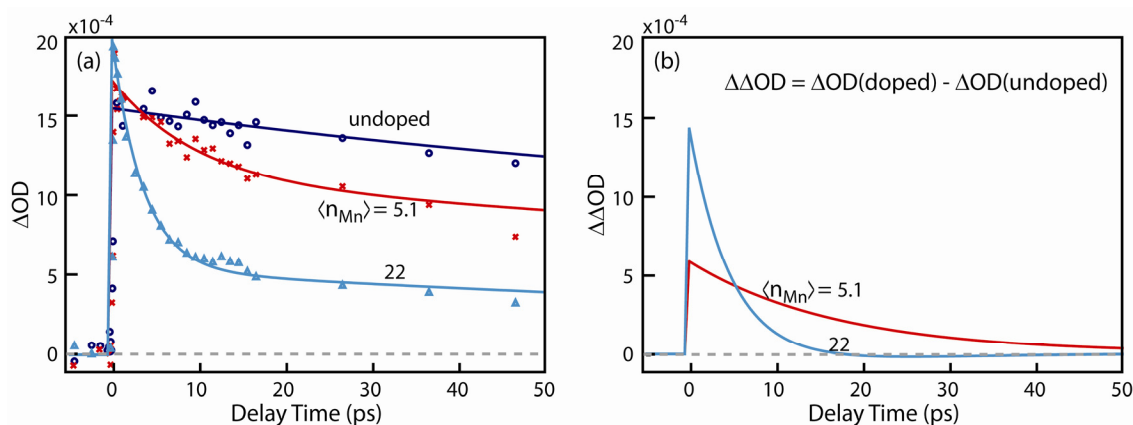


Figure 20. (a) Transient absorption data of undoped and Mn-doped CdS/ZnS nanocrystals obtained with 390 nm pump and 880 nm probe at $\langle n_{ex} \rangle = 1$. Experimental data (symbol) and fit to exponential functions (solid line). (b) $\Delta\Delta OD$ data of $\langle n_{Mn} \rangle = 5.1$ and 22 samples.

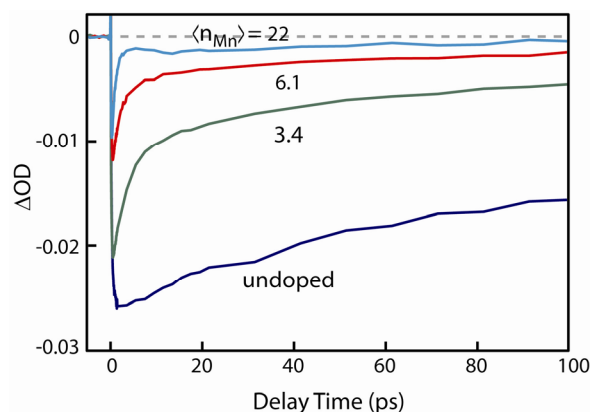


Figure 21. Transient absorption data of Mn-doped CdS/ZnS core/shell nanocrystals measured with pump wavelength 390 nm at $\langle n_{ex} \rangle = 1$ and probe wavelength 455 nm, which is slightly longer than the band edge absorption. $\langle n_{Mn} \rangle$ is shown in the legend. The bleach signal at zero time delay was partially canceled by an absorptive component, especially in the sample with a high level of Mn doping.

In Figure 20a, the time scale of the fast decaying component in ΔOD data becomes shorter as $\langle n_{Mn} \rangle$ increases. We attribute the increasingly faster decay of ΔOD with increasing $\langle n_{Mn} \rangle$ to the energy transfer from exciton to Mn^{2+} ions. In order to extract

the time scale of the energy transfer, we first employed a simple subtractive procedure without fitting the data to a detailed kinetic model with all the radiative and nonradiative exciton relaxation pathways. Figure 20b displays the difference between the two ΔOD data ($\Delta\Delta OD$) from the doped and undoped nanocrystal samples, where the subtraction was performed after normalizing the data to the amplitude of the slowly decaying component that has the time constant of ~ 800 ps. This procedure is sufficient for obtaining a rough time scale of the energy transfer since ΔOD of undoped nanocrystals decays at a much slower rate compared to the time scale of the fast decaying component in ΔOD of doped nanocrystals. We interpret the time scale of the decay of $\Delta\Delta OD$ as the energy transfer time from exciton to dopant states for a given Mn^{2+} concentration. From the fit to a single exponential function, 18 ps and 4 ps were obtained for $\langle n_{Mn} \rangle = 3$ and 13 respectively. The ratio of the two times is close to the ratio of $\langle n_{Mn} \rangle$, which is expected from the first order energy transfer kinetics between an exciton and multiple Mn^{2+} ions. Extrapolation of the energy transfer time to the case of $\langle n_{Mn} \rangle = 1$ yields $\tau_{ET} = \sim 53$ ps for a single pair of exciton and Mn^{2+} ion in our CdS/ZnS core/shell nanocrystals at the doping radius of 2.1 nm. According to the earlier studies on bulk Mn-doped semiconductors and self-assembled Mn-doped quantum dots, the energy transfer between the exciton and dopant occurred on the time scale of tens of ps.^{89,91} In colloidal Mn-doped nanocrystals, Chung *et al.* reported 700 ps energy transfer time in aqueous colloidal solution of 2% Mn-doped ZnS nanocrystals from the comparison of the decay time of exciton luminescence and rise time of 4T_1 (Mn^{2+}) absorption at an unspecified exciton density.⁹³ Olano *et al.* observed the difference in transient absorption data between undoped and

Mn-doped ZnSe nanocrystals, which exhibited the presence of an energy transfer channel in doped nanocrystals with the time constants of tens of ps.⁹⁴ Although the direct comparison cannot be made between our and earlier measurements due to the uncertainties in the effective doping density and donor-acceptor distance in the earlier works, the time scales of the energy transfer are of the same order of magnitude except Chung *et al.*'s work.

While the above analysis offers a simple way to obtain the approximate time scale of the energy transfer, it does not account for some detailed features in ΔOD data. For instance, a persistent and slowly decaying component ($\tau = \sim 800$ ps) in ΔOD data, whose amplitude decreases with increasing $\langle n_{Mn} \rangle$ is ignored in the analysis. One possible explanation for the slowly decaying component is the absorption from the trapped exciton.¹¹⁰ According to the earlier studies in CdS and CdSe nanocrystals, electron and hole trapping was considered to occur on the times scale of sub ps to tens of ps depending on the size and surface passivation of the nanocrystals.^{44,46,110} Since the trapping will localize the wavefunction of the electron or (and) hole at the defect site and lower the energy of exciton, the energy transfer from trapped exciton to Mn^{2+} ions will be inefficient. If the trapped exciton has an absorption at the probe wavelength, competition between the energy transfer and exciton trapping can explain the observed slowly decaying component in ΔOD data, whose amplitude decreases with increasing $\langle n_{Mn} \rangle$. □ □

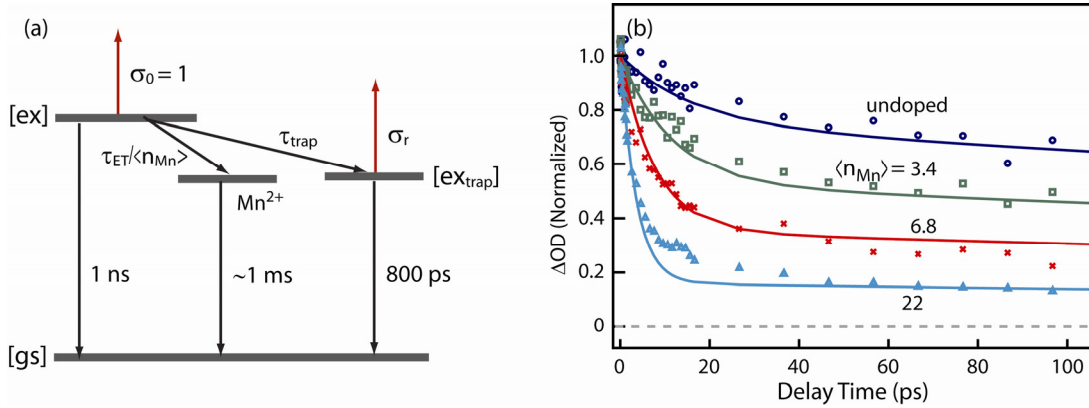


Figure 22. (a) Kinetic scheme used for modeling of energy transfer competing with radiative and nonradiative relaxation (trapping) of exciton in Mn-doped CdS/ZnS nanocrystals. [gs], [ex] and [ex_{trap}] represent ground state, excited state (exciton), and trapped excited state (trapped exciton). The fitting parameters are τ_{ET} , τ_{trap} and σ_r . See the text. (b) Experimental data (symbol) and fit (solid line) of the data to the kinetic model.

In order to extract the more refined energy transfer time taking into account the competition between the energy transfer and trapping, we fitted ΔOD data of Mn-doped nanocrystals of four different $\langle n_{Mn} \rangle$ to the kinetic model shown in Figure 22a. Three parameters, τ_{ET} , τ_{tr} and σ_r , were optimized in the fitting. τ_{ET} and τ_{tr} represent the energy transfer time between a pair of exciton and Mn^{2+} ion and exciton trapping time respectively. σ_r is the absorption cross section of the trapped exciton relative to the initially excited exciton. All four normalized ΔOD data were simultaneously fitted to $OD(t) = [ex](t) + \sigma_r[ex_{trap}](t)$ with the initial condition of $[ex](0) = 1$, where $[ex](t)$ and $[ex_{trap}](t)$ are the population of the initially excited and trapped exciton state at time t respectively. Here, the apparent time scale of the energy transfer was assumed to be linear to $\langle n_{Mn} \rangle$. Since the fitting of the data and the optimized parameters are very insensitive to the decay times of [ex] and [ex_{trap}] that account for the slowly decaying

component on ~ 1 ns time scale, we used the fixed time constants for these processes. In fact, the extracted rate parameters vary only 3% when the time constants for the decay of $[ex]$ and $[ex_{\text{trap}}]$ were varied from 1 to 10 ns.

Figure 22b shows the fitting result with optimized parameters of $\tau_{\text{ET}} = 102$ ps $\tau_{\text{tr}} = 17$ ps and $\sigma_{\text{r}} = 0.75$. With the inclusion of exciton trapping time and the absorption of trapped exciton as the additional parameters, the amplitude of the slow-decaying component is reasonably well reproduced for all four Mn doping concentrations. The value of τ_{ET} extracted from this more refined analysis is not significantly different from the value obtained from the analysis shown in Figure 20, suggesting that the simple subtractive analysis can also capture the approximate time scale of the energy transfer. It is interesting to note that the optimized trapping time (τ_{tr}) is within the range of electron and hole trapping times from earlier works on CdS and CdSe nanocrystals.^{44,110} While the data from our study is insufficient to unambiguously determine the nature of trapping and the absorption from trapped exciton, the model works well for the purpose of extracting the time scale of the energy transfer.

In order to further examine the possibility of extending near IR probe to study the time scale of the energy transfer at higher exciton densities, we measured ΔOD at higher excitation fluences corresponding to $\langle n_{\text{ex}} \rangle = 14$. ΔOD data of undoped and Mn-doped ($\langle n_{\text{Mn}} \rangle = 22$) nanocrystals are compared in Figure 23, where the doped nanocrystals exhibit the faster decay of the signal. In fact, the faster decay of ΔOD with increasing $\langle n_{\text{Mn}} \rangle$ was observed as a general trend. (Figure 24) Modeling the decay of ΔOD signal at higher exciton density and extracting the energy transfer time is, however, more

complex than the low exciton density case due to the highly nonlinear Auger relaxation kinetics.

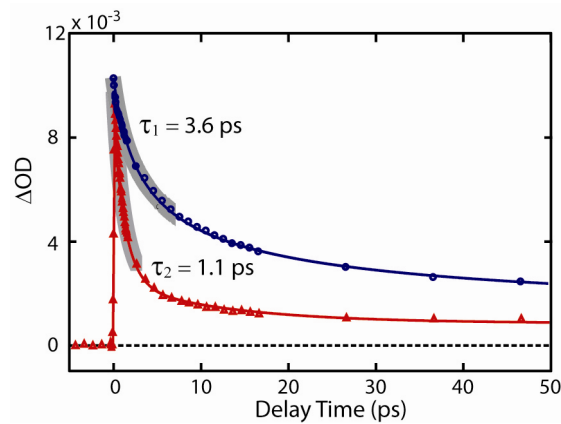


Figure 23. Transient absorption data of undoped and Mn-doped CdS/ZnS core/shell nanocrystals with $\langle n_{ex} \rangle = 14$. Experimental data (symbol) and fit (solid lines) are shown for $\langle n_{Mn} \rangle = 0$ (circle) and 22 (triangle). The time constants τ_1 and τ_2 were obtained from multi exponential fitting of the data.

Here, we make a simple comparison of the exponential decay times at early delay time (<10 ps) only without attempting to make a detailed kinetic analysis. In Figure 23, the exponential time constants in the shaded regions are 3.6 ps and 1.1 ps carrying about 50% and 70% of the amplitude for undoped and doped ($\langle n_{Mn} \rangle = 22$) nanocrystal samples respectively. Treating these time constants as the first-order time constants, one obtains an approximate time constant of 1.6 ps for the additional first order process in the doped nanocrystal that can be ascribed to the energy transfer.²⁰ This can be crudely interpreted as $\tau_{ET} = 20$ ps for a single Mn^{2+} ion at this excitation condition. This suggests that despite the fast Auger relaxation of excitons at higher exciton densities, the energy transfer is sufficiently fast to compete with Auger relaxation. More detailed discussion

on the measurement and analysis of energy transfer at higher exciton densities will be made in a future report.

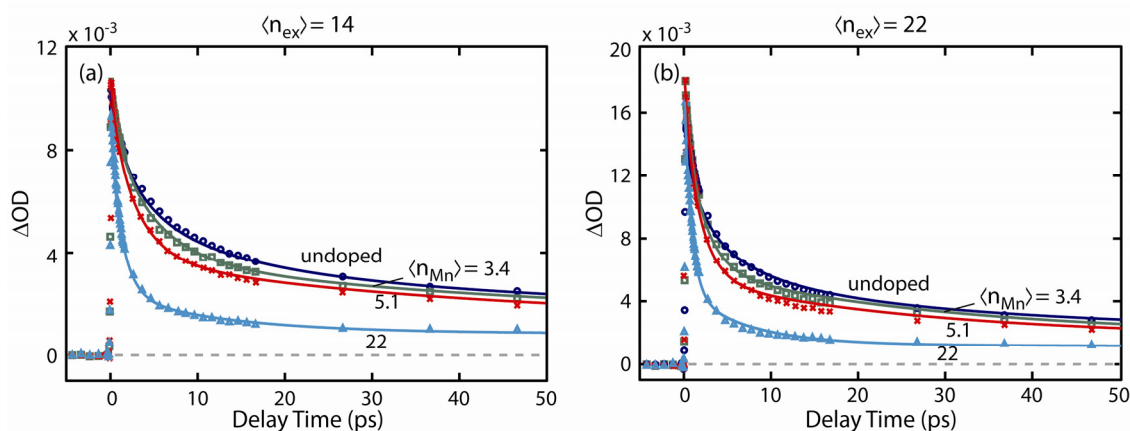


Figure 24. Transient absorption data for CdS/ZnS core/shell nanocrystals doped with various $\langle n_{Mn} \rangle$ (as indicated in the legend) measured with pump/probe wavelength 390/880 nm at $\langle n_{ex} \rangle = 14$ and 22 ((a) and (b)). The early signal decays faster as $\langle n_{Mn} \rangle$ increases, indicating the exciton to Mn^{2+} energy transfer effectively competes with Auger recombination process even at high excitation density.

4.3 Conclusions

In conclusion, exciton-dopant energy transfer time in Mn-doped CdS/ZnS core/shell nanocrystals was measured employing pump-probe transient absorption technique. Using the nanocrystals with well-defined doping radius and concentration, a quantitative energy transfer time that can be correlated with the doping structure of the nanocrystals were obtained. Energy transfer time was measured from the comparative analysis of the exciton relaxation dynamics in doped and undoped nanocrystals. For this purpose, near IR probe monitoring primarily the intraband transition of excitons was used. Employing a simple kinetic model, where the energy transfer competes with

exciton relaxation and trapping, the energy transfer time of 60 ps for a pair of exciton and Mn^{2+} ion was obtained for 5 nm Mn-doped CdS/ZnS nanocrystals with doping radius of 2.1 nm and exciton density of 1 per particle. The strategy taken in this work will be useful in future studies on the relationship between the energy transfer time and structure of the doped nanocrystals.

4.4 Experimental Section

Synthesis of nanocrystals, photoluminescence spectrum and time-dependent Mn luminescence intensity measurements are described in Chapter III.

The general method of the transient absorption measurement is described in Chapter III. Here, the pump beam centered at 390 nm was generated by doubling 60 fs, 780 nm fundamental output in a 300 μm -thick BBO (β -barium borate) crystal with average fluence of the pump beam under the probe beam area in the range of 0.9 - 24 mJ/cm^2 . White light continuum, generated in 1 mm-thick sapphire or CaF_2 crystal by focusing several μJ of 780 nm beam, was used as the probe source. Probe beam centered at 880 and 455 nm was preselected before the sample by placing a narrow slit in the beam path of the prism dispersion compensator. The time resolution of the measurement was ~ 100 fs based on instrument limited signal rise time. The fwhm (full width at half maximum) beam size of 390 nm pump and continuum probe beam was measured to be 300 μm and 30 μm respectively. The sample solution (25 mL in total volume) was circulated as a free streaming jet (400 μm thick) at a linear speed of several m/sec to avoid reexcitation of the same sample region before the complete relaxation of Mn^{2+}

ligand field excited state and potential photo-damage of the sample. The average number of the photoexcited excitons (i.e. the number of 390 nm photons absorbed) per particle at a given excitation fluence was estimated following the method in Chapter III. The concentration of the nanocrystals (21 μM) was determined from the average diameter of the nanocrystals measured from TEM and total metal ion concentration measured from elemental analysis employing ICP mass spectrometry.

CHAPTER V

DOPING LOCATION- AND SIZE- DEPENDENT ENERGY TRANSFER IN MN- DOPED CdS/ZnS NANOCRYSTALS*

5.1 Introduction

Doping of semiconductor nanocrystals is attracting significant attention as a way to introduce new optical, electronic, and magnetic properties originating from the dopant ions interacting with charge carriers of the semiconductor host in the confined space of the nanocrystals.^{1,4,74} In particular, semiconductor nanocrystals doped with transition metal ions have shown interesting luminescence and magnetic properties applicable in optoelectronics and spintronics.^{99,114-116} Due to the spatially confined nature of the nanocrystals, the interaction of the dopant ions with charge carriers responsible for many new properties of doped nanocrystals is stronger than in their bulk counterparts, leading to the enhancement of the dopant-related material properties.^{4,74} For instance, Mn phosphorescence and photoinduced ferromagnetism in Mn-doped CdS or CdSe nanocrystals, resulting from exciton-Mn energy transfer and formation of excitonic magnetic polaron, respectively, are stronger due to the greater overlap of the exciton and dopant wavefunctions than in the bulk.^{4,33,117}

*Reprinted in part with permission Chen, Hsiang-Yun; Maiti, Sourav; Son, Dong Hee, Doping Location-Dependent Energy Transfer Dynamics in Mn-Doped CdS/ZnS Nanocrystals. *ACS Nano* **2012**, 6 (1), 583-591. Copyright 2012 by the American Chemical Society.

The strength of exchange coupling between the dopant and charge carriers that dictates the rate of many interesting photophysical processes in doped semiconductor nanocrystals depends on the wavefunction overlap of exciton and dopant ions.^{91,118} Trapping of the charge carriers by the structural defect and new trap states that can potentially be introduced by doping, in addition to the preexisting trap states, also depends on the electronic coupling of ‘donor’ and ‘acceptor’ sensitive to the doping location and concentration.¹⁶ Therefore, the dynamics of photophysical processes of doped semiconductor nanocrystals, including exciton relaxation and energy transfer, will be strongly affected by the spatial location and concentration of dopant within the nanocrystals.

However, studying the dynamics of the photophysical processes in doped semiconductor nanocrystals correlated with the doping structure has been challenging partly due to the difficulties in obtaining doped nanocrystals with well-defined doping structure and the added complexity in the dynamics. In the majority of the syntheses of doped semiconductor nanocrystals, the radial doping location in the nanocrystals was either random or poorly controlled.^{58,59,119} Dynamics measured from an ensemble of such nanocrystals will be highly heterogeneous and information on the doping location dependence will be buried under the structural heterogeneity. So far, only a small number of studies have addressed the properties of doped nanocrystals correlated with doping location, mostly on the dopant luminescence and its quantum yield in Mn-doped II-VI semiconductor nanocrystals.^{70,83}

In this study, we investigated the dynamics of exciton relaxation and exciton-Mn energy transfer in Mn-doped CdS/ZnS core/shell nanocrystals correlated with the radial doping location and doping concentration *via* pump-probe transient absorption measurements. For this purpose, we employed layer-by-layer synthesis method to prepare the spherical doped nanocrystals with the largely removed heterogeneity in the radial doping location.⁶⁹ The exciton dynamics in Mn-doped nanocrystals reflects the competition among many processes such as exciton recombination, charge carrier trapping and exciton-Mn energy transfer processes.^{46,50,51,120} From the measurements of transient absorption at the band-edge and near infrared regions, structurally correlated rates of exciton-Mn energy transfer and competing charge carrier trapping process were obtained. The rate of exciton-Mn energy transfer was strongly dependent on doping location, showing ~6 fold increase with 1.2 nm decrease in doping radius in ZnS shell in this study. Hole trapping, occurring on 50 - 90 ps time scale, was identified as the major nonradiative pathway competing with exciton-Mn energy transfer. In addition, the quantum yield of radiative relaxation of Mn excited state also exhibited dependence on the doping location and concentration, which can become close to unity. Information on the structurally resolved dynamics of various photophysical processes in Mn-doped nanocrystals in this study will provide a valuable insight into the structural control of the properties of doped semiconductor nanocrystals.

5.2 Results and Discussion

5.2.1 Doping Location Dependence of Exciton-Mn Energy Transfer

Two different pairs of undoped and Mn-doped spherical core/shell nanocrystals were synthesized in this study using CdS/ZnS and CdSe/ZnS core/shell structures as the host nanocrystals. Mn-doped CdS/ZnS nanocrystals were used to investigate the doping radius- and concentration-dependent exciton dynamics in the presence of exciton-Mn energy transfer process. Mn-doped CdSe/ZnS nanocrystals were used to examine the potential role of Mn^{2+} ions as the charge carrier trap since exciton-Mn energy transfer pathway can be blocked by decreasing the bandgap of the host nanocrystals.^{6,91} Both doped and undoped core/shell nanocrystals were prepared *via* layer-by-layer coating of the shell on the premade core nanocrystals similar to our earlier work.⁹⁵

Figure 25 displays the representative transmission electron micrograph (TEM) and schematic diagram of the doping structure of the Mn-doped CdS/ZnS core/shell nanocrystals used in this study. The nanocrystals have the average core and total diameter of 3.6 and 7.2 nm, respectively. Mn^{2+} ions are doped at three different radial locations in ZnS shell with average distance d of 0, 0.6, and 1.2 nm from the interface of core and shell. A detailed discussion on the determination of the average doping location is made in Section 3.4. For each doping location d (labeled as **a**, **b**, and **c**), nanocrystals in three different ranges of doping concentration (labeled as **1**, **2**, and **3**) were prepared as summarized in Table 3. The three different doping concentration groups have average doping concentration of $\langle n_{\text{Mn}} \rangle = \sim 6$, ~ 12 , and ~ 22 ions per nanocrystal on average. The diameters of the core and core/shell nanocrystals were obtained from TEM. The average

Mn doping concentration was measured from the elemental analysis employing inductively coupled plasma mass spectrometry and the particle size determined from TEM.

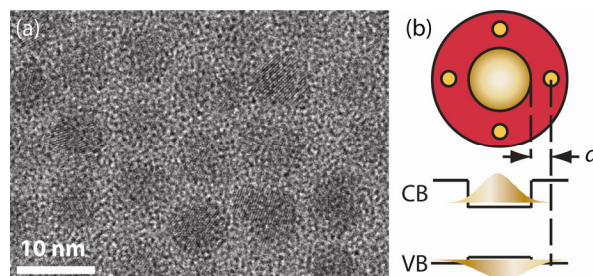


Figure 25. (a) TEM of typical Mn-doped CdS/ZnS nanocrystals. (b) Schematic diagram of the structure of the Mn-doped CdS/ZnS nanocrystals and exciton wavefunction distribution. d is the radial doping location of Mn^{2+} ions (yellow dots). VB and CB are valence and conduction band.

Figure 26 shows the absorption and photoluminescence spectra of undoped and three Mn-doped CdS/ZnS nanocrystals with $\langle n_{\text{Mn}} \rangle = \sim 6$ at various radial doping locations. Both undoped and Mn-doped nanocrystals exhibit very similar absorption spectra, supporting that the core size and shell thickness are nearly identical in all the samples. Undoped nanocrystals show exciton fluorescence peaked at 433 nm. In Mn-doped nanocrystals, exciton fluorescence was nearly quenched while the sensitized Mn phosphorescence appeared at ~ 600 nm arising from the dipole-forbidden ligand field transition (${}^4\text{T}_1 \rightarrow {}^6\text{A}_1$) following exciton-Mn energy transfer.^{4,106} Mn phosphorescence luminescence blue shifts as Mn^{2+} ions are doped closer to the surface of the nanocrystals. This was previously explained by the difference in the local pressure at different radial doping location resulting from the lattice mismatch at the core/shell interface.⁸³ The

luminescence quantum yields of both exciton (Φ_{ex}) and Mn (Φ_{Mn}) and lifetimes of Mn luminescence (τ_{Mn}) from Mn-doped nanocrystals are shown in Table 3.

Table 3. Exciton (Φ_{ex}) and Mn (Φ_{Mn}) Luminescence Quantum Yield and Mn Luminescence Lifetime (τ_{Mn}) of Doped CdS/ZnS Nanocrystals of Varying Doping Location (d) and Concentration ($\langle n_{\text{Mn}} \rangle$).

| Sample | d (nm) | $\langle n_{\text{Mn}} \rangle$ | Φ_{ex} | Φ_{Mn} | τ_{Mn} (ms) | ϕ_{Mn}^a | $\tau_{\text{Mn}}/\tau_{\text{Mn,r}}^b$ |
|-----------|----------|---------------------------------|--------------------|--------------------|-------------------------|----------------------|---|
| undoped | | 0 | 0.35 | - | - | - | - |
| a1 | 0 | 5.3 | 0.02 | 0.70 | 5.2 | 0.86 | 0.83 |
| a2 | 0 | 13 | 0.01 | 0.71 | 4.6 | 0.80 | 0.73 |
| a3 | 0 | 20 | 0.00 | 0.50 | 3.3 | 0.56 | 0.52 |
| b1 | 0.6 | 6.1 | 0.01 | 0.76 | 6.0 | 0.95 | 0.95 |
| b2 | 0.6 | 11 | 0.01 | 0.75 | 5.8 | 0.87 | 0.92 |
| b3 | 0.6 | 24 | 0.00 | 0.71 | 4.0 | 0.79 | 0.63 |
| c1 | 1.2 | 6.4 | 0.04 | 0.41 | 5.1 | 0.72 | 0.81 |
| c2 | 1.2 | 13 | 0.02 | 0.41 | 4.8 | 0.68 | 0.76 |
| c3 | 1.2 | 21 | 0.01 | 0.46 | 3.3 | 0.56 | 0.52 |

^a ϕ_{Mn} is the radiative relaxation quantum yield of Mn obtained from Φ_{Mn} and relative efficiency of energy transfer (f_{ET}).

^b The ratio between the measured τ_{Mn} and the hypothetical radiative lifetime of $\tau_{\text{Mn,r}} = 6.3$ ms. See the text.

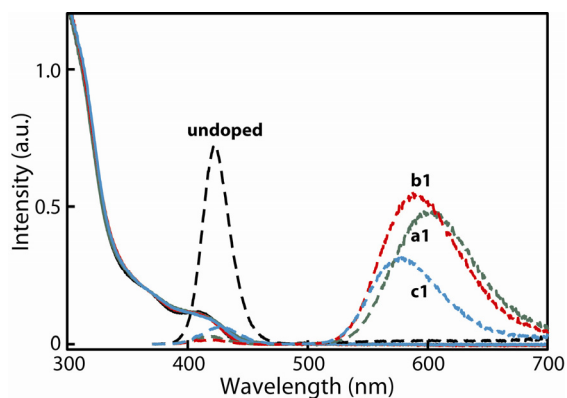


Figure 26. Absorption (solid) and photoluminescence (dashed) spectra of undoped and Mn-doped CdS/ZnS nanocrystals with different doping location (d) with $\langle n_{\text{Mn}} \rangle = \sim 6$. **a1**, **b1**, **c1** are for $d = 0, 0.6, 1.2$ nm, respectively.

To investigate the doping location-dependent exciton relaxation and energy transfer dynamics in undoped and Mn-doped CdS/ZnS nanocrystals, pump-probe transfer dynamics in undoped and Mn-doped CdS/ZnS nanocrystals, pump-probe transient absorption (ΔOD) measurement was made on colloidal solutions of the nanocrystals. The bleach recovery at 420 nm and the decay of induced absorption at 880 nm were measured as shown in a - c and d - f of Figure 27, respectively. Each panel compares the ΔOD data of the nanocrystal samples with different doping location but in the same doping concentration group. At the probe wavelength of 420 nm, corresponding to the interband transition at the peak of the first excitonic absorption, ΔOD data reflects primarily the electron dynamics. In undoped nanocrystals, it represents the combined dynamics of the radiative recombination of exciton and removal of the electron population from the conduction band by electron trapping as depicted in Figure 28.^{46,48,50-52} In Mn-doped nanocrystals, the bleach recovery has an additional contribution from exciton-Mn energy transfer. However, the hole dynamics, such as hole trapping, has little spectroscopic signature at this wavelength in both undoped and doped

nanocrystals.^{50,51} In some cases, dopant can also function as the electron or hole trap. However, substitutionally doped Mn^{2+} ions in CdS/ZnS host function as the energy acceptor rather than charge carrier acceptor because the charge transfer between Mn^{2+} ion and valence or conduction band is energetically more expensive than bandgap transition.¹¹⁵

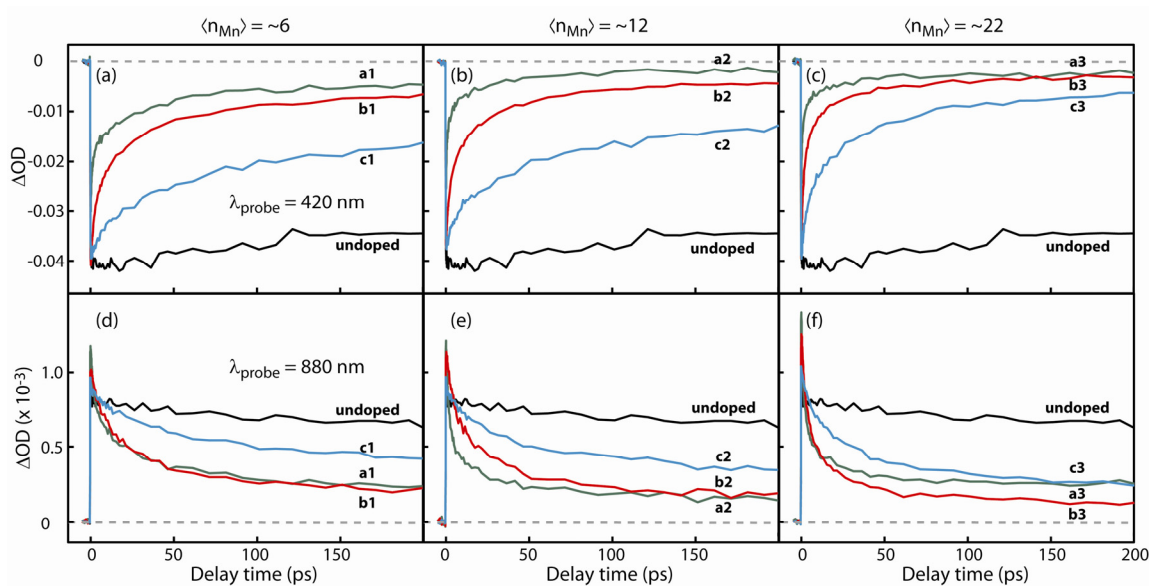


Figure 27. (a) - (c) Bleach recovery probed at 420 nm and (d) - (f) induced absorption probed at 880 nm of undoped and Mn-doped CdS/ZnS nanocrystals of varying doping locations and densities. Doping location $d = 0, 0.6, 1.2 \text{ nm}$ are labeled as **a**, **b**, **c**, respectively. Each panel compares the samples belonging to the same doping concentration group as noted on top of each column.

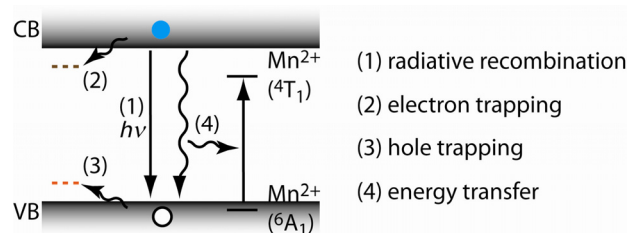


Figure 28. Photophysical processes following the excitation of exciton in Mn-doped semiconductor nanocrystals. CB and VB are conduction and valence band. Dashed lines within the gap represent trap states.

The induced absorption probed at 880 nm exhibits the dynamics that is nearly a mirror image of the bleach recovery measured at 420 nm, although the amplitude is ~ 50 times smaller. The similarity of the dynamics represented in the data at both probe wavelengths is clearly seen in Figure 29, where the normalized $|\Delta OD|$ are compared. In our previous study, we ascribed the induced absorption at 880 nm observed in a similar Mn-doped nanocrystal sample to the intraband absorption of the electrons mixed with absorption from the trapped exciton, although its nature (*i.e.*, electron *vs.* hole trap) was not clearly identified.⁹⁵ Therefore, $|\Delta OD|$ data at these two probe wavelengths contain similar information on the electron dynamics at low initial exciton densities (*e.g.*, <1 exciton/particle), although they become increasingly dissimilar at higher excitation densities due to the saturation of the bleach.^{49,111,121} ΔOD data from all the Mn-doped nanocrystal samples at both probe wavelengths share the following common general features. They exhibit the dynamics occurring on two clearly separated time scales. The fast component, with a few to tens of ps dynamics, becomes faster with increasing doping concentration and smaller value of d . The slower component has ~ 1 ns time

constant and does not exhibit noticeable dependence on the doping concentration or location.

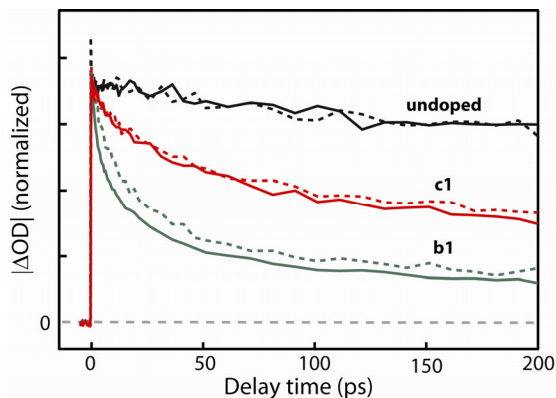


Figure 29. Comparison of the normalized $|\Delta OD|$ data probed at 420 (solid) and 880 nm (dashed).

We first discuss the bleach recovery data probed at 420 nm in Figure 27a-c. In order to extract the time scale of the dynamics, we fit the data to the sum of three exponential functions, $-\sum r_i \cdot \exp(-t/\tau_i)$. The data with an extended time window (750 ps) and the overlaid fit result are also provided in Figure 30. The fitting parameters are summarized in Table 4, where r_i is the relative amplitude of the exponential function with time constant τ_i . The fast component in the dynamics was fit with two exponential functions with time constants τ_1 and τ_2 . The slow component was fit with a fixed single exponential time constant of 1 ns. The fast component represented by the average time constant $\tau_{\text{avg}} = (r_1\tau_1 + r_2\tau_2)/(r_1 + r_2)$ can be assigned to exciton-Mn energy transfer that depletes both the electron and hole population. A single exponential function did not fit the fast component very well, especially for the doped nanocrystals with $d = 0$ nm. This

is probably due to the remaining distribution of the actual doping radius, since the core is not a perfect sphere. Statistical distribution of the doping concentration may also have contributed to the departure from the single exponential kinetics. The slow component, exhibiting essentially the same dynamics as that of undoped nanocrystals, can be interpreted in different ways. One interpretation is the presence of undoped nanocrystals within the ensemble of nanocrystals, resulting in the heterogeneous kinetics, similar to the observation made in quantum dot-dye Förster resonance energy transfer (FRET) pairs with a low surface density of dyes.⁵² However, we ruled out this possibility for the following reasons. Firstly, the fraction of undoped nanocrystals in the ensemble of nanocrystals should be <1% in all of our samples, if the doping concentration follows Poisson statistics. The small remaining exciton fluorescence results from the competition between radiative exciton relaxation and other processes not from the undoped nanocrystals.

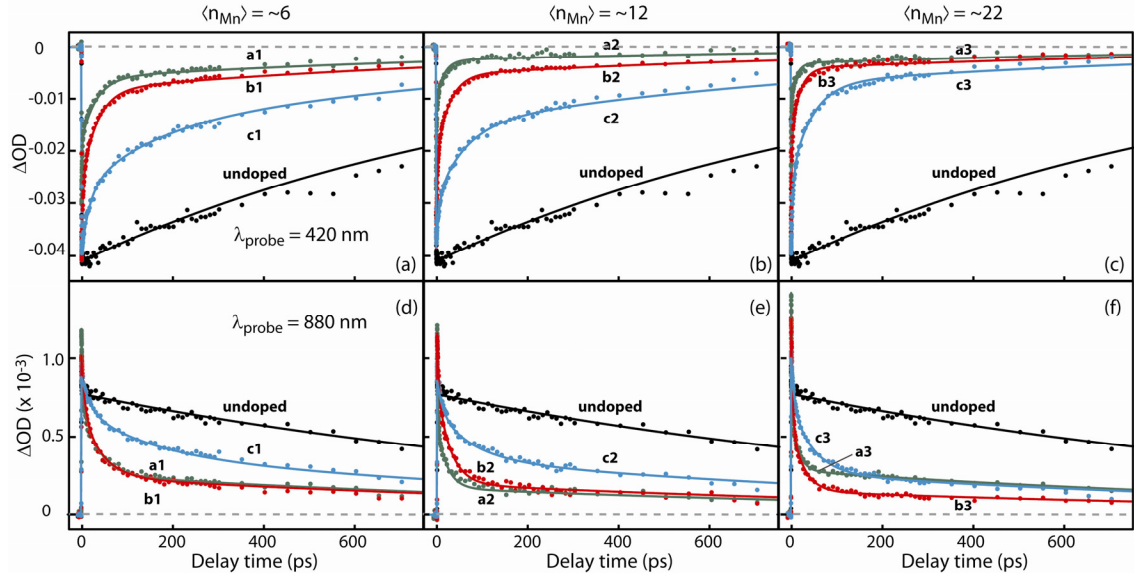


Figure 30. Comparison of transient absorption data (dots) and the fits (lines) to time window of 750 ps. (a)-(c) Bleach recovery probed at 420 nm and (d)-(f) induced absorption probed at 880 nm of undoped and Mn-doped CdS/ZnS nanocrystals of varying doping locations and densities. Doping location $d = 0, 0.6, 1.2$ nm are labeled as **a, b, c**, respectively. Each panel compares the samples belonging to the same doping concentration group as noted on top of each column.

Table 4. Multi-Exponential Fitting Parameters of ΔOD Data Probed at 420 nm to $-\sum r_i \cdot \exp(-t/\tau_i)$.

| Sample | r_1 | r_2 | r_3^a | τ_1 (ps) | τ_2 (ps) | τ_{avg} (ps) ^b | τ_{tr} (ps) ^c |
|-----------|-------|-------|---------|---------------|---------------|--------------------------------|-------------------------------|
| a1 | 0.44 | 0.37 | 0.18 | 0.88 | 32 | 15 | 67 |
| a2 | 0.52 | 0.37 | 0.12 | 0.63 | 16 | 7.2 | 55 |
| a3 | 0.62 | 0.27 | 0.11 | 0.56 | 12 | 3.8 | 30 |
| b1 | 0.36 | 0.44 | 0.20 | 2.5 | 33 | 19 | 77 |
| b2 | 0.44 | 0.42 | 0.14 | 2.1 | 27 | 15 | 89 |
| b3 | 0.54 | 0.36 | 0.10 | 1.3 | 18 | 8.0 | 70 |
| c1 | 0.28 | 0.29 | 0.43 | 18 | 141 | 80 | 106 |
| c2 | 0.23 | 0.38 | 0.39 | 6.6 | 63 | 42 | 64 |
| c3 | 0.38 | 0.45 | 0.17 | 3.8 | 45 | 26 | 125 |

^a r_3 is the amplitudes for τ_3 fixed at 1 ns.

^b $\tau_{avg} = (r_1 \tau_1 + r_2 \tau_2) / (r_1 + r_2)$

^c $\tau_{tr} = 1 / (f_{tr} \cdot (\tau_{tr}^{-1} + \tau_{ET}^{-1}))$

Secondly, the amplitude of the slow-recovery component (τ_3) varies largely with the doping location for a given doping concentration, indicating that the slow dynamics is not associated with undoped nanocrystals.

The alternative explanation involves the charge carrier trapping, more specifically hole trapping, which inhibits exciton-Mn energy transfer while not influencing the electron dynamics probed at the band-edge. The effect of hole trapping on the electron dynamics explains very well the observed ΔOD data probed at 420 nm as follows, although the hole trapping itself is spectroscopically silent at 420 nm. The inhibition of exciton-Mn energy transfer process by the hole trapping allows a fraction of nanocrystals to avoid the depopulation of the electron in conduction band occurring *via* exciton-Mn energy transfer. Therefore, the fraction of Mn-doped nanocrystals undergoing hole trapping will exhibit the similarly slow bleach recovery dynamics as the undoped nanocrystals unless doping introduces an additional electron trap. In this case, the relative amplitudes of the fast and slow bleach recovery represent the branching ratio between the energy transfer and hole trapping.

The inhibition of exciton-Mn energy transfer process by the charge carrier trapping can be understood from the large reduction in the wavefunction overlap between the donor and acceptor upon the trapping of the charge carrier if the exchange coupling of exciton and Mn^{2+} ion mediates the energy transfer.^{20,95,115} According to Dexter's theory of energy transfer mediated by exchange coupling, the probability of energy transfer (P) is proportional to the coulomb interaction of two charge clouds $Q'(r_1)$ and $Q(r_2)$ in the following way.⁸⁶

$$P \propto \left| \int Q'(r_1) \frac{1}{r_{12}} Q(r_2) dr_1 dr_2 \right|^2 \int F_d(E) F_a(E) dE$$

$$Q'(r_1) = \Psi_{exciton}^*(r_1) \Psi_{Mn(excited)}(r_1), Q(r_2) = \Psi_{Mn(ground)}^*(r_2) \quad (14)$$

Here, $\Psi_{exciton}$, $\Psi_{Mn(excited)}$, and $\Psi_{Mn(ground)}$ represent the wavefunctions of exciton, excited and ground states of Mn^{2+} ion, respectively. $F_d(E)$ and $F_a(E)$ are the normalized luminescence and absorption spectra of donor (exciton) and acceptor (Mn^{2+} ion). Therefore, the large reduction in $Q'(r_1)$ from the trapping of charge carriers will greatly diminish the rate of the energy transfer.

In principle, both the electron trapping and hole trapping can inhibit exciton-Mn energy transfer. We concluded that hole trapping is the major process inhibiting the energy transfer for the following reason. In undoped nanocrystals, electron trapping time should be longer than the bleach recovery time probed at the band-edge ($\sim ns$) that reflects the depopulation of electron in conduction band *via* both radiative and nonradiative pathways.⁵¹ If the electron trapping in Mn-doped nanocrystals is similar to undoped nanocrystals as indicated by the insensitivity of τ_3 on doping concentration, it will be too slow to compete with the energy transfer process that is orders of magnitude faster. Furthermore, if the electron trapping contributes significantly to the inhibition of the energy transfer, it should also be reflected in the slow component of the bleach recovery (τ_3), showing the faster recovery with the increasing electron trapping. The fact that the fixed time constant of $\tau_3=1ns$ can describe the slow recovery component in both undoped and doped nanocrystals regardless of the doping concentration argues against the participation of electron trapping in the inhibition of the energy transfer. A separate

experiment performed in Mn-doped CdSe/ZnS nanocrystals also indicates that Mn doping does not introduce an additional electron trapping at low doping densities as will be discussed later in more detail. On the other hand, hole trapping is considered to occur faster than electron trapping, as suggested by a number of earlier studies, therefore capable of inhibiting exciton-Mn energy transfer.^{46,51} Furthermore, the hole trapping that inhibits exciton-Mn energy transfer process explains the observed bleach recovery dynamics very well as discussed above.

Based on the above argument, r_1+r_2 and r_3 in Table 4 can be interpreted as the relative efficiency (or branching ratio) of exciton-Mn energy transfer (f_{ET}) and hole trapping (f_{tr}) processes, respectively. Since the time scale of the fast recovery is 1-2 orders of magnitude faster than the bleach recovery in undoped nanocrystals, we can readily assign the fast recovery component almost exclusively to exciton-Mn energy transfer provided that there is no additional electron trapping. Under this condition, the hole trapping time (τ_{tr}) can be obtained from the relative hole trapping efficiency (f_{tr}) and energy transfer time (τ_{ET}) via $f_{tr} = \tau_{tr}^{-1} / (\tau_{tr}^{-1} + \tau_{ET}^{-1})$, where τ_{avg} is taken as τ_{ET} . The average hole trapping time at each doping location is $\langle \tau_{tr} \rangle \sim 50, 80, \text{ and } 100 \text{ ps}$ for $d = 0, 0.6, \text{ and } 1.2 \text{ nm}$, respectively.

It is interesting to note the differences in the role of the hole trapping in the energy transfer in Mn-doped nanocrystals and quantum dot-dye FRET pairs. In quantum dot-dye FRET pairs, the energy transfer between quantum dot and dye molecules adsorbed on the surface is Förster type mediated by the dipole coupling of donor and acceptor. The hole-trapped excitons are believed to participate in the quantum dot-dye

energy transfer process.¹²² On the contrary, hole trapping in Mn-doped nanocrystals seems very effectively inhibiting the energy transfer. However, the energy transfer in Mn-doped CdS/ZnS nanocrystals can readily outcompete the hole trapping by an order of magnitude and can exhibit very high quantum yield of Mn luminescence (Φ_{Mn}) as shown in Table 3.

In Figure 31, the rate constant ($1/\tau_{\text{ET}}$) of the energy transfer process obtained from the exponential fitting of ΔOD data is shown for all Mn-doped nanocrystals as a function of both the doping location and concentration. Two clear trends are observed. With increasing doping concentration, $1/\tau_{\text{ET}}$ increases linearly for all the Mn-doped nanocrystals of different doping location, indicating that each Mn^{2+} ion has approximately an equal contribution as the energy acceptor at a given radial doping location. When the radial doping location is varied, the slope of the lines in Figure 31 increases rapidly as the dopant ions get closer to the center of the nanocrystals. With 1.2 nm change in the radial doping location, the rate of the energy transfer varies by 6 fold. We attempted to fit the donor-acceptor distance (R_{DA}) dependence of the energy transfer rate (k_{ET}) to Dexter energy transfer model (Eq. 15)⁸⁶ using the slopes in Figure 31, although we have a limited number of data points.

$$k_{\text{ET}} \propto \exp(-2 R_{DA} / L) \quad (15)$$

The value of L that represents the sum of van der Waals radii of donor and acceptor obtained from the fit is 1.4 nm, which is significantly smaller than the radius of CdS core (1.8 nm) and exciton Bohr radius in CdS (2.8 nm).¹²³ However, the largely different conduction (~ 1 eV) and valence (~ 0.2 eV) band offset in CdS/ZnS core/shell,

giving rise to different spatial extent of the electron and hole wavefunction, makes it less straightforward to apply Eq. 15 to describe the distance dependence of the energy transfer rate. A further study will be needed to address this issue more quantitatively.

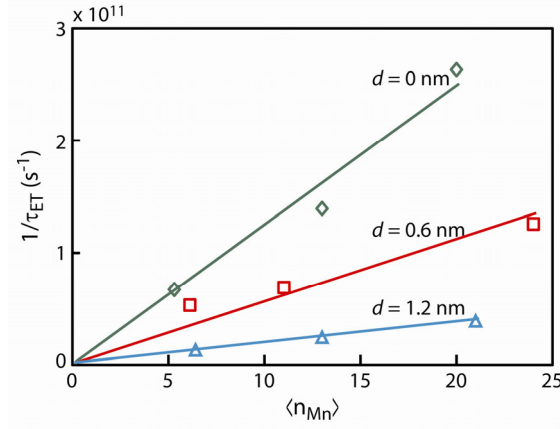


Figure 31. Doping location-dependent energy transfer rate constant ($1/\tau_{ET}$). The solid lines are trend lines assuming the energy transfer rate is linear to the average Mn doping concentration.

Since the energy transfer observed in Mn-doped CdS/ZnS nanocrystals is much faster than other radiative and nonradiative exciton relaxation pathways, the quantum yield of Mn luminescence can be quite high. In fact, all Mn-doped nanocrystals studied here exhibit higher Mn luminescence quantum yield (Φ_{Mn}) than exciton luminescence quantum yield (Φ_{ex}) of undoped nanocrystals. The large luminescence quantum yield of Mn-doped nanocrystals is also partly due to the dominating radiative relaxation of the Mn excited state. Mn luminescence quantum yield (Φ_{Mn}) can be expressed as $\Phi_{Mn} = f_{ET} \times \phi_{Mn}$, where f_{ET} and ϕ_{Mn} are the efficiency of the energy transfer and quantum yield of the radiative relaxation of Mn, respectively. ϕ_{Mn} calculated from the measured values of Φ_{Mn}

and f_{ET} is also shown in Table 3. It is interesting to note that ϕ_{Mn} decreases with decreasing τ_{Mn} and that it is as high as 0.95 in sample **b1** that has the longest Mn luminescence lifetime ($\tau_{Mn} = 6$ ms). Although the dependence of the radiative lifetime of Mn excited state ($\tau_{Mn,r}$) on the doping location and concentration is unknown in our study, we calculated $\tau_{Mn}/\tau_{Mn,r}$ and compared with ϕ_{Mn} in Table 3 assuming that $\tau_{Mn,r} = 6.3$ ms and independent of the doping location and concentration.⁷⁴ The values of $\tau_{Mn}/\tau_{Mn,r}$ are very close to the experimentally determined ϕ_{Mn} for most of the samples, suggesting that the variation of τ_{Mn} reflects largely the change of ϕ_{Mn} with varying doping location and concentration. The generally decreasing ϕ_{Mn} with increasing doping concentration observed in this study can be ascribed to the increasing Mn-Mn antiferromagnetic interaction at shorter interdopant distance that can enhance the nonradiative relaxation of Mn.^{84,108} These observations clearly indicate that the doping location and concentration not only determine the rate of exciton-Mn energy transfer but also influences the radiative quantum yield of dopant ions. These results also provide a much clearer picture of the sensitization of Mn phosphorescence in Mn-doped nanocrystals than the earlier study solely based on the quantum yield measurement.⁷⁰

Now we turn to the induced absorption data probed at 880 nm. As shown in Figure 29, the decay of the induced absorption at 880 nm exhibits very similar dynamics to the bleach recovery probed at 420 nm. The parameters from the multi-exponential fitting of the data are summarized in Table 5. The same kinetic scheme employed to interpret the bleach recovery data describes the dynamics of the data obtained at 880 nm. The fast decay component is ascribed to the depopulation of electron by the energy

transfer. The slow decay component reflects the depopulation of electron in hole-trapped nanocrystals that do not experience the energy transfer. On the other hand, the time scales of the fast component (τ_{avg}) in 880 nm data are somewhat longer and the relative amplitudes of the slow component (r_3) are larger than in 420 nm data. These small differences may partially be due to the potentially different effect of the hole trapping on the absorption cross sections of the interband and electron intraband transitions in Mn-doped nanocrystals. Besides these differences, the induced absorption probed at 880 nm essentially carries the same information as the bleach recovery data in our study. However, it is worth to mention that the induced absorption probed at near infrared region can be used to study the exciton dynamics at relatively high exciton densities, where the bleach recovery at the band-edge cannot access. This is because the amplitude of the induced absorption scales roughly linearly with the initial photoexcited exciton densities, whereas the bleach recovery rapidly saturates.⁹⁵

To examine whether doping of Mn introduces an additional electron trap, we compared the bleach recovery data at the band-edge in undoped and Mn-doped CdSe/ZnS nanocrystals that do not exhibit exciton-Mn energy transfer. The diameters of CdSe core and CdSe/ZnS core/shell are 5.2 and 6.1 nm, respectively. In this host nanocrystal, the energy transfer process is blocked since the bandgap of the host ($\lambda = 590$ nm) is smaller than the energy of accepting ligand field transition on Mn^{2+} ions.^{6,111} According to the excitation spectra of Mn-doped ZnS nanocrystals studied earlier, the lowest ligand field transition (${}^6\text{A}_1 \rightarrow {}^4\text{T}_1$) was centered around 520 nm, while luminescence (${}^4\text{T}_1 \rightarrow {}^6\text{A}_1$) occurred at 590 nm. The large Stokes shift was ascribed to the

strong coupling of the ligand field transition to LO phonon mode of the host matrix with Huang-Rhys factor of ~ 3 , which also accounts for the broad width of Mn luminescence.¹²⁴

Table 5. Multi-Exponential Fitting Parameters of ΔOD Data Probed at 880 nm to $\Sigma r_i \exp(-t/\tau_i)$.

| Sample | r_1 | r_2 | r_3^a | τ_1 (ps) | τ_2 (ps) | τ_{avg} (ps) ^b |
|-----------|-------|-------|---------|---------------|---------------|--------------------------------|
| a1 | 0.37 | 0.41 | 0.22 | 2.4 | 35 | 20 |
| a2 | 0.51 | 0.34 | 0.15 | 1.6 | 21 | 9.4 |
| a3 | 0.52 | 0.28 | 0.20 | 1.3 | 15 | 6.0 |
| b1 | 0.32 | 0.44 | 0.24 | 6.8 | 42 | 27 |
| b2 | 0.30 | 0.53 | 0.17 | 3.0 | 29 | 20 |
| b3 | 0.53 | 0.35 | 0.12 | 3.0 | 27 | 12 |
| c1 | 0.23 | 0.31 | 0.46 | 20 | 148 | 92 |
| c2 | 0.23 | 0.35 | 0.42 | 13 | 79 | 53 |
| c3 | 0.28 | 0.45 | 0.27 | 6.4 | 48 | 32 |

^a r_3 is the amplitudes for τ_3 fixed at 1.3 ns.

^b $\tau_{avg} = (r_1 \tau_1 + r_2 \tau_2) / (r_1 + r_2)$

Figure 32 shows the bleach recovery data of undoped and Mn-doped CdSe/ZnS nanocrystals with $\langle n_{Mn} \rangle = 2.3$ and 40 at $d = 0$ nm pumped at 395 nm and probed at 590 nm. The bleach recovery dynamics of the undoped and Mn-doped nanocrystals with $\langle n_{Mn} \rangle = 2.3$ are virtually identical, indicating that doping Mn^{2+} ions does not introduce an additional electron trapping at a low doping concentration. In addition, the similar photoluminescence quantum yield of undoped ($\Phi_{ex} = 0.22$) and Mn-doped ($\Phi_{ex} = 0.21$) CdSe/ZnS nanocrystals also indicates that Mn doping at low densities do not introduce an additional charge carrier trapping that leads to the nonradiative relaxation of excitons.

While CdSe was used as the core instead of CdS to prevent the energy transfer, the evidence for the absence of an additional electron trapping in CdSe is consistent with the insensitivity of τ_3 to Mn doping in CdS/ZnS host that is also indicative of the absence of the additional electron trapping. However, at much higher doping concentrations, *e.g.*, $\langle n_{\text{Mn}} \rangle = 40$, the bleach signal begins to show faster recovery and the quantum yield of exciton luminescence decreases. This observation suggests that significantly more additional charge carrier traps can be created including electron traps at very high doping concentrations, perhaps due to the creation of a structural defect.

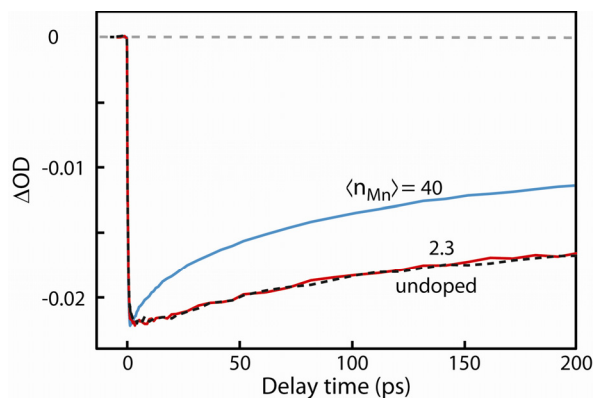


Figure 32. Bleach recovery of undoped (dashed) and Mn-doped (solid) CdSe/ZnS nanocrystals at 590 nm.

5.2.2 Nanocrystal Size Dependence of Exciton-Mn Energy Transfer

In this section, we discuss the correlation between exciton-Mn energy transfer rate and the size of Mn-doped nanocrystals for a given radial doping location. With increasing size of the host nanocrystals, the spatial extent of exciton wavefunction will also increase if exciton is in the spatially confined regime. Therefore, the change in the

size of the host nanocrystals can vary the wavefunction overlap between exciton and dopant ions, which can modify the energy transfer rate.

The effect of varying the particle size on the exciton-Mn energy transfer rate was examined in CdS/ZnS core/shell nanocrystals, where the effective radius of CdS core is varied at a fixed radial doping location and doping concentration. Figure 33a shows TEM images of the two Mn-doped nanocrystals having different core sizes labelled as ‘small’ and ‘large’. The thickness of the outer ZnS shell was maintained the same at 0.7 nm. The insets in the figures are the pictorial representation of the nanocrystal structures. Figure 33b compares the UV-Vis absorption spectra of the both nanocrystals, where the red-shift of the exciton absorption peak is observed with increasing core radius from 1.8 to 2.5 nm. For both nanocrystals, Mn ions were doped at 1.8 nm from the center of the nanocrystal.

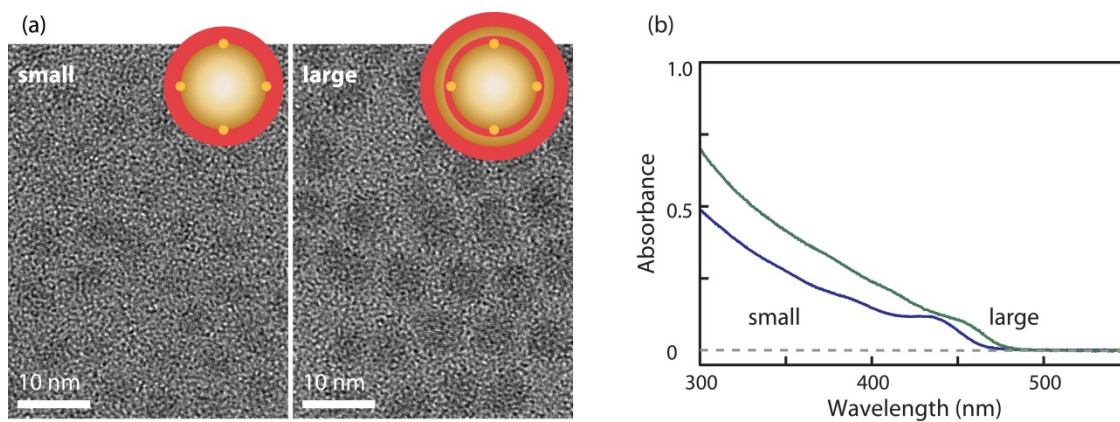


Figure 33. (a) TEM images of the Mn-doped CdS/ZnS nanocrystals with different core radius, 1.8 and 2.5 nm for small and large nanocrystals. Doping radii and concentrations are identical in the two nanocrystals. (b) UV-Vis absorption spectra of the two Mn-doped nanocrystals in (a).

Figure 34a and b compare the dynamics of the band-edge bleach recovery for the pair of undoped and doped nanocrystals of the two different core sizes shown in Figure 33. While both pairs of the nanocrystal samples were excited at the same pump wavelength of 395 nm, the bleach recovery was probed at 420 and 455 nm for the small and large nanocrystals respectively to match the size-dependent band-edge absorption. Both the small and large nanocrystals exhibit the appearance of the fast-recovery component in the bleach signal upon doping. The fast-recovery component on the time scale of <10 ps represents the energy transfer for both samples. The difference between the energy transfer dynamics in small and large nanocrystals can be more clearly seen in $\Delta\Delta\text{OD}$ data shown in Figure 34c, where the fast-recovery component in the bleach recovery signal is isolated by subtracting the slow-recovery component. In Figure 34c, small nanocrystals exhibit the faster dynamics in $\Delta\Delta\text{OD}$ data, indicating the faster energy transfer rate. The energy transfer is faster in the small nanocrystals since the amplitude of the exciton wavefunction at the dopant site is larger due to the more confined nature of the wavefunction. This observation also confirms the importance of the confinement of exciton and dopant wavefunctions within the same volume of the nanocrystals in enhancing the efficiency of the photophysical processes mediated by the exciton-dopant electronic coupling.

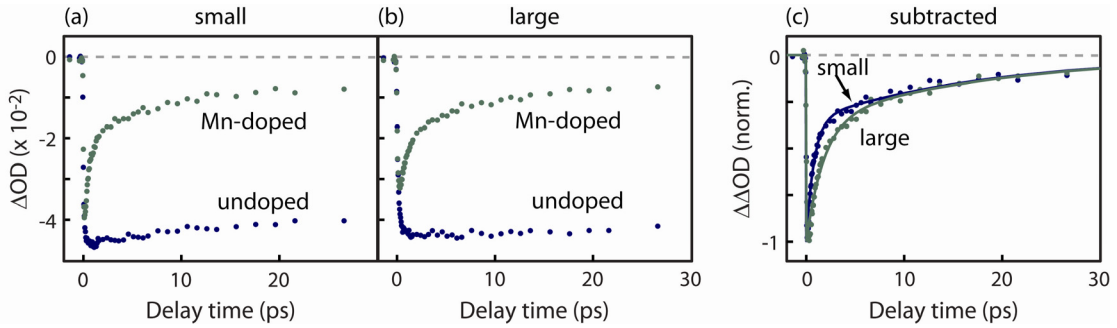


Figure 34. (a), (b) Comparison of the dynamics of band-edge bleach recovery in undoped and doped nanocrystals of small and large core sizes. (c) Normalized $\Delta\Delta\text{OD}$ data obtained by subtracting the slow-recovery component ($\sim\text{ns}$) from the data of Mn-doped nanocrystals.

5.3 Conclusions

In conclusion, doping location-dependent dynamics of exciton relaxation and energy transfer in Mn-doped CdS/ZnS nanocrystals are investigated *via* transient absorption measurements. By using the doping location- and concentration-controlled nanocrystals that removed a major structural heterogeneity, previously unavailable information on the dynamics of energy transfer and competing hole trapping is obtained. The rate of exciton-Mn energy transfer exhibited a strong dependence on the doping radius for a given doping concentration and occurred on the time scales of a few to tens of ps within the range of the doping concentration of this study. In the competition between exciton-Mn energy transfer and charge carrier trapping that inhibits the energy transfer, hole trapping was identified as the major process competing with exciton-Mn energy transfer. Due to the fast energy transfer that efficiently competes with nonradiative relaxation pathways, Mn-doped nanocrystals exhibited much higher luminescence quantum yield than undoped nanocrystals. Knowledge on the structurally

resolved dynamics of various photophysical processes in Mn-doped nanocrystals obtained in this study will provide a valuable insight into the structural control of the properties of doped semiconductor nanocrystals.

5.4 Experimental Section

Synthesis of nanocrystals, quantum yield measurement, and time-dependent Mn luminescence intensity measurement are described in Chapter III.

The general description of the transient absorption measurement is described in Chapter III. Detailed experimental condition for this set of experiment is as the following. Pump pulse at 395 nm was generated by the frequency doubling of 790 nm output from a Ti:sapphire laser in a β -barium borate crystal at 3 kHz repetition rate. The pulse width and fwhm beam diameter of the pump beam were 70 fs and 300 μm , respectively with $\langle n_{\text{ex}} \rangle$ than 0.5. White light continuum generated in 1 mm-thick CaF_2 and sapphire window by focusing 790 nm beam was used as the probe light (fwhm beam diameter $\sim 30 \mu\text{m}$) at band-edge (420 nm) and near infrared (880 nm) regions, respectively. The hexane solutions of the sample nanocrystals were circulated in a 1 mm-thick quartz liquid cell at the linear flow rate of $\sim 1 \text{ m/s}$ to avoid potential photo-damage and reexcitation of the same sample area. The nanocrystal concentrations of all the samples were kept the same at $\sim 6.4 \mu\text{M}$.

CHAPTER VI

HOT ELECTRONS FROM CONSECUTIVE EXCITON-Mn ENERGY TRANSFER IN Mn-DOPED SEMICONDUCTOR NANOCRYSTALS*

6.1 Introduction

Generation of hot electrons in metallic or semiconducting materials and hot electron-induced chemistry on their surfaces have been actively investigated for decades. For instance, optically excited hot electrons with excess energy above Fermi level of metals demonstrated its capability to transfer part of electron energy to the adsorbate molecules and excite their internal modes initiating various surface chemistry.¹²⁵⁻¹³⁰ In semiconductors, hot electrons excited above the conduction band edge have been shown to be beneficial in catalysis and photovoltaic applications via fast interfacial charge transfer that can effectively compete with intraband relaxation.¹³¹⁻¹³³

Recently, a number of groups reported efficient interfacial charge transfer of optically excited hot electrons in semiconductor nanocrystals,¹³⁴⁻¹³⁶ demonstrating the potential of harvesting hot electrons in nanocrystals that are widely employed in catalysis and photovoltaic applications. Hot electrons with larger excess energy will generally experience a lower energy barrier for interfacial charge transfer and their

*Reprinted in part with permission from Chen, Hsiang-Yun; Chen, Tai-Yen; Berdugo, Erick; Park, Yerok; Lovering, Kaitlin; Son, Dong Hee. Hot Electrons from Consecutive Exciton–Mn Energy Transfer in Mn-Doped Semiconductor Nanocrystals. *J. Phys. Chem. C* **2011**, *115* (23), 11407-11412. Copyright 2011 by the American Chemical Society.

wavefunctions can reach further away from the nanocrystals, making them potentially useful for photocatalytic and photovoltaic applications.

Hot electrons in semiconductor nanocrystals can be excited via optical excitation in a number of different ways. The simplest way is the above-bandgap excitation with sufficient excess energy that can excite the electrons high in conduction band. Hot electrons with higher excess energy generally requires excitation with the higher-energy photons in the UV region, which is increasingly less convenient to work with. The lower-energy photons can also excite hot electrons with large excess energy via multiphoton excitation.¹³⁷⁻¹³⁹ However, multiphoton excitation is usually much less efficient than single photon excitation and requires high excitation intensity.

In this study, we investigated the generation of hot electrons with large excess energy in Mn-doped semiconductor nanocrystals that occurs via two consecutive exciton-Mn energy transfer process taking advantage of the fast exciton-Mn energy transfer and long lifetime of the intermediate acceptor state. In Mn-doped semiconductor nanocrystals such as Mn-doped CdS or ZnS, the energy of photoexcited excitons can be transferred to the excited ligand field state of Mn^{2+} ions. Typically, exciton-Mn energy transfer depletes the population of exciton and creates the locally excited ligand field state of Mn^{2+} ion (${}^4\text{T}_1$) that has a lifetime of $\sim 10^{-3}$ s due to the dipole-forbidden nature of the transition involved.^{4,106}

In principle, exciton-Mn energy transfer to the same Mn^{2+} ion can occur twice consecutively promoting Mn^{2+} ion to the higher-energy state if the second energy transfer occurs before the relaxation of ${}^4\text{T}_1$ state of Mn^{2+} ion. If such consecutive energy

transfer occurs, the excited d-electron on Mn^{2+} ion at the terminal state is energetically located significantly above the conduction band edge of the semiconductor host. In this case, the excited state of Mn^{2+} ion after two consecutive energy transfer can be considered as Mn^{2+} ionized into conduction band of the semiconductor host creating a delocalized hot electron and a hole localized near Mn^{2+} ion.^{140,141} Therefore, the overall effect of the two consecutive exciton-Mn energy transfer can be viewed as an 'upconversion' of the energy of two excitons into one composed of a hot electron and a localized hole. The hot electron and localized hole pair eventually recombines and relaxes back to ground state.

Here, we present experimental evidences showing that two consecutive exciton-Mn energy transfer occur efficiently generating hot electrons in Mn-doped colloidal CdS/ZnS core/shell nanocrystals. The key evidence comes from the measurement of the luminescence intensity from ${}^4\text{T}_1$ state of Mn^{2+} ion serving as the intermediate acceptor state at varying excitation density under one- or two-pulse excitation conditions. We also show that Mn-doped nanocrystals exhibit a higher photocatalytic reducing capability of methylene blue than undoped nanocrystals when the excitation rate is sufficiently fast to have consecutive exciton-Mn energy transfer even under *cw* excitation condition.

6.2 Results and Discussion

Figure 35 shows the UV-Vis absorption and luminescence spectra of both undoped and Mn-doped nanocrystals used in this study. Luminescence spectra of both

nanocrystals were obtained with 370 nm excitation. The exciton and Mn luminescence in undoped and Mn-doped nanocrystals occur at 440 nm and 625 nm respectively.

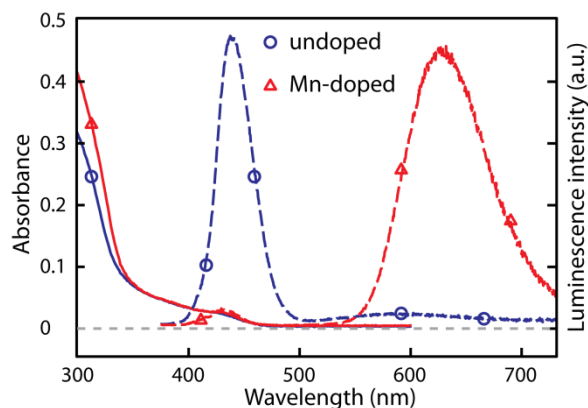


Figure 35. Absorption (solid) and luminescence (dashed) spectra of undoped and Mn-doped CdS/ZnS nanocrystals. Excitation wavelength is 370 nm.

In Mn-doped CdS/ZnS nanocrystals, Mn luminescence arises from the radiative relaxation of 4T_1 ligand field state of Mn^{2+} ions populated by exciton-Mn energy transfer (ET1) to the ground 6A_1 state. If an additional exciton-Mn energy transfer (ET2) occurs to the same Mn^{2+} ion before the relaxation of 4T_1 state, 4T_1 state can be further excited to the conduction band level of the host leading to the ionization of Mn^{2+} to the conduction band as depicted in Figure 36a. Since the energy levels of Mn^{2+} d electrons are close to the valence band edge of CdS,^{142,143} the two consecutive energy transfer (ET1 and ET2) to the same Mn^{2+} ion can create hot electrons with a large excess energy in conduction band. The hole initially on Mn^{3+} will likely to be shared locally by the sulfur atoms nearby. Therefore, the resulting state from the two consecutive exciton-Mn energy transfer can be considered as a hot exciton composed of a hot electron and a localized

hole near Mn^{2+} ion. One might view this process as the 'upconversion' of the energy of two excitons into a more energetic exciton via two energy transfer processes (eq. 16) In this scheme, while the intermediate ${}^4\text{T}_1$ state is emissive the terminal state decays nonradiatively rather than decaying back to ${}^4\text{T}_1$ state as will be discussed more in detail later.

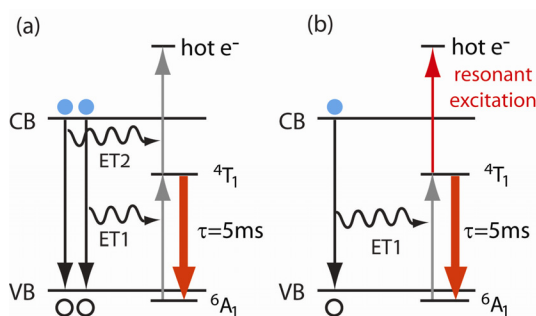
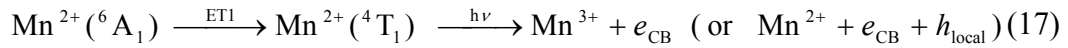


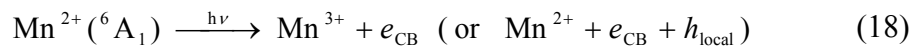
Figure 36. Possible pathways for hot electron excitation in Mn-doped CdS/ZnS nanocrystals (a) Hot electron excitation via two consecutive exciton-Mn energy transfer process in Mn-doped CdS/ZnS semiconductor nanocrystals. (b) Hot electron excitation via exciton-Mn energy transfer followed by a direct resonant excitation of ${}^4\text{T}_1$ ligand field state of Mn^{2+} ion. VB and CB are valence and conduction band respectively. Thick downward arrows in orange color indicate Mn luminescence. The lifetime of ${}^4\text{T}_1$ state is 5 ms.

The confirmation of the occurrence of consecutive energy transfer from the spectroscopic detection of hot electrons is not straightforward in the steady state or time-resolved absorption measurements. This is because hot electrons in the conduction band do not have a sufficiently distinct spectroscopic signature from that of lower-energy electrons excited by the initial photoexcitation. However, the decrease of Mn luminescence from the depletion of the emitting ${}^4\text{T}_1$ state can be used as a readily

measurable indicator of the occurrence of two consecutive energy transfer under the experimental condition that rules out other pathways to deplete 4T_1 state. In fact, a decrease of Mn luminescence from the direct resonant excitation of 4T_1 state to conduction band following an exciton-Mn energy transfer has been observed in Mn-doped ZnSe nanocrystals by Irvine et al. under two-color *cw* excitation condition as depicted in Figure 36b.¹⁴⁰ (eq. 1)



In their study, 440 nm beam was used for the excitation of exciton and 676 nm beam was used to excite 4T_1 state to conduction band. However, since the absorption cross section of 4T_1 state was several orders of magnitude smaller than that of exciton, 676 nm beam was several orders of magnitude more intense than 440 nm beam to excite 4T_1 state to conduction band resonantly. The decrease of Mn luminescence intensity upon excitation from 4T_1 state to conduction band is considered to be due to the relatively fast nonradiative relaxation pathway compared to the relaxation of the electron through the manifold of ligand field states of Mn^{2+} ion. The nonradiative decay of the electrons ionized from Mn^{2+} ions to conduction band was also reported in Mn-doped ZnO nanocrystals, where the direct charge transfer excitation from 6A_1 state to conduction band can occur with sub-bandgap excitation due to the midgap location of 6A_1 state.¹⁴⁴ (eq. 18) However, such direct charge transfer excitation does not occur in Mn-doped CdS/ZnS nanocrystals.



In our study, we observed the decrease of Mn luminescence intensity in Mn-doped CdS/ZnS nanocrystals as the excitation density increased under pulsed excitation condition, which can only be explained by the excitation of hot electrons via two consecutive energy transfer. We used pulsed excitation at 395 nm (60 fs pulse width) in the fluence range of 0 - 4.6 mJ/cm² per pulse. Under this condition, the probability of resonant excitation of ⁴T₁ state to conduction band is negligible, since the absorption cross section of ⁴T₁ state at 395 nm is estimated to be 3 - 4 orders of magnitude smaller than that of exciton ($\sigma_{\text{ex}} = 2.2 \times 10^{-15} \text{ cm}^2$) in our Mn-doped nanocrystals.^{141,145} Therefore, the process described in eq. 17 is highly unlikely under our experimental condition. In addition, the excitation pulse width (60 fs) much shorter than the exciton-Mn energy transfer time ($\sim 10 \text{ ps}$)⁹⁵ and the slow rate (50 Hz) of the excitation further preclude the possibility of the excitation of ⁴T₁ state to conduction band following ET1. Furthermore, the lattice heating from the photoexcitation is sufficiently small and short-lived, not affecting the luminescence lifetime and quantum yield of ⁴T₁ state as will be discussed further in detail below. This indicates that the decrease of Mn luminescence reflects the actual depletion of the emitting ⁴T₁ state population.

Figure 37 compares the excitation density-dependent luminescence intensities of Mn-doped and undoped CdS/ZnS nanocrystals in the excitation density of 0 - 20 photons/particle. The two curves are plotted with the initial slopes in the linear regime at low excitation densities matched in order to show the difference at higher excitation densities more clearly. The average excitation density, $\langle n_{\text{ex}} \rangle$, was estimated from $\langle n_{\text{ex}} \rangle = f \cdot \sigma$, where f is the excitation fluence and σ is the absorption cross section of the

nanocrystal assuming that σ is not sensitive to the excitation intensity. Although this assumption is not strictly true, the measurement of the transmittance of the excitation beam through the sample indicated that σ is only very weakly dependent on the excitation fluences of our study.

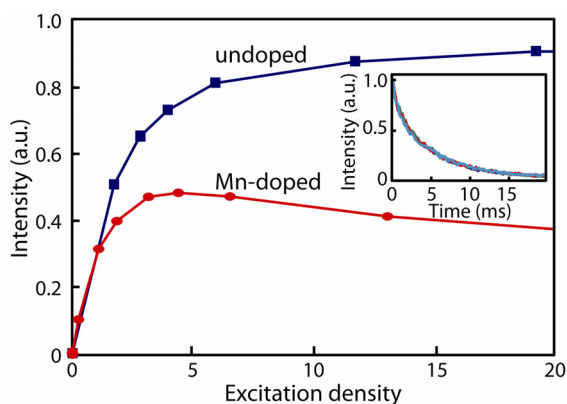


Figure 37. Excitation density-dependent luminescence of undoped and Mn-doped CdS/ZnS core/shell nanocrystals. The lines are the visual guidance. The inset compares the Mn luminescence decay curves at the excitation density of 2.5, 5 and 15 photons/particle.

In Figure 37, the intensity of Mn luminescence in Mn-doped nanocrystals increases initially at low excitation density regime (0 - 3 photons/particle), but decreases as the excitation density increases further. No noticeable change of the luminescence spectrum was observed within the entire range of the excitation density. The inset in Figure 37 shows the decay of Mn luminescence intensity in time at several different excitation densities: 2.5, 5, 15 photons/particle. It shows nearly identical decay at all the excitation densities with the decay time of ~ 5 ms, indicating that the relaxation channels of 4T_1 state do not vary within the range of the excitation densities of this study. The

initial transient lattice temperature rise from the photoexcitation ($\Delta T_{\max} \sim 25$ K for 20 photon/particle.)¹⁰⁹ does not seem to influence the lifetime of 4T_1 state, since the small nanocrystals suspended in liquid solvent cools very rapidly (e.g., ~ 100 ps for <10 nm diameter).¹⁴⁶ On the other hand, the exciton luminescence intensity of undoped nanocrystal sample exhibits a quite different behavior. The exciton luminescence intensity increases initially and saturates at higher excitation densities, consistent with the previous observation made in CdSe nanocrystals by Fisher et al.¹⁴⁷ In undoped nanocrystals, multi-exciton state rapidly falls back to one-exciton state. Therefore, the majority of the exciton luminescence intensity is contributed by the one-exciton state with a minor contribution from the multi-exciton state resulting in the saturation of exciton luminescence intensity as observed.

As mentioned above, the direct resonant excitation from 4T_1 state to conduction band following ET1 is highly unlikely under our experimental condition. However, the depletion of 4T_1 state can occur via two consecutive exciton-Mn energy transfer from multiple number of excitons if both ET1 and ET2 are sufficiently fast compared to the exciton relaxation and decay of the intermediate acceptor state (4T_1). In our previous study, the time scale of ET1 between a pair of exciton and Mn^{2+} ion in Mn-doped CdS/ZnS nanocrystal was determined to be tens of ps for a single exciton-Mn pair and the energy transfer became faster with increasing Mn doping density.⁹⁵ Furthermore, the energy transfer was sufficiently fast even when Auger recombination was present at high exciton densities in the nanocrystals.⁹⁵ Considering that ET1 and ET2 are essentially the same type of energy transfer with a difference in the accepting Mn ligand field

transitions, it is reasonable to expect that the rates of both energy transfer processes are of the similar order of magnitude. In such case, the two consecutive energy transfer can occur before the relaxation of all the excitons when multiple number of excitons are excited in the nanocrystals.

Unlike in usual two-photon processes quadratic to the excitation intensity, the two consecutive exciton-Mn energy transfer processes in Mn-doped nanocrystals will not exhibit such quadratic behavior since the density of excitons varies with time during the energy transfer process. Therefore, hot electron generation via two consecutive energy transfer cannot be confirmed by checking the presence of the quadratic excitation intensity dependence. However, further corroborating evidence for the occurrence of two consecutive exciton-Mn energy transfer can be obtained from the comparison of Mn luminescence intensities under one- and two-pulse excitation condition, as shown in Figure 38. For the two-pulse excitation, the second pulse with the equal intensity as the first pulse is applied 200 ps after the first pulse, which is much longer than the time scale of ET1. At low excitation densities (e.g. <2 photons/particle) the effect of the second pulse is increasing Mn luminescence intensity. On the other hand, the second pulse results in the decrease of Mn luminescence intensity at the excitation densities higher than ~ 3 photons/particle.

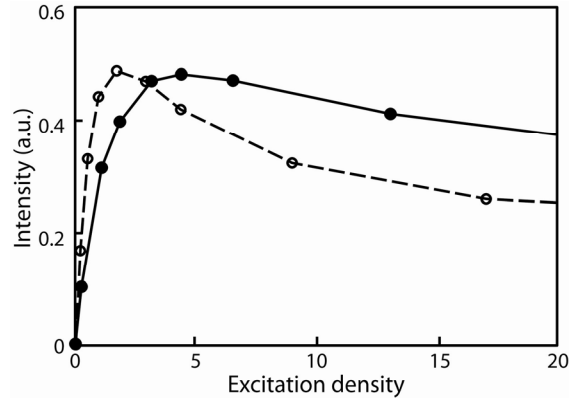


Figure 38. Excitation density-dependent luminescence intensity of Mn-doped and nanocrystals under one-pulse (solid) and two-pulse (dashed) excitation. For the two-pulse excitation, the pulses are separated by 200 ps. The lines are the visual guidance.

The opposite effect of the second pulse on Mn luminescence intensity in different excitation density regimes can be understood from the different relative magnitudes of $k_{ET1}[{}^6A_1]$ and $k_{ET2}[{}^4T_1]$. Here, k_{ET1} and k_{ET2} are the rate constants of ET1 and ET2 processes for a single donor-acceptor pair. $[{}^6A_1]$ and $[{}^4T_1]$ are the populations of the two Mn^{2+} ligand field states at the time of the excitation by the second pulse. Therefore, $k_{ET1}[{}^6A_1]$ and $k_{ET2}[{}^4T_1]$ represent, respectively, the rate of population and depletion of 4T_1 state via energy transfer from each exciton excited by the second pulse. At low excitation densities, $k_{ET1}[{}^6A_1]$ will be larger than $k_{ET2}[{}^4T_1]$ since the majority of Mn^{2+} ions are at the ground 6A_1 state. Therefore, the net effect of the second pulse is increasing the population of 4T_1 state via ET1, resulting in the further increase of Mn luminescence intensity. As the excitation density from the first pulse increases, $k_{ET1}[{}^6A_1]$ decreases while $k_{ET2}[{}^4T_1]$ increases. Therefore, ET2 will become the increasingly more dominating process in the excitation by the second pulse, resulting in the depletion of 4T_1 state and the decrease of Mn luminescence intensity as observed in this study. However,

if ET2 does not occur or is not sufficiently fast compared to the exciton relaxation, the second pulse should result in only the increase and saturation of Mn luminescence intensity as the excitation density increases.

The fact that the second pulse has no net effect on Mn luminescence at the excitation density of ~ 3 photons/particle in the nanocrystals with Mn doping density of 3.6 ions/particle and Mn luminescence quantum yield of $\sim 40\%$ suggest that the rates of ET1 and ET2 are of similar order of magnitude. In principle, Mn luminescence intensity vs. initial excitation density can be simulated with an appropriate kinetic model to extract the rate of ET2 if the rates of all other dynamic processes in play are known. However, the complexity of the kinetics that includes various competing linear and nonlinear processes and uncertainties of some rate parameters, such as the exciton state-dependent Auger recombination, ET1 and ET2 rate constants, make it difficult to extract an accurate rate of ET2 at this point.

Since both ET1 and ET2 are many orders of magnitude faster than the decay of 4T_1 state ($\tau = 5$ ms), two consecutive exciton-Mn energy transfer can generate hot electrons even with *cw* excitation as long as the excitation rate is sufficiently fast to allow ET2 before the decay of 4T_1 state. In this regard, the long 4T_1 state lifetime is particularly beneficial for having consecutive energy transfer from *cw* excitation. Hot electrons generated in Mn-doped nanocrystals in this way can potentially be useful for photocatalytic reduction reaction taking advantage of the lower energy barrier and larger donor-acceptor electronic coupling of the electrons of higher energy for the electron transfer.¹⁴⁸ In order to test whether photocatalysis by Mn-doped nanocrystals can benefit

from consecutive exciton-Mn energy transfer under *cw* excitation, the photocatalytic reduction efficiencies of undoped and Mn-doped nanocrystals were compared at two different excitation conditions: (a) Fast excitation rate allowing consecutive exciton-Mn energy transfer, (b) slow excitation rate with no consecutive exciton-Mn energy transfer. The comparison of the reduction efficiencies was made using the photocatalytic reduction of methylene blue (MB). Photocatalytic reduction of MB in the absence of the dissolved oxygen in solution is known to lead to the disappearance of the color in the visible via the formation of colorless leucomethylene blue.¹⁴⁹ To prevent the degradation of MB via oxidative mineralization by the dissolved oxygen that also result in the loss of color, the measurement was made under O₂-free environment using the deoxygenated dichloromethane as the solvent.¹⁵⁰ Due to the simplicity of the colorimetric measurement, MB has been used to assess the efficiency in heterogeneous photocatalytic reduction in many studies.¹⁵¹⁻¹⁵³

Figure 39a and b compare the decay kinetics of the absorption of MB at 656 nm by undoped (square) and Mn-doped (circle) nanocrystals under 405 nm *cw* excitation at two different excitation conditions mentioned above. For the data in Figure 39a, the average excitation intensity within the full-width at half-maximum (fwhm) from a 405 nm diode laser was 760 mW/cm² corresponding to the average excitation rate of 12 excitations/⁴T₁ lifetime for each particle. At this excitation rate, two consecutive energy transfer can occur in Mn-doped nanocrystals. For the data in Figure 39b, a 405 nm light emitting diode was used for the excitation at the intensity of 1.2 mW/cm² corresponding

to the average excitation rate of 0.02 excitations/ 4T_1 lifetime. At his slow excitation rate, only the isolated single energy transfer events can occur in Mn-doped nanocrystals.

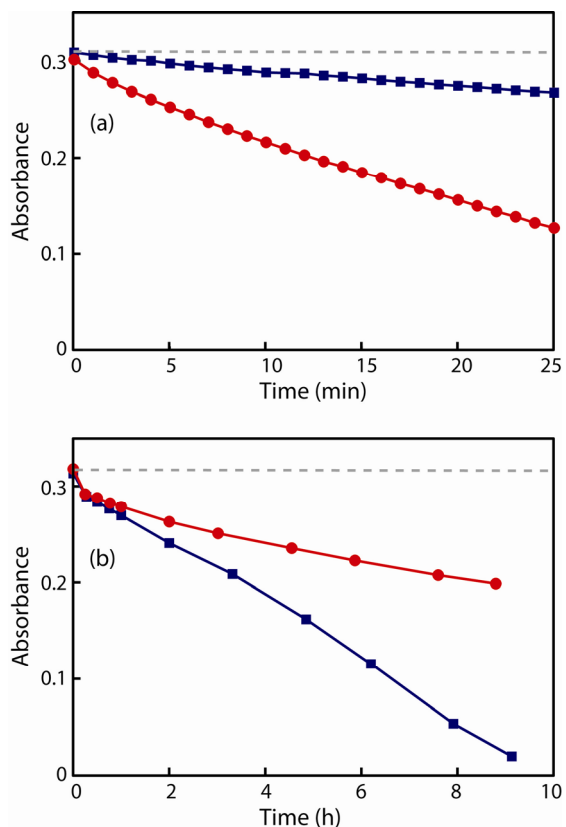


Figure 39. Photocatalytic reduction of MB in undoped (square) and Mn-doped (circle) solution under (a) 760 and (b) 1.2 mW/cm² 405 nm *cw* excitation. The solid lines are the visual guidance. The dashed lines are the initial absorbance of MB.

In Figure 39a, the kinetics is ~ 4 times faster in Mn-doped nanocrystals than in undoped nanocrystals. On the other hand, undoped nanocrystals exhibit the faster kinetics than Mn-doped nanocrystals in Figure 39b. The opposite trend of the photocatalytic efficiencies of Mn-doped and undoped nanocrystals under the two different excitation conditions may be explained in the following way. At the slower

excitation rate, the role of exciton-Mn energy transfer is simply decreasing the exciton density within the nanocrystals resulting in the lower photocatalytic reduction efficiency of Mn-doped nanocrystals compared to the undoped ones. At the higher excitation rate, two consecutive exciton-Mn energy transfer can generate hot electrons and localized holes. Hot electrons with a large excess energy can exhibit higher reduction efficiency than electrons from near-band edge excitons in undoped nanocrystals, more than compensating the smaller number of electrons generated. The above result indicates that consecutive energy transfer in Mn-doped nanocrystals has a beneficial effect in photocatalysis, while further studies on the reaction involving both electron and holes are needed to reveal its full potential.

6.3 Conclusions

In summary, we investigated the occurrence of consecutive exciton-Mn energy transfer in Mn-doped semiconductor nanocrystals that can generate hot electrons with a large excess energy in conduction band. Due to the fast exciton-Mn energy transfer and long lifetime of the intermediate acceptor state, two consecutive exciton-Mn energy transfer can occur efficiently even with relatively weak *cw* excitation. Under the excitation condition that supports consecutive exciton-Mn energy transfer responsible for hot electron generation, Mn-doped nanocrystals exhibit the higher photocatalytic reduction efficiency than undoped nanocrystals.

6.4 Experimental Section

The synthesis of Mn-doped and undoped CdS/ZnS nanocrystals follows the procedures described in Chapter III. The resulting nanocrystals have core diameter and shell thickness of 3.6 nm and 1.8 nm, respectively. The doping concentration is 3.6 Mn²⁺ ions per nanocrystals determined from ICP-MS.

The exciton and Mn luminescence intensities of undoped and Mn-doped nanocrystals were measured with 395 nm pulsed excitation within the fluence range of 0 - 4.6 mJ/cm² per pulse. The excitation pulses were generated by frequency doubling 790 nm output from a Ti:Sapphire laser in a β -barium borate (BBO) crystal. The nanocrystal solution in hexane was circulated in a 1 mm-thick liquid cell at the linear flow rate of \sim 1 cm/s to avoid any potential photodegradation of the nanocrystals by the excitation pulse. The repetition rate of the excitation pulse was set at 50 Hz, much slower than the relaxation time of ⁴T₁ state on Mn²⁺ ions, to avoid the reexcitation of Mn-doped nanocrystal before the complete decay of Mn luminescence. The optical setup for the measurement of the luminescence intensity and lifetime is shown in Figure 40a. In order to obtain an accurate correlation between the luminescence intensity and excitation density of the nanocrystal (number of photons absorbed per particle), the spatial intensity profiles of both the excitation pulse and luminescence from the sample were measured. The spatially resolved detection of the luminescence intensity is particularly important when using excitation source with a small beam diameter. This is because Mn luminescence intensity becomes nonlinear to the excitation intensity as the excitation

intensity increases resulting in the mismatch of the spatial intensity profiles of excitation beam and Mn luminescence at higher excitation intensities.

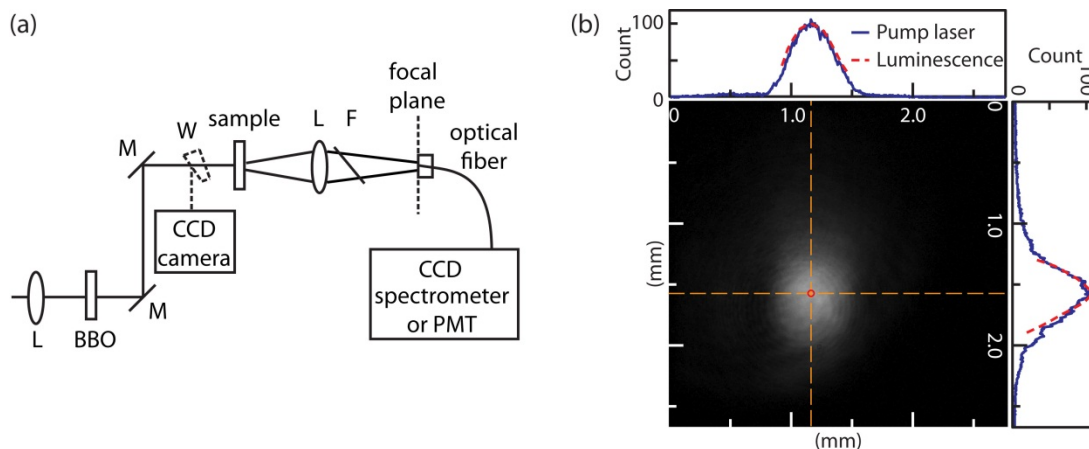


Figure 40. (a) Experimental setup for the measurement of excitation density-dependent luminescence intensity. L, M, W, and F are lens, dielectric mirror, wedge beam splitter, and filter respectively. (b) 2-dimensional intensity profile of the excitation pulse at a low excitation fluence. The top and right panels compare the line profiles of the excitation (solid) and Mn luminescence intensities (dashed) in two directions indicated with the dashed line.

The intensity profile of the excitation pulse was directly imaged with a CCD camera using a wedge beam splitter placed in front of the sample cell. The beam diameter (full width at half maximum) measured in this way was $\sim 500 \mu\text{m}$. The intensity profile of the luminescence from the sample was measured by imaging the luminescence on the entrance of an optical fiber ($50 \mu\text{m}$ in diameter) mounted on an x-y translation stage. The exit side of the optical fiber was connected to a CCD spectrometer (QE65000, Ocean Optics) that measured both the spectrum and intensity the luminescence as a function of the position of the optical fiber. The intensity profile of the luminescence was obtained by raster scanning the optical fiber. Figure 40b shows the spatial intensity

profile of the excitation pulse at a low excitation fluence regime, where the luminescence intensity increases linearly with the excitation fluence. The line profiles of the excitation beam and Mn luminescence intensities are almost identical under this condition as shown on the top and right panels of Figure 40b. However, the two intensity profiles become more dissimilar as the excitation fluence increases. In this study, the excitation and luminescence intensities at the center of the peak within 50 mm diameter were taken to obtain excitation density-dependent luminescence intensity. For the lifetime measurement, the optical fiber was connected to a photomultiplier tube (931A, Hamamatsu), and the data were collected by a digital oscilloscope (TDS 2022B, Tektronix).

The kinetics of photocatalytic reduction of MB by undoped and Mn-doped nanocrystals was studied under 405 nm *cw* excitation. All the sample solutions were prepared in a N₂-atmosphere glove box. Dichloromethane bubbled with N₂ for more than 1 hr was used as the solvent to prevent oxidative photodegradation of MB by the dissolved oxygen. For the comparative measurement of the photoreduction rate by undoped and Mn-doped nanocrystals, concentrations of MB (6.1 μM) and nanocrystal (0.23 μM) and the total volume (2.1 ml) of the sample solution were kept identical for all the measurements. The sample solutions in the cuvette with an air-tight cap were illuminated at two different excitation intensities: 760 and 1.2 mW/cm² using a diode laser and a light emitting diode respectively. The absorbance of MB at 656 nm was recorded as a function of time to monitor the reduction kinetics. MB has negligible absorption at the excitation wavelength and the illumination of the sample solution

containing only MB showed virtually no change of absorbance during the period of the time of the measurements.

CHAPTER VII
CONTROLLED LOCAL LATTICE STRAIN TUNES TEMPERATURE
DEPENDENCE OF Mn LUMINESCENCE IN Mn-DOPED CORE/SHELL CdS/ZnS
NANOCRYSTALS

7.1 Introduction

Lattice strain has been utilized as a unique way to control the optical, electronic and transport properties of various nanocrystalline materials. In one-dimensional materials, band structure and electrical conductivity of carbon nanotubes and ZnO nanowires were varied by the lattice strain created by bending or torsional stress.¹⁵⁴⁻¹⁵⁶ In zero-dimensional semiconductor nanocrystals, lattice strain from the lattice mismatch at the core/shell interface was shown to have a large effect on the bandgap in type II quantum well structures.^{157,158} Recently, the variation of the local lattice strain and pressure in doped core/shell semiconductor nanocrystals was used to controllably modify the electronic structure of the dopant ions as well.^{66,83} These earlier studies showed that lattice strain in core/shell nanocrystals can tune the optical properties of not only the exciton of the semiconductor host but also the dopant ions.

In this study, we show that the controlled local lattice strain in Mn-doped core/shell semiconductor nanocrystals can be used to vary the vibronic coupling of Mn luminescence and tune the temperature dependence of the luminescence spectrum. In addition, the experimental data suggest that the local thermal expansion near Mn²⁺ ions may also be enhanced by the local lattice strain, increasing the spectral shift of Mn

luminescence with the change of temperature. The Mn luminescence spectrum at a given temperature is determined by the thermally-averaged Franck-Condon factor, which is characterized by Huang-Rhys factor and the frequencies of the vibrational modes coupled to ${}^4T_1 \rightarrow {}^6A_1$ transition of Mn^{2+} ion. These two parameters dictating the temperature-dependent spectral lineshape of Mn luminescence are sensitive to the local lattice structure around Mn^{2+} ions. Therefore, the ability to control the local lattice strain at the dopant site can be utilized to control the temperature dependence of the spectral characteristics of Mn^{2+} ions. The exploration of the local lattice strain as an independent variable tuning the optical properties of doped nanocrystals can potentially be more generally extended to the luminescence of many other doped nanocrystals.^{23,26} Since the origins of the dopant luminescence is localized on the dopant or partially involve the charge carrier localized near the dopant, local lattice strain can have a significant influence on the dopant-related luminescence unlike in luminescence of the delocalized exciton in quantum dots.

Here, we investigated how the variation of the local lattice strain at the dopant site affects the temperature dependence of Mn luminescence bandwidth and peak position. For this purpose, we used Mn-doped CdS/ZnS nanocrystals, where the local lattice strain at the dopant site is systematically varied by controlling the radial doping location. We observed that the bandwidth and peak position of Mn luminescence show the stronger temperature dependence as Mn^{2+} ions are doped closer to the core/shell interface having the maximum lattice strain. This observation can be explained by the

increasing softening of the coupled vibrational mode and enhanced local thermal expansion as the anisotropic lattice strain at the dopant site increases.

The present work demonstrates the possibility of using the controlled local lattice strain in doped nanocrystals to modify the local vibronic coupling and thermal property to vary the temperature-dependent spectral characteristics of the dopant-related luminescence. The tunable temperature dependence of Mn luminescence bandwidth and peak position via the local lattice strain also bears importance in the dynamics of exciton-Mn energy transfer process responsible for Mn luminescence. Since the energy transfer rate depends on the donor-acceptor spectral overlap, varying the temperature dependence of the accepting Mn^{2+} transition can affect the energy transfer rate.⁸⁶ The understanding of the role of local lattice strain in the temperature dependence of the dopant luminescence will be valuable in addressing the temperature-dependent energy transfer dynamics.

7.2 Results and Discussion

7.2.1 Variation of Local Lattice Strain at Dopant Site

Varying local lattice strain at the dopant site was achieved by controlling the radial doping location of Mn^{2+} ions for a given CdS/ZnS core/shell host structure following the previously published procedures.³⁷ (Figure 41a) The nanocrystal samples used in this study is the same as the $\langle n_{\text{Mn}} \rangle = \sim 6$ and ~ 22 samples used in Chapter V, i.e., the diameter of core is 3.6 nm and the thickness of the shell is 1.8 nm. Mn^{2+} ions were doped at 0, 2, and 4 monolayers away from the core/shell interface. The thickness of a

monolayer of ZnS in the shell is 0.31 nm. Since the direct measurement of the local lattice strain is difficult, the lattice strain in the core and shell of the undoped host was calculated using a simple continuum model assuming the spherical core and shell of zinc blende structure that are continuous at the interface.^{159,160} Details of the calculation are in Section 7.4. The calculated strain in the radial and tangential direction of the core and shell are plotted in Figure 41b. In bulk phase, CdS has larger lattice parameter (5.82 Å) than ZnS (5.41 Å), introducing 7.6% lattice mismatch at the core/shell interface.^{141,161} Therefore, in CdS/ZnS core/shell nanocrystals, CdS core shrinks while ZnS shell expands in the tangential direction to maintain the continuity of the lattice at the interface. In this model, the core experiences contraction in both radial and tangential direction. On the other hand, the shell experiences a biaxial strain: tangential expansion and radial contraction. The strain on the shell is the largest at the core/shell interface and gradually decreases as the radius increases. Although the above calculation based on the continuum model has a limitation in accurately calculating the local variation of the lattice strain of the real core/shell nanocrystals, it captures the key aspects of the spatial variation of the local lattice strain, such as the contraction in the CdS core and biaxial strain in the ZnS shell.

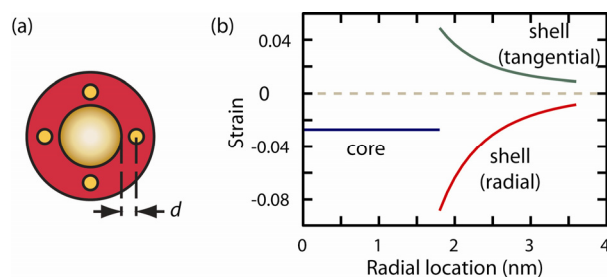


Figure 41. (a) Schematic diagram of the structure of the Mn-doped CdS/ZnS nanocrystals. d is the distance between the core/shell interface and the Mn^{2+} ions (yellow dots). (b) Strain profile of the CdS/ZnS core/shell nanocrystal with core radius and shell thickness of 1.8 and 1.8 nm, respectively.

The local lattice strain at the dopant site directly influences the ligand field and bond strength around Mn^{2+} ions determining their electronic and vibrational energy structure. Therefore, the ability to control the local lattice strain allows tuning of the dopant luminescence spectrum and its temperature dependence. In this study, we focus on investigating how the controlled lattice strain in the core/shell structure varies the temperature dependence of the bandwidth and peak position of Mn luminescence via the modification of the local vibronic coupling.

7.2.2 Temperature-Dependent Mn Luminescence Bandwidth vs Local Lattice Strain

We first analyze the temperature-dependent bandwidth of Mn luminescence at various doping locations. Figure 42 shows the Mn luminescence spectra of Mn-doped CdS/ZnS nanocrystals at three radial doping locations and two doping concentrations in the temperature range of 5-320 K. Since the samples used in this chapter are the same as some of the samples in Chapter V, the same sample codes are used. Doping location (d) is labeled as **a**, **b**, and **c** for doping at 0, 2, and 4 monolayers of ZnS above the core/shell

interface, respectively. The average doping concentration ($\langle n_{\text{Mn}} \rangle$) is labeled as **1** and **3** for $\langle n_{\text{Mn}} \rangle = \sim 6$ and ~ 22 ions/particle, respectively. For all the samples, the luminescence bandwidth increases with increasing temperature, due to the increasing population of the higher vibronic levels of the emitting ligand field state of Mn^{2+} ion (${}^4\text{T}_1$). A clearly visible trend is that the nanocrystals with Mn^{2+} ions doped closer to the core/shell interface exhibit the larger temperature dependence of both the bandwidth and peak position of Mn luminescence. For a given doping location, the nanocrystals with higher doping concentration show stronger temperature dependence. In Mn-doped ZnS nanocrystals without lattice strain from core/shell lattice mismatch, both the bandwidth and the peak position exhibit relatively weak temperature dependence similar to the case of sample **c1**.¹⁶²

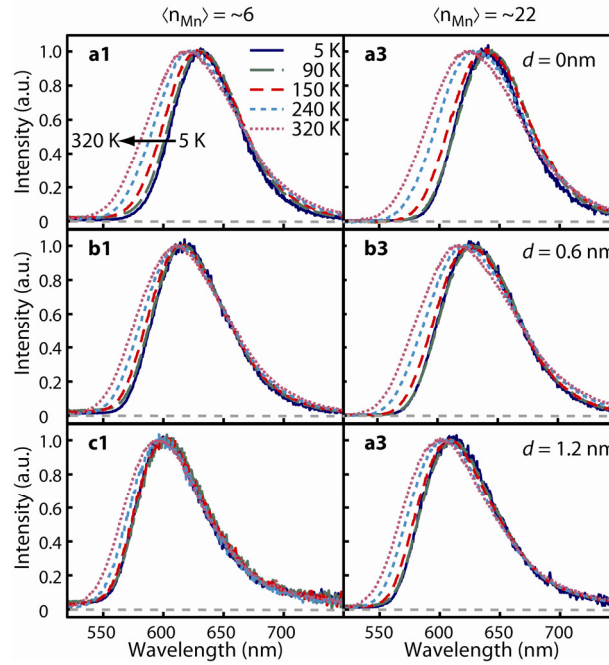


Figure 42. Temperature-dependent Mn luminescence spectra of Mn-doped CdS/ZnS nanocrystals with varying radial doping locations (d) and doping concentrations ($\langle n_{\text{Mn}} \rangle$). Different doping locations are labeled as **a**, **b**, and **c** for $d = 0, 2$ and 4 monolayers (ML) of ZnS above the core/shell interface, respectively. Different doping concentrations are labeled as **1** and **3** for $\langle n_{\text{Mn}} \rangle = \sim 6$ and ~ 22 , respectively.

For a more quantitative comparison of the temperature-dependent bandwidth, the raw luminescence spectra, $I(\lambda)$, typically expressed in counts/nm vs. wavelength (nm) are converted into the spectra on energy axis, $I(E)$, in counts/eV vs. eV by multiplying $I(\lambda)$ with λ^2 . $I(E)$ is further converted to the spectral lineshape, $L(E)$, as shown in eq 19, where E is the photon energy. The conversion of $I(E)$ to $L(E)$ is needed for the analysis of bandwidth since $L(E)$ directly represents Franck-Condon factor, $\text{FC}(E)$, while $I(E)$ includes E^3 weighting factor to $\text{FC}(E)$.^{163,164}

$$L(E) = I(E)/E^3 = (32\pi^3/3\hbar^4 c^3)n^3|M|^2 \text{FC}(E) \quad (19)$$

Here, c , n , and M are speed of light, optical dielectric constant, and transition dipole moment, respectively. The Mn luminescence spectra converted to spectral lineshape, $L(E)$, are shown in Figure 43.

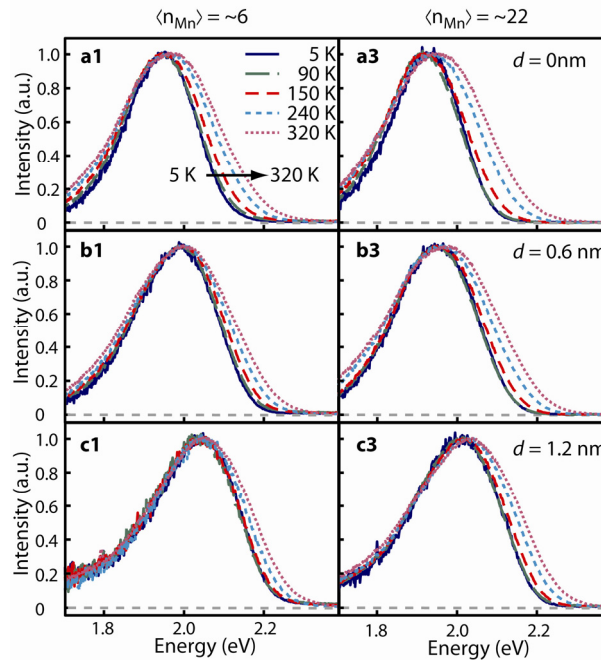


Figure 43. Temperature-dependent Mn luminescence spectral lineshape of Mn-doped CdS/ZnS nanocrystals with varying radial doping locations (d) and doping concentrations ($\langle n_{Mn} \rangle$). Different doping locations are labeled as **a**, **b**, and **c** for $d = 0$, 2 and 4 monolayers (ML) of ZnS above the core/shell interface, respectively. Different doping concentrations are labeled as **1** and **3** for $\langle n_{Mn} \rangle \approx 6$ and ≈ 22 , respectively.

The temperature-dependent full-width at half maximum (fwhm), $\Gamma(T)$, obtained from the Mn luminescence lineshape described above is plotted in Figure 44a and b. Two trends are readily identified from these data. Firstly, fwhm at 5 K, $\Gamma(5\text{ K})$, decreases with increasing local lattice strain. For instance, $\Gamma(5\text{ K})$ of sample **a1** is 20% smaller than sample **c1**. Changing the average doping concentration from $\langle n_{Mn} \rangle \approx 6$ to

~ 22 has only a minor effect on $\Gamma(5\text{ K})$ with $\sim 1\%$ difference. Secondly, the slope of $\Gamma(T)$ vs. T increases with increasing lattice strain. In Figure 44c and d, fwhm normalized to the value at 5 K, $\Gamma(T)/\Gamma(5\text{ K})$, is plotted. The rate of temperature broadening of $\Gamma(T)/\Gamma(5\text{ K})$ in the linear regime in sample **a1** is faster than in sample **c1** by over 100%.

At 5 K, kT is sufficiently lower than the vibrational energy of the lattice and $\Gamma(5\text{ K})$ is essentially identical to $\Gamma(0\text{ K})$. If the heterogeneous broadening can be ignored, $\Gamma(0\text{ K})$ reflects the vibronic coupling of ${}^4T_1 \rightarrow {}^6A_1$ transition and is expressed as follows.⁸⁷

$$\Gamma(0\text{ K}) = [8(\hbar\omega)^2 S \ln(2)]^{1/2} \quad (20)$$

Here, ω is the frequency of the vibrational mode coupled to ${}^4T_1 \rightarrow {}^6A_1$ transition of Mn^{2+} ions and S is Huang-Rhys factor. Therefore, one could interpret the decrease in $\Gamma(5\text{ K})$ with increasing lattice strain in terms of the decrease in the combined parameter of the frequency of the coupled vibrational mode and Huang-Rhys factor, $\omega S^{1/2}$. Alternatively, heterogeneity of the local lattice strain due to the finite width of the radial doping location in the nanocrystals may be invoked to explain the variation of $\Gamma(5\text{ K})$ among the different samples. However, this is a less probable scenario for the following reasons. If the heterogeneity of the radial doping location is mainly responsible for the differences in $\Gamma(5\text{ K})$, $\Gamma(5\text{ K})$ of sample **a1** should be larger than sample **c1**. Since the gradient of the lattice strain increases towards the core/shell interface, the effect of the heterogeneity in the lattice strain at the dopant site on $\Gamma(5\text{ K})$ should become larger as the dopant ions get closer to the core/shell interface. The fact that the measured $\Gamma(5\text{ K})$ exhibits the opposite

trend and that there is little dependence of $\Gamma(5\text{ K})$ on the doping concentration argues against this alternative explanation.

An insight into the origin of the decreasing fwhm with increasing lattice strain at 5 K can be obtained from the rate of variation of $\Gamma(T)/\Gamma(5\text{ K})$ vs. T . Assuming that $\Gamma(5\text{ K})$ is similar to $\Gamma(0\text{ K})$, $\Gamma(T)/\Gamma(5\text{ K})$ data can be fit to $[\coth(\hbar\omega/2kT)]^{1/2}$, which describes the temperature dependence of the bandwidth of the luminescence lineshape.^{87,162} From this fit, information on the frequency of the coupled vibrational mode (ω) can be extracted. Solid lines in Figure 44c and d are the fitting results. The values of ω determined from the fit are summarized in Table 6. According to this analysis, ω decreases with increasing local lattice strain as Mn^{2+} ions get closer to the core/shell interface. As the doping location changes from 4 to 0 monolayers above the core/shell interface, the value of ω decreases by 30-40 %. These observations indicate that the softening of the vibrational mode with increasing lattice strain contributes to the narrower bandwidth at 5 K in sample **a1** than in **c1**.

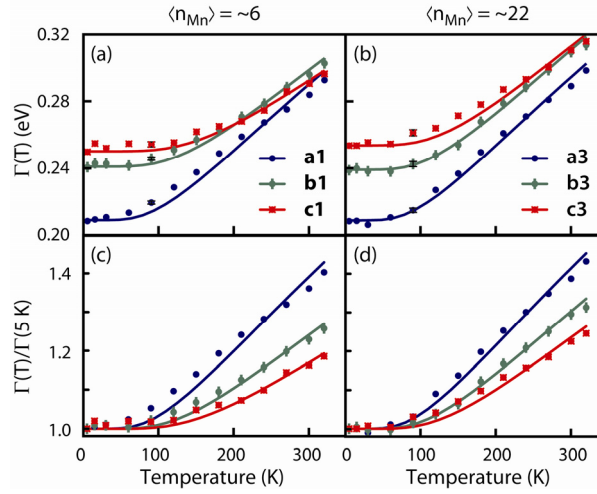


Figure 44. (a), (b) Temperature-dependent Mn luminescence bandwidth, $\Gamma(T)$, for $\langle n_{Mn} \rangle = \sim 6$ and ~ 22 , respectively. (c), (d) Temperature dependence of $\Gamma(T)/\Gamma(5 \text{ K})$ for $\langle n_{Mn} \rangle = \sim 6$ and ~ 22 with the same color code as (a) and (b), respectively. Dots and lines are experimental data and the fit to $[\coth(\hbar\omega/2kT)]^{1/2}$, respectively. Error bars are indicated only in (a) and (b).

Table 6. Vibrational Frequency (ω) at Varying Doping Location (d) and Concentration ($\langle n_{Mn} \rangle$) from the Fit of Mn Luminescence Bandwidth vs. Temperature.

| sample | d (monolayer) | $\langle n_{Mn} \rangle$ | ω (cm^{-1}) ^a |
|-----------|-----------------|--------------------------|--|
| a1 | 0 | 5.3 | 238(11) |
| b1 | 2 | 6.1 | 322(11) |
| c1 | 4 | 6.4 | 387(19) |
| a3 | 0 | 20 | 229(7) |
| b3 | 2 | 24 | 282(5) |
| c3 | 4 | 21 | 327(15) |

^aThe numbers in the parenthesis are the uncertainty of the fit.

For a given doping location, ω is lower for the nanocrystals with the higher doping concentration. The difference in ω ($\Delta\omega$) between $\langle n_{Mn} \rangle = \sim 6$ and ~ 22 is less than

4% for the interfacial doped nanocrystal samples **a1** and **a3**. $\Delta\omega$ becomes larger as the local lattice strain decreases, reaching 15% for the samples **c1** and **c3**. The additional softening of the coupled vibrational mode at the higher doping concentration may be due to the smaller lattice parameter of zinc blende MnS (5.22 Å) than ZnS (5.41 Å), which provides further lattice strain of the host when the doping concentration is higher.¹⁶⁵

Interestingly, while the effect of increasing the local lattice strain on the spectral shift of Mn luminescence appears similar to the increase in the local pressure, the effect on ω is the opposite. The red-shift of Mn luminescence from the variation of the local pressure due to the lattice strain in Mn-doped CdS/ZnS core/shell nanocrystals is similar to the red-shift observed in Mn-doped ZnS under the hydrostatic pressure at the rate of -30 meV/GPa.^{83,166} On the other hand, ω in Table 6 exhibit red-shift with increasing lattice strain in contrast to the blue-shift of optical phonons of ZnS under the same hydrostatic pressure.^{167,168} Such opposite effect on the vibrational frequency may be due to the differences in the nature of the lattice strain created by the hetero interface and the hydrostatic pressure, i.e., anisotropic vs. isotropic strain. In fact, in superlattice of CdS/ZnS and ZnSe/ZnS, where ZnS experiences the anisotropic biaxial lattice strain of the opposite signs to the longitudinal and transverse directions, optical phonons exhibited red-shift with increasing lattice strain.^{169,170} The red-shift of phonons with increasing biaxial strain in the superlattice is qualitatively similar to what is observed in the vibrational mode coupled to Mn luminescence in Mn-doped core/shell nanocrystals in our study.

It is also notable that the magnitude of the variation of ω from anisotropic local lattice strain in core/shell nanocrystals is significantly larger than the variation of the phonon frequency expected under the isotropic strain of the similar magnitude. In the case of longitudinal optical (LO) phonon of ZnS, hydrostatic pressure of 15 GPa that isotropically compresses the lattice by $\sim 5\%$ results in $\sim 15\%$ increase in the phonon frequency compared to 30-40 % decrease of ω with comparable anisotropic lattice strain in the core/shell structure.^{167,168} This suggests that the lattice strain from the interfacial lattice mismatch can be more effective in modifying the vibrational mode coupled to the electronic transition of the dopant than the external pressure.

So far, we discussed the effect of varying local lattice strain at the dopant location on the frequency of the coupled vibrational mode without assigning the mode. Although the longitudinal optical phonon has been considered as the coupled mode, it should be a vibrational mode on a more local scale considering the high sensitivity of ω on the doping location.^{162,171} One can speculate that the vibrations in the tetrahedral MnS_4 unit are the most relevant in the vibronic coupling of ${}^4\text{T}_1 \rightarrow {}^6\text{A}_1$ transition. Usually resonance Raman can give information about the vibrational modes and their displacement upon the coupled electronic transition. However, it is difficult to obtain such information in Mn-doped nanocrystals due to very weak transition dipole of the ligand field transition of Mn^{2+} ions. To elucidate the correlation between local lattice strain, the vibrational mode, and the frequency coupled to the Mn luminescence, a detailed computational study on the local lattice structure and the vibrational spectrum in Mn-doped core/shell nanocrystals is underway.

7.2.3 Effect of Local Lattice Strain on Temperature-Dependent Peak Shift

Figure 45a and b show ΔE_{0-0} defined as the shift of the 0-0 transition energy (E_{0-0}) of Mn luminescence with respect to the lowest value of E_{0-0} as a function of temperature. E_{0-0} was determined by fitting the experimental Mn luminescence lineshape to the lineshape function in eq21, which represents the thermally averaged vibronic transition coupled to a single vibrational mode.¹⁷²

$$L(E) = A \exp[-S \coth(\hbar\omega/2kT) + (E_{0-0} - E)/2kT] J_n(z) \quad (21)$$

A is a constant for normalizing the spectral amplitude. $J_n(z)$ is the Bessel function of the first kind with imaginary argument, where $n = (E_{0-0} - E)/\hbar\omega$ and $z = S \operatorname{csch}(\hbar\omega/2kT)$. In this fit, the vibrational frequency (ω) and Huang-Rhys factor (S) obtained from the analysis described in the previous section was used. The quality of the fit is excellent as shown in Figure 47 of Section 7.4.

For all the Mn-doped CdS/ZnS nanocrystals, E_{0-0} blue-shifts to higher energy with the increase of temperature in the range of 90-320 K. Below ~ 50 K, E_{0-0} red-shifts with the increase of temperature. For comparison, ΔE_{0-0} in Mn-doped ZnS nanocrystals with $\langle n_{\text{Mn}} \rangle = 17$ is also shown in Figure 45b. The magnitude of the temperature dependence of ΔE_{0-0} is the largest in the interfacial-doped nanocrystals (**a1** and **a3**). For a given doping location, the samples with the higher doping concentration results in the larger shift with temperature change.

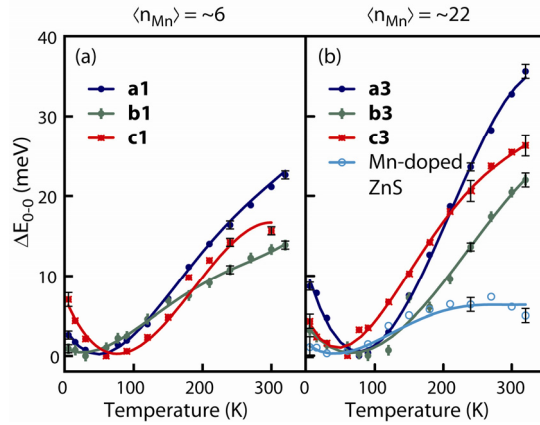


Figure 45. (a), (b) Temperature-dependent relative Mn luminescence 0-0 transition energy (ΔE_{0-0}) for $\langle n_{\text{Mn}} \rangle \approx 6$ and ≈ 22 , respectively. ΔE_{0-0} for Mn-doped ZnS has is also shown in (b). The curves are the visual guidance only.

According to the earlier studies on the temperature dependent spectral lineshape of the doped ions in the crystalline host matrix, temperature shift of E_{0-0} has two main contributions. One is the thermal expansion of the lattice that changes the ligand field strength around the dopant ions, therefore changing the ligand field transition energy.^{162,173} In high-spin d5 system of Mn^{2+} ion, ${}^4T_1 \rightarrow {}^6A_1$ transition energy increases with decreasing ligand field splitting ($10 Dq$) with lattice expansion. Therefore, thermal expansion of the lattice results in the blue-shift of E_{0-0} . The second contribution arises from the difference in the frequencies of the coupled vibrational mode in the ground and excited electronic states. When the vibrational frequency is higher in the excited electronic state (4T_1), as in d5 high-spin system, the second contribution also results in the blue-shift with increasing temperature.^{162,173} However, the second contribution is usually less significant than the thermal expansion in the temperature dependence of E_{0-0} . In the case of Mn-doped ZnS nanocrystals, Mn luminescence blue-shifts by ~ 6 meV as

the temperature increases from 50 to 320 K. With this temperature change, ZnS lattice expands by 0.11% in bulk phase.^{141,158} According to the pressure-dependent peak shift measurement made in Mn-doped ZnS, the hydrostatic pressure that contracts the host lattice by $\sim 0.11\%$ results in the red-shift of Mn luminescence by ~ 8 meV.^{166,174} Therefore, the observed shift of E_{0-0} in Mn-doped ZnS nanocrystals can be accounted for primarily by the thermal expansion of ZnS host.

On the other hand, ΔE_{0-0} shows much stronger temperature dependence in Mn-doped core/shell CdS/ZnS nanocrystals than in Mn-doped ZnS nanocrystals. In sample **a3**, which has the largest lattice strain and the higher doping concentration, ΔE_{0-0} varies with temperature ~ 6 times faster than in Mn-doped ZnS nanocrystals between 50-320 K. Furthermore, the reversal of the slope of ΔE_{0-0} below ~ 50 K is more pronounced in all the core/shell nanocrystal samples. We first focus on the blue-shift with increasing temperature above ~ 50 K. We attributed the enhanced temperature dependence of E_{0-0} to the higher local thermal expansion at the dopant site in the Mn-doped core/shell nanocrystals based on the discussion above. Thermal expansion originates from the anharmonicity of the lattice potential.¹⁷⁵ The distortion of the local lattice structure at the dopant site from the anisotropic local lattice strain with opposite signs in the tangential and radial directions may have enhanced the anharmonicity of the local vibration near the dopant site, leading to an increase in the local thermal expansion. Since the local lattice strain is the largest at the core/shell interface and the higher doping concentration can impose an additional lattice distortion, sample **a3** should show the largest temperature dependence of ΔE_{0-0} as observed experimentally.

At temperatures below ~ 50 K, the luminescence red-shifts with the increase of the temperature in contrast to the blue-shift observed at higher temperatures. Also, the amplitude of the red-shift is much larger in CdS/ZnS core/shell host than in ZnS host. Such reversal of the slope of E_{0-0} vs. T has been previously observed in heavily doped bulk $\text{Cd}_{1-x}\text{Mn}_x\text{Te}$ and $\text{Zn}_{1-x}\text{Mn}_x\text{Se}$, where the doping concentration was a few to tens of %.^{173,176,177} The red-shift in temperature range of $< \sim 50$ K in these heavily doped bulk materials was tens of meV. Antiferromagnetic coupling or superexchange coupling between the neighboring Mn^{2+} ions that are not thermally destroyed only at sufficiently low temperatures was considered responsible for the red-shifts of Mn luminescence with temperature increase below ~ 50 K. However, considering the much lower doping concentration (0.1-0.5%) in the nanocrystals studied here, it is uncertain whether the red-shift observed in our study can be explained in the same way as in the heavily doped materials. The fact that Mn-doped ZnS nanocrystals exhibit a very small shift of E_{0-0} (< 1 meV) below ~ 50 K indicates that the effect of antiferromagnetic coupling or superexchange coupling between Mn^{2+} ions is negligible in ZnS nanocrystal host. While the enhanced local thermal expansion in Mn-doped CdS/ZnS core/shell nanocrystals may enhance antiferromagnetic coupling and superexchange coupling at low temperatures via larger changes in lattice parameter, further investigation is needed for a clearer explanation.

7.3 Conclusions

In summary, we studied the effect of varying the local lattice strain at the dopant site in Mn-doped CdS/ZnS core/shell nanocrystals on the temperature dependence of Mn luminescence bandwidth and peak shift. In this study, the doped core/shell nanocrystals with lattice mismatch provided a unique platform to vary the local lattice strain at the dopant site via controlled radial doping location. With the increase of the local lattice strain at the dopant site, the bandwidth of Mn luminescence showed the larger temperature dependence. This was explained by the softening of the vibrational mode coupled to ${}^4T_1 \rightarrow {}^6A_1$ transition of Mn^{2+} ions with increasing lattice strain. In addition, the shift of Mn luminescence peak with the temperature change also became stronger with increasing lattice strain and increasing doping concentration. This was ascribed to the enhanced local thermal expansion, which may arise from the enhancement of anharmonicity of the local lattice potential near the dopant ions due to the local lattice strain. The present study demonstrates that the controlled local lattice strain at the dopant site in doped core/shell nanocrystals can be used to vary the temperature dependence of the width and energy of the local dopant luminescence spectrum via structurally modified local vibronic coupling and local thermal expansion.

7.4 Experimental Section

The nanocrystal samples used in this study is the same as that in Chapter V.

The nanocrystals samples in the mixture of poly(methyl methacrylate) and chloroform are spin-coated on the sapphire substrates. The samples were sealed in

vacuum in an open-cycle cryostat (ST-100, Janis), with liquid nitrogen or liquid helium used as the cryogen. Mn-doped CdS/ZnS nanocrystals were excited at 403 nm using *cw* diode laser or xenon lamp. The power of the laser was kept below ~ 1 mW with 3 mm beam size to avoid the heating of the substrate. Mn-doped ZnS nanocrystals were excited at 325 nm using xenon lamp. 450 nm long pass filter was used to block the excitation light in the measurement of the spectrum. Non-flat transmittance spectrum of the long pass filter was taken into account in the analysis of the spectral lineshape. The luminescence spectra were measured with two different spectrometers (QE65000, Ocean Optics and Fluorolog 3, Horiba), which give the identical lineshape after the intensity calibration. Comparisons of the intensity-calibrated spectra taken with the two spectrometers are shown in Figure 46.

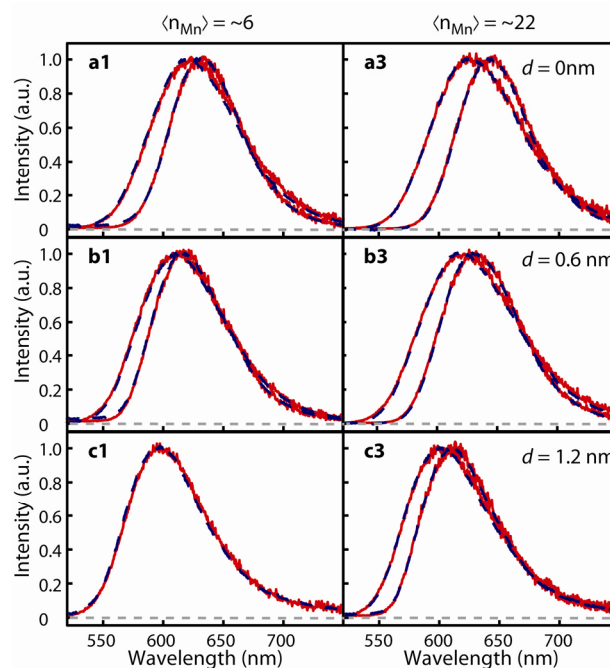


Figure 46. Comparison of Mn luminescence spectra taken at 90 K (right and narrow peaks in each panel except for **c1**) and 300 K (left and broad peaks in each panel) with QE65000 (dashed) and Fluorolog 3 (solid). Excitation wavelength for all the data is 403 nm.

Calculation of the Strain Profile in Spherical CdS/ZnS Core/Shell Nanocrystals.

The strain profile of the CdS/ZnS core/shell nanocrystals was calculated based on a hollow sphere model with the boundary condition that the lattice is continuous at the hetero-interface with no defect (i.e., no missing or extra atom).^{159,160,178} This model has been previously used for the calculation of strain and pressure profile in core/shell nanocrystals.^{83,157} Here we summarize the key equations. The nanocrystal has core radius (r^c) and total radius (R) of 1.8 and 3.6 nm with internal and external pressure of P_i and P_o . The external pressure is ignored since the internal pressure induced by the lattice mismatch is much higher than the external pressure. Therefore, the radial displacement

of the shell in spherical coordinate is reduced to eq 22. Assuming the core is under isotropic pressure, the radial displacement of the core is given by eq 23.

$$u_r^s = \frac{r(1+\nu^s)}{Y^s} \left(\frac{\frac{1}{2} \left(\frac{R}{r} \right)^3 + \frac{1-2\nu^s}{1+\nu^s}}{\left(\frac{R}{r^c} \right)^3 - 1} \right) P_i \quad (22)$$

$$u_r^c = -\frac{r}{3K^c} P_i = -\frac{r(1-2\nu^c)}{Y^c} P_i \quad (23)$$

where K , Y , and ν are the bulk modulus, Young's modulus, and Poisson's ratio, respectively. The superscripts, c and s , are core and shell, respectively. Using the correlation between the strain and the displacement in the spherical coordinate, we obtain

$$e_{\theta\theta} = e_{\phi\phi} = \frac{u_r}{r} \quad (24)$$

and

$$e_{rr} = \frac{du_r}{dr} \quad (25)$$

Therefore, the strain of the core is

$$e_{rr}^c = e_{\theta\theta}^c = e_{\phi\phi}^c = -\frac{(1-2\nu^c)}{Y^c} P_i \quad (26)$$

and the radial and tangential strain of the shell is

$$e_{rr}^s = \frac{(1+\nu^s)}{Y^s} \left(\frac{-\left(\frac{R}{r} \right)^3 + \frac{1-2\nu^s}{1+\nu^s}}{\left(\frac{R}{r^c} \right)^3 - 1} \right) P_i \quad (27)$$

$$e_{\theta\theta}^s = e_{\phi\phi}^s = \frac{(1+\nu^s)}{Y^s} \left(\frac{\frac{1}{2} \left(\frac{R}{r} \right)^3 + \frac{1-2\nu^s}{1+\nu^s}}{\left(\frac{R}{r^c} \right)^3 - 1} \right) P_i \quad (28)$$

P_i is obtained using the boundary condition that the lattice is continuous at the hetero-interface. Therefore, the differences of the tangential strain of the core and shell accounts for the lattice mismatch (ε),

$$e_{\theta\theta}^s - e_{\theta\theta}^c = \varepsilon \quad (29)$$

where $\varepsilon = (a^{\text{CdS}} - a^{\text{ZnS}}) / a^{\text{ZnS}}$ for CdS/ZnS. a^{CdS} and a^{ZnS} are the lattice parameter for zinc blende CdS and ZnS, respectively. Therefore,

$$P_1 = \frac{2Y^c Y^s \varepsilon \left[\left(\frac{R}{r^c} \right)^3 - 1 \right]}{[2Y^s(1-2\nu^c) + Y^c(1+\nu^s)] \left(\frac{R}{r^c} \right)^3 - 2[Y^s(1-2\nu^c) - Y^c(1-2\nu^s)]} \quad (30)$$

The elastic constants used in the calculation are the Reuss-Voigt-Hill average of zinc blende crystal structure as summarized in Table 7.^{83,179,180}

Table 7. Parameters Used for the Calculation of Strain Profile.

| Radius (nm) | Young's modulus (GPa) | Poisson's ratio | Lattice parameter (Å) | Lattice mismatch |
|-------------|-----------------------|-----------------|-------------------------|-----------------------|
| $r^c = 1.8$ | $Y^c = 48.5$ | $\nu^c = 0.369$ | $a^{\text{CdS}} = 5.82$ | $\varepsilon = 0.076$ |
| $R = 3.6$ | $Y^s = 82.8$ | $\nu^s = 0.321$ | $a^{\text{ZnS}} = 5.41$ | |

Extraction of 0-0 Energy (E_{0-0}) of Mn Luminescence. The E_{0-0} of Mn luminescence is extracted via fitting the spectral lineshape to the thermally-averaged Franck-Condon factor,⁸⁷⁸⁷

$$L(E) = A \sum_{n=-\infty}^{\infty} \exp \left[-S \coth \left(\frac{\hbar\omega}{2kT} \right) + \frac{n\hbar\omega}{2kT} \right] J_n(z) \delta(E_{0-0} - n\hbar\omega - E) \quad (31)$$

where A is a constant for normalizing the spectral amplitude, ω is the frequency of the vibrational mode coupled to ${}^4T_1 \rightarrow {}^6A_1$ transition of Mn^{2+} ions, and S , k , T , and E are Huang-Rhys factor, Boltzmann factor, temperature, and photon energy. n is an integer from $-\infty$ to $+\infty$. $J_n(z)$ is the Bessel function of the first kind with imaginary argument where $z = S \operatorname{csch}\left(\frac{\hbar\omega}{2kT}\right)$. Since $L(E) \neq 0$ only when $\delta(E_{0-0} - n\hbar\omega - E) = 1$. Eq 31 is simplified to

$$L(E) = A \exp\left[-S \coth\left(\frac{\hbar\omega}{2kT}\right) + \frac{E_{0-0}-E}{2kT}\right] J_n(z) \quad (32)$$

where n is replaced by $\frac{(E_{0-0}-E)}{\hbar\omega}$ and E is continuous.

Here, ω for each sample is obtained from the fit of the temperature-dependent bandwidth, as discussed in the main text. Using the calculated ω and the bandwidth at 5 K, $\Gamma(5\text{ K})$, S is obtained using eq 2 as summarized in Table 8. All the Mn luminescence spectra are fit to eq 32 with constant ω and S to obtain E_{0-0} . Figure 47 shows examples of the fit with the Mn luminescence spectral lineshape.

Table 8. Parameters Used for the Fit of E_{0-0} .

| sample | d (monolayer) | $\langle n_{\text{Mn}} \rangle$ | ω (cm^{-1}) | S |
|--------------|-----------------|---------------------------------|-------------------------------|-----|
| a1 | 0 | 5.3 | 238 | 9.0 |
| b1 | 2 | 6.1 | 322 | 6.6 |
| c1 | 4 | 6.4 | 387 | 4.9 |
| a3 | 0 | 20 | 229 | 9.8 |
| b3 | 2 | 24 | 282 | 8.4 |
| c3 | 4 | 21 | 327 | 7.1 |
| Mn-doped ZnS | | 17 | 303 | 4.9 |

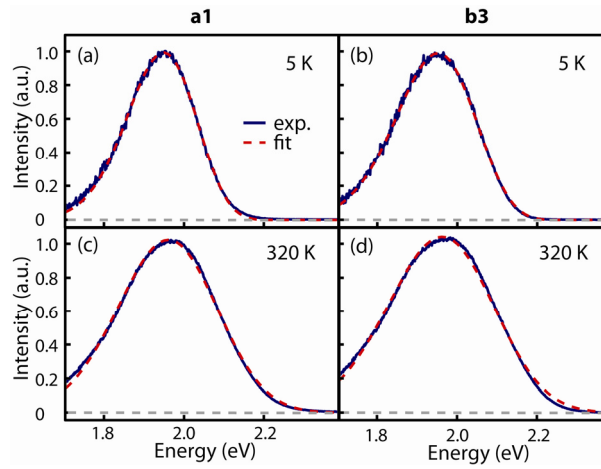


Figure 47. Comparison of Mn luminescence spectral lineshape (solid lines) and the fit (dashed lines) using eq 32. (a) and (c) are taken at 5 and 320 K of sample **a1**, respectively. (b) and (d) are taken at 5 and 320 K of sample **b3**, respectively.

CHAPTER VIII

SUMMARY

8.1 Exciton-Mn Energy Transfer Dynamics

Mn-doped II-VI semiconductor nanocrystals are interesting in their bright dopant luminescence and magnetic properties after exciton-Mn energy transfer and the formation of exciton magnetic polaron. Both processes are mediated by the strong exciton-Mn exchange interaction benefiting from the confinement of exciton in the nanocrystals that stops the migration of excitons and increases the exciton-Mn exciton wavefunction overlap. Although the two processes occur very quickly (few to tens of ps and ~ 200 ps, respectively), non-radiative relaxation processes such as the hole trapping process occurring at a similar timescale are still in competition. Optimization of the rate of energy transfer and formation of exciton magnetic polaron is critical for increasing the yield of the two processes. This could be achieved by increasing the exciton-Mn wavefunction overlap.

The effect of exciton-Mn wavefunction overlap on the dynamics of energy transfer was studied via pump-probe transient absorption technique in radial doping location-controlled Mn-doped CdS/ZnS core/shell nanocrystals. The degree of exciton-Mn wavefunction overlap was varied by changing the radial doping locations in the CdS/ZnS nanocrystals with the same core size and shell thickness. (Figure 25) As the radial doping locations of the Mn^{2+} ions are changed from the core/shell interface toward the surface of the nanocrystals, the exciton-dopant overlap becomes smaller and the

energy transfer rates are expected to decrease. The energy transfer rate was obtained by comparing the exciton dynamics of undoped and Mn-doped nanocrystals. An extra relaxation rate constant extracted after introducing the dopants was assigned to the energy transfer. At each doping radius, a nearly linear correlation of energy transfer rate constant and doping concentration is obtained. (Figure 31) With increasing doping radius by 1.2 nm, the energy transfer rate decreases by ~6 times in the samples studied here. The energy transfer yield obtained from the branching ratio of the energy transfer and the competing process (hole trapping) also decreases. Combining the energy transfer yield and the apparent Mn luminescence quantum yield, we obtained the highest Mn radiative quantum yield is ~95% in the samples studied.

To further demonstrate the effect of exciton-Mn wavefunction overlap on the energy transfer rate, the size of the nanocrystals was varied while the radial doping radius was fixed. The result indicates the energy transfer rate is higher in the smaller nanocrystals.

8.2 Hole Trapping Dynamics

Hole trapping to the surface or interior defects is a major issue in using the undoped and Mn-doped II-VI semiconductor nanocrystals because trapping competes with processes such as exciton luminescence and energy transfer in undoped and Mn-doped nanocrystals, respectively. However, hole trapping dynamics is relatively difficult to study due to the spectroscopic feature of the hole is mixed with the electron. In the exciton dynamics probed at bandedge in Mn-doped nanocrystals, although the dynamics

represents the electron dynamics, hole trapping rate constant (k_{trap}) can be conveniently obtained using the branching ratio of energy transfer (r_{ET}) and hole trapping (r_{trap}) following the correlation: $k_{\text{trap}}/k_{\text{ET}} = r_{\text{trap}}/r_{\text{ET}}$. The obtained hole trapping time is 50-100 ps in Mn-doped nanocrystal studied here.

8.3 Hot Electron Generation after Multiple Exciton-Mn Energy Transfers

Opposite to the bright Mn luminescence after one exciton-Mn energy transfer, Mn emission could be quenched if multiple exciton-Mn energy transfers to the same Mn^{2+} ion during the Mn luminescence lifetime. This phenomenon was studied through the intensity of Mn luminescence vs. excitation density using <100 fs pulse excitation. Mn luminescence intensity was the highest at ~ 3 exciton/nanocrystals. The intensity decreases when further increasing the excitation density due to the extra excitons' capability of transferring the energy to the already excited Mn^{2+} ion. The d electron of the Mn^{2+} ion is excited to the conduction band and relaxes through a non-radiative pathway. Quenching of Mn luminescence by direct optical excitation of the excited Mn^{2+} ion is ruled out due to the excitation duration (<100 fs) being much shorter than energy transfer. We also ruled out the possibility of the two excited Mn^{2+} ions annihilate each other from the independence of Mn luminescence lifetime on the excitation density. The highly excited electron has shown higher photocatalytic efficiency than the electron in undoped nanocrystals, demonstrating another potential application of Mn-doped nanocrystals.

8.4 Strain Effect on the Temperature-Dependence of Mn Luminescence Spectrum

The temperature dependence of Mn luminescence spectral characteristics (peak position and bandwidth) in Mn-doped CdS/ZnS core/shell nanocrystals is tunable via controlled local lattice strain at the dopant site that affects the local vibronic coupling and local thermal expansion. The lattice mismatch at the core/shell interface creates a gradient of lattice strain in the shell along the radial direction that allows varying the local lattice strain at Mn^{2+} site via the controlled radial doping location. Increasing the local lattice strain at Mn^{2+} site results in the stronger temperature-broadening of Mn luminescence bandwidth due to the increasing softening of the vibrational mode coupled to Mn^{2+} ligand field transition. Larger local lattice strain also causes a stronger temperature dependence of the luminescence peak, which indicates the enhanced local thermal expansion at the dopant site.

8.5 Future Works

Here we have shown that the exciton-Mn spatial overlap has great influence on energy transfer rate. On top of this result, individual contribution of hole-Mn and electron-Mn wavefunction overlaps to energy transfer can be studied in Mn-doped type II quantum well structure where the electron and hole wavefunctions are spatially separated. According to the study of exciton-Mn magnetic exchange interaction, hole-Mn exchange coupling is stronger than the electron-Mn exchange coupling. Since exciton-Mn energy transfer also depends on their exchange coupling, one may expect that the hole-Mn exchange coupling is more important to energy transfer. This

assumption can be verified by preparing Mn-doped nanocrystals with type II quantum well structure, such as ZnSe/CdS core/shell nanocrystals where the hole and electron are mainly at the core and shell, respectively. By doping the Mn^{2+} ions in the core or shell, the hole or electron will have more overlap with the dopants than the counterpart. We should expect a higher energy transfer rate in the core-doped nanocrystals with higher hole-Mn wavefunction overlap. By comparing the energy transfer rate with the simulated distribution of exciton wavefunction at the dopant site, the strength of hole-Mn and electron-Mn exchange interaction to energy transfer can be quantified.

Furthermore, host-dopant hole trapping rate can be potentially extracted using the competition with exciton-Mn energy transfer. In chapter V, the intrinsic hole trapping time was extracted using the branching ratio of hole trapping and the energy transfer in the bleach recovery dynamics. By adding hole accepting dopants, such as Cu ions, extra hole traps are introduced. The strategy for extracting the intrinsic hole trapping time can be applied to extract the hole trapping time to Cu. In addition, whether the mechanism for Cu luminescence occurs first with hole trapping to Cu^+ or electron transfer to Cu^{2+} with luminescence also needs to be verified. This can be examined by comparing luminescence quantum yield and exciton dynamics of the Cu/Mn co-doped nanocrystals with the Mn-doped nanocrystals. If the hole trapping to Cu^+ occurs first, the long recovery component of bleach recovery representing the hole trapping population should become larger, and the Mn luminescence quantum yield should become smaller. The hole trapping rate can be calculated using the way that the intrinsic hole trapping time is extracted. On the other hand, if the electron transfer to Cu^{2+} occurs first, the bleach

recovery dynamics and the Mn luminescence quantum yield of the co-doped nanocrystals should be similar to the Mn-doped nanocrystals. The lifetime of Cu luminescence reported in the literature is $10^{-7} - 10^{-5}$ s, which is significantly longer than the exciton-Mn energy transfer time of 10^{-12} - 10^{-10} ps. Therefore, exciton-Mn energy transfer should still dominate the exciton relaxation pathway in the co-doped nanocrystals. Cu-doped nanocrystals have shown great flexibility in luminescence color, but the luminescence quantum yield is still relatively low. Understanding the hole-Cu charge transfer time and process correlated with the core/shell structure will be useful in improving the luminescence quantum yield of Cu-doped nanocrystals for future applications.

REFERENCE

- (1) Norris, D. J.; Efros, A. L.; Erwin, S. C. *Science* **2008**, *319*, 1776.
- (2) Erwin, S. C.; Zu, L.; Haftel, M. I.; Efros, A. L.; Kennedy, T. A.; Norris, D. J. *Nature* **2005**, *436*, 91.
- (3) Wei, C.; Jin, Z. Z.; Alan, G. J. *J. Nanosci. Nanotechnol.* **2004**, *4*, 919.
- (4) Beaulac, R.; Archer, P. I.; Gamelin, D. R. *J. Solid State Chem.* **2008**, *181*, 1582.
- (5) Godlewski, M.; Yatsunenko, S.; Nadolska, A.; Opalinska, A.; Lojkowski, W.; Drozdowicz-Tomsia, K.; Goldys, E. M. *Opt. Mater.* **2009**, *31*, 490.
- (6) Beaulac, R.; Archer, P. I.; van Rijssel, J.; Meijerink, A.; Gamelin, D. R. *Nano Lett.* **2008**, *8*, 2949.
- (7) Sarma, D. D.; Viswanatha, R.; Sapra, S.; Prakash, A.; Garcia-Hernandez, M. J. *Nanosci. Nanotechnol.* **2005**, *5*, 1503.
- (8) Yang, H.; Santra, S.; Holloway, P. H. *J. Nanosci. Nanotechnol.* **2005**, *5*, 1364.
- (9) Archer, P. I.; Santangelo, S. A.; Gamelin, D. R. *Nano Lett.* **2007**, *7*, 1037.
- (10) Bacher, G.; Schomig, H.; Welsch, M. K.; Zaitsev, S.; Kulakovskii, V. D.; Forchel, A.; Lee, S.; Dobrowolska, M.; Furdyna, J. K.; Konig, B.; Ossau, W. *Appl. Phys. Lett.* **2001**, *79*, 524.
- (11) Bacher, G.; Schömig, H.; Scheibner, M.; Forchel, A.; Maksimov, A. A.; Chernenko, A. V.; Dorozhkin, P. S.; Kulakovskii, V. D.; Kennedy, T.; Reinecke, T. L. *Physica E* **2005**, *26*, 37.
- (12) Bussian, D. A.; Crooker, S. A.; Yin, M.; Brynda, M.; Efros, A. L.; Klimov, V. I. *Nat Mater* **2009**, *8*, 35.
- (13) Bryan, J. D.; Heald, S. M.; Chambers, S. A.; Gamelin, D. R. *J. Am. Chem. Soc.* **2004**, *126*, 11640.
- (14) Murase, N.; Jagannathan, R.; Kanematsu, Y.; Watanabe, M.; Kurita, A.; Hirata, K.; Yazawa, T.; Kushida, T. *J. Phys. Chem. B* **1999**, *103*, 754.
- (15) Pradhan, N.; Peng, X. *J. Am. Chem. Soc.* **2007**, *129*, 3339.

- (16) Jones, M.; Lo, S. S.; Scholes, G. D. *Proc. Natl. Acad. Sci.* **2009**, *106*, 3011.
- (17) Tyagi, P.; Kambhampati, P. *J. Chem. Phys.* **2011**, *134*, 094706.
- (18) Vlaskin, V. A.; Janssen, N.; van Rijssel, J.; Beaulac, R. m.; Gamelin, D. R. *Nano Lett.* **2010**, *10*, 3670.
- (19) Hsia, C.-H.; Wuttig, A.; Yang, H. *ACS Nano* **2011**, *5*, 9511.
- (20) McLaurin, E. J.; Vlaskin, V. A.; Gamelin, D. R. *J. Am. Chem. Soc.* **2011**, *133*, 14978.
- (21) Xie, R.; Peng, X. *J. Am. Chem. Soc.* **2009**, *131*, 10645.
- (22) Srivastava, B. B.; Jana, S.; Pradhan, N. *J. Am. Chem. Soc.* **2011**, *133*, 1007.
- (23) Viswanatha, R.; Brovelli, S.; Pandey, A.; Crooker, S. A.; Klimov, V. I. *Nano Lett.* **2011**, *11*, 4753.
- (24) Jana, S.; Srivastava, B. B.; Acharya, S.; Santra, P. K.; Jana, N. R.; Sarma, D. D.; Pradhan, N. *Chem. Commun.* **2010**, *46*, 2853.
- (25) Meulenbergh, R. W.; van Buuren, T.; Hanif, K. M.; Willey, T. M.; Strouse, G. F.; Terminello, L. J. *Nano Lett.* **2004**, *4*, 2277.
- (26) Sahu, A.; Kang, M. S.; Kompch, A.; Notthoff, C.; Wills, A. W.; Deng, D.; Winterer, M.; Frisbie, C. D.; Norris, D. J. *Nano Lett.* **2012**, *12*, 2587.
- (27) Gould, C.; Slobodskyy, A.; Supp, D.; Slobodskyy, T.; Grabs, P.; Hawrylak, P.; Qu, F.; Schmidt, G.; Molenkamp, L. W. *Phys. Rev. Lett.* **2006**, *97*, 017202.
- (28) Maksimov, A. A.; Bacher, G.; McDonald, A.; Kulakovskii, V. D.; Forchel, A.; Becker, C. R.; Landwehr, G.; Molenkamp, L. W. *Phys. Rev. B* **2000**, *62*, R7767.
- (29) Schömig, H.; Bacher, G.; Forchel, A.; Lee, S.; Dobrowolska, M.; Furdyna, J. K. *J. Supercond.* **2003**, *16*, 379.
- (30) Bhattacharjee, A. K.; à la Guillaume, C. B. *Phys. Rev. B* **1997**, *55*, 10613.
- (31) Awschalom, D. D.; Warnock, J.; von Molnár, S. *Phys. Rev. Lett.* **1987**, *58*, 812.

- (32) Bacher, G.; Welsch, M. K.; Forchel, A.; Lyanda-Geller, Y.; Reinecke, T. L.; Becker, C. R.; Molenkamp, L. W. *J. Appl. Phys.* **2008**, *103*, 113520.
- (33) Beaulac, R.; Schneider, L.; Archer, P. I.; Bacher, G.; Gamelin, D. R. *Science* **2009**, *325*, 973.
- (34) Reshina, I. I.; Ivanov, S. V.; Mirlin, D. N.; Sedova, I. V.; Sorokin, S. V. *Phys. Rev. B* **2006**, *74*, 235324.
- (35) Toropov, A. A.; Terent'ev, Y. V.; Sorokin, S. V.; Ivanov, S. V.; Koyama, T.; Nishibayashi, K.; Murayama, A.; Oka, Y.; Bergman, J. P.; Buyanova, I. A.; Chen, W. M.; Monemar, B. *Phys. Rev. B* **2006**, *73*, 245335.
- (36) Vlaskin, V. A.; Beaulac, R. m.; Gamelin, D. R. *Nano Lett.* **2009**, *9*, 4376.
- (37) Chen, H.-Y.; Maiti, S.; Son, D. H. *ACS Nano* **2012**, *6*, 583.
- (38) Alivisatos, A. P. *J. Phys. Chem.* **1996**, *100*, 13226.
- (39) El-Sayed, M. A. *Acc. Chem. Res.* **2004**, *37*, 326.
- (40) Sewall, S. L.; Cooney, R. R.; Anderson, K. E. H.; Dias, E. A.; Kambhampati, P. *Phys. Rev. B* **2006**, *74*, 235328.
- (41) Ekimov, A. I.; Hache, F.; Schanne-Klein, M. C.; Ricard, D.; Flytzanis, C.; Kudryavtsev, I. A.; Yazeva, T. V.; Rodina, A. V.; Efros, A. L. *J. Opt. Soc. Am. B* **1993**, *10*, 100.
- (42) Kambhampati, P. *Acc. Chem. Res.* **2010**, *44*, 1.
- (43) Burda, C.; Chen, X.; Narayanan, R.; El-Sayed, M. A. *Chem. Rev.* **2005**, *105*, 1025.
- (44) Klimov, V. I. *J. Phys. Chem. B* **2000**, *104*, 6112.
- (45) Guyot-Sionnest, P.; Shim, M.; Matranga, C.; Hines, M. *Phys. Rev. B* **1999**, *60*, R2181.
- (46) Sewall, S. L.; Cooney, R. R.; Anderson, K. E. H.; Dias, E. A.; Sagar, D. M.; Kambhampati, P. *J. Chem. Phys.* **2008**, *129*, 084701.
- (47) Chuang, C.-H.; Burda, C. *J. Phys. Chem. Lett.* **2012**, *3*, 1921.
- (48) Pandey, A.; Guyot-Sionnest, P. *Science* **2008**, *322*, 929.

- (49) Burda, C.; Link, S.; Mohamed, M. B.; El-Sayed, M. *J. Chem. Phys.* **2002**, *116*, 3828.
- (50) Klimov, V. I.; Schwarz, C. J.; McBranch, D. W.; Leatherdale, C. A.; Bawendi, M. G. *Phys. Rev. B* **1999**, *60*, R2177.
- (51) Knowles, K. E.; McArthur, E. A.; Weiss, E. A. *ACS Nano* **2011**, *5*, 2026.
- (52) Boulesbaa, A.; Huang, Z.; Wu, D.; Lian, T. *J. Phys. Chem. C* **2010**, *114*, 962.
- (53) McArthur, E. A.; Morris-Cohen, A. J.; Knowles, K. E.; Weiss, E. A. *J. Phys. Chem. B* **2010**, *114*, 14514.
- (54) Guyot-Sionnest, P.; Hines, M. A. *Appl. Phys. Lett.* **1998**, *72*, 686.
- (55) Pandey, A.; Guyot-Sionnest, P. *J. Chem. Phys.* **2007**, *127*, 104710.
- (56) Bhargava, R. N.; Gallagher, D.; Hong, X.; Nurmikko, A. *Phys. Rev. Lett.* **1994**, *72*, 416.
- (57) Gallagher, D.; Héady, W. E.; Racz, J. M.; Bhargava, R. N. *J. Mater. Res.* **1995**, *10*, 870.
- (58) Mikulec, F. V.; Kuno, M.; Bennati, M.; Hall, D. A.; Griffin, R. G.; Bawendi, M. G. *J. Am. Chem. Soc.* **2000**, *122*, 2532.
- (59) Norris, D. J.; Yao, N.; Charnock, F. T.; Kennedy, T. A. *Nano Lett.* **2001**, *1*, 3.
- (60) Dalpian, G. M.; Chelikowsky, J. R. *Phys. Rev. Lett.* **2006**, *96*, 226802.
- (61) Pradhan, N.; Goorskey, D.; Thessing, J.; Peng, X. *J. Am. Chem. Soc.* **2005**, *127*, 17586.
- (62) Azad Malik, M.; O'Brien, P.; Revaprasadu, N. *J. Mater. Chem.* **2001**, *11*, 2382.
- (63) Hanif, K. M.; Meulenberg, R. W.; Strouse, G. F. *J. Am. Chem. Soc.* **2002**, *124*, 11495.
- (64) Beaulac, R.; Archer, P. I.; Ochsenein, S. T.; Gamelin, D. R. *Adv. Funct. Mater.* **2008**, *18*, 3873.
- (65) Zheng, J.; Yuan, X.; Ikezawa, M.; Jing, P.; Liu, X.; Zheng, Z.; Kong, X.; Zhao, J.; Masumoto, Y. *J. Phys. Chem. C* **2009**, *113*, 16969.

- (66) Zuo, T.; Sun, Z.; Zhao, Y.; Jiang, X.; Gao, X. *J. Am. Chem. Soc.* **2010**, *132*, 6618.
- (67) Yang, Y.; Chen, O.; Angerhofer, A.; Cao, Y. C. *J. Am. Chem. Soc.* **2006**, *128*, 12428.
- (68) Thakar, R.; Chen, Y.; Snee, P. T. *Nano Lett.* **2007**, *7*, 3429.
- (69) Yang, Y.; Chen, O.; Angerhofer, A.; Cao, Y. C. *J. Am. Chem. Soc.* **2008**, *130*, 15649.
- (70) Yang, Y.; Chen, O.; Angerhofer, A.; Cao, Y. C. *Chem. Eur. J.* **2009**, *15*, 3186.
- (71) Son, D. H.; Hughes, S. M.; Yin, Y.; Paul Alivisatos, A. *Science* **2004**, *306*, 1009.
- (72) Robinson, R. D.; Sadtler, B.; Demchenko, D. O.; Erdonmez, C. K.; Wang, L.-W.; Alivisatos, A. P. *Science* **2007**, *317*, 355.
- (73) Li, H.; Brescia, R.; Krahn, R.; Bertoni, G.; Alcocer, M. J. P.; D'Andrea, C.; Scotognella, F.; Tassone, F.; Zanella, M.; De Giorgi, M.; Manna, L. *ACS Nano* **2012**, *6*, 1637.
- (74) Mocatta, D.; Cohen, G.; Schattner, J.; Millo, O.; Rabani, E.; Banin, U. *Science* **2011**, *332*, 77.
- (75) Eilers, J.; Groeneveld, E.; de Mello Donegá, C.; Meijerink, A. *J. Phys. Chem. Lett.* **2012**, *3*, 1663.
- (76) Wark, S. E.; Hsia, C.-H.; Son, D. H. *J. Am. Chem. Soc.* **2008**, *130*, 9550.
- (77) Miszta, K.; Dorfs, D.; Genovese, A.; Kim, M. R.; Manna, L. *ACS Nano* **2011**, *5*, 7176.
- (78) Ishizumi, A.; Jojima, E.; Yamamoto, A.; Kanemitsu, Y. *J. Phys. Soc. Jpn.* **2008**, *77*, 053705.
- (79) Gan, C.; Zhang, Y.; Battaglia, D.; Peng, X.; Xiao, M. *Appl. Phys. Lett.* **2008**, *92*, 241111.
- (80) Bawendi, M. G.; Carroll, P. J.; Wilson, W. L.; Brus, L. E. *J. Chem. Phys.* **1992**, *96*, 946.
- (81) Pradhan, N.; Battaglia, D. M.; Liu, Y.; Peng, X. *Nano Lett.* **2006**, *7*, 312.

- (82) Pierres, A.; Benoliel, A. M.; Bongrand, P.; Ronda, C. R.; Amrein, T. *J. Lumin.* **1996**, *69*, 245.
- (83) Ithurria, S.; Guyot-Sionnest, P.; Mahler, B.; Dubertret, B. *Phys. Rev. Lett.* **2007**, *99*, 265501.
- (84) Suyver, J. F.; Wuister, S. F.; Kelly, J. J.; Meijerink, A. *Phys. Chem. Chem. Phys.* **2000**, *2*, 5445.
- (85) Leslie, T. C.; Allen, J. W. *Phys. Status Solidi A* **1981**, *65*, 545.
- (86) Dexter, D. L. *J. Chem. Phys.* **1953**, *21*, 836.
- (87) Henderson, B.; Imbusch, G. F., *Optical Spectroscopy of Inorganic Solids*. Oxford University Press Inc.: New York, 1989.
- (88) Kushida, T. *J. Phys. Soc. Jpn.* **1973**, *34*, 1318.
- (89) Hefetz, Y.; Goltsos, W. C.; Nurmikko, A. V.; Kolodziejski, L. A.; Gunshor, R. L. *Appl. Phys. Lett.* **1986**, *48*, 372.
- (90) Leinen, D. *Phys. Rev. B* **1997**, *55*, 6975.
- (91) Seufert, J.; Bacher, G.; Scheibner, M.; Forchel, A.; Lee, S.; Dobrowolska, M.; Furdyna, J. K. *Phys. Rev. Lett.* **2001**, *88*, 027402.
- (92) Shibata, K.; Nakayama, E.; Souma, I.; Murayama, A.; Oka, Y. *Phys. Status Solidi B* **2002**, *229*, 473.
- (93) Chung, J. H.; Ah, C. S.; Jang, D.-J. *J. Phys. Chem. B* **2001**, *105*, 4128.
- (94) Olano, E. M.; Grant, C. D.; Norman, T. J.; Castner, E. W.; Zhang, J. Z. *J. Nanosci. Nanotechnol.* **2005**, *5*, 1492.
- (95) Chen, H.-Y.; Chen, T.-Y.; Son, D. H. *J. Phys. Chem. C* **2010**, *114*, 4418.
- (96) Yu, W. W.; Peng, X. *Angew. Chem. Int. Ed.* **2002**, *41*, 2368.
- (97) Peng, Z. A.; Peng, X. *J. Am. Chem. Soc.* **2000**, *123*, 183.
- (98) Srivastava, B. B.; Jana, S.; Karan, N. S.; Paria, S.; Jana, N. R.; Sarma, D. D.; Pradhan, N. *J. Phys. Chem. Lett.* **2010**, *1*, 1454.
- (99) Wood, V.; Halpert, J. E.; Panzer, M. J.; Bawendi, M. G.; Bulović, V. *Nano Lett.* **2009**, *9*, 2367.

- (100) Melhuish, W. H. *J. Phys. Chem.* **1961**, *65*, 229.
- (101) Karstens, T.; Kobs, K. *J. Phys. Chem.* **1980**, *84*, 1871.
- (102) Jones, G.; Jackson, W. R.; Choi, C. Y.; Bergmark, W. R. *J. Phys. Chem.* **1985**, *89*, 294.
- (103) Isak, S. J.; Eyring, E. M. *J. Phys. Chem.* **1992**, *96*, 1738.
- (104) Lakowicz, J. R., *Principles of Fluorescence Spectroscopy*. 3rd ed.; Springer: New York, 2006.
- (105) Leatherdale, C. A.; Woo, W. K.; Mikulec, F. V.; Bawendi, M. G. *J. Phys. Chem. B* **2002**, *106*, 7619.
- (106) Bol, A. A.; Meijerink, A. *Phys. Rev. B* **1998**, *58*, R15997.
- (107) Nawrocki, M.; Rubo, Y. G.; Lascaray, J. P.; Coquillat, D. *Phys. Rev. B* **1995**, *52*, R2241.
- (108) Vink, A. P.; de Bruin, M. A.; Roke, S.; Peijzel, P. S.; Meijerink, A. *J. Electrochem. Soc.* **2001**, *148*, E313.
- (109) Klimov, V. I.; McBranch, D. W. *Phys. Rev. Lett.* **1998**, *80*, 4028.
- (110) Zhang, J. Z. *J. Phys. Chem. B* **2000**, *104*, 7239.
- (111) Ueda, A.; Tayagaki, T.; Kanemitsu, Y. *J. Phys. Soc. Jpn.* **2009**, *78*, 083706.
- (112) Klimov, V. I.; McGuire, J. A.; Schaller, R. D.; Rupasov, V. I. *Phys. Rev. B* **2008**, *77*, 195324.
- (113) Barzykin, A. V.; Tachiya, M. *J. Phys.: Condens. Matter* **2007**, 065105.
- (114) Ochsenein, S. T.; Gamelin, D. R. *Nat. Nanotech.* **2011**, *6*, 112.
- (115) Beaulac, R.; Ochsenein, S.; Gamelin, D., Colloidal Transition-Metal-Doped Quantum Dots. In *Nanocrystal Quantum Dots, 2nd Ed.*, Klimov, V. I., Ed. CRC Press: Boca Raton, FL, 2010; pp 397.
- (116) Yu, J. H.; Liu, X.; Kweon, K. E.; Joo, J.; Park, J.; Ko, K. T.; Lee, D. W.; Son, J. S.; Park, J.; Kim, Y.-W.; Hwang, G. S.; Dobrowolska, M.; Furdyna, J. K.; Hyun, T. *Nat. Mater.* **2010**, *9*, 47.

- (117) Magana, D.; Perera, S. C.; Harter, A. G.; Dalal, N. S.; Strouse, G. F. *J. Am. Chem. Soc.* **2006**, *128*, 2931.
- (118) Lee, S.; Dobrowolska, M.; Furdyna, J. K. *Solid State Commun.* **2007**, *141*, 311.
- (119) Chen, D.; Viswanatha, R.; Ong, G. L.; Xie, R.; Balasubramanian, M.; Peng, X. *J. Am. Chem. Soc.* **2009**, *131*, 9333.
- (120) Underwood, D. F.; Kippeny, T.; Rosenthal, S. J. *J. Phys. Chem. B* **2001**, *105*, 436.
- (121) Klimov, V. I. *Annu. Rev. Phys. Chem.* **2007**, *58*, 635.
- (122) Dayal, S.; Burda, C. *J. Am. Chem. Soc.* **2007**, *129*, 7977.
- (123) Gaponenko, S. V., *Optical Properties of Semiconductor Nanocrystals*. Cambridge University Press: Cambridge, 1999.
- (124) Chen, W.; Sammynaiken, R.; Huang, Y.; Malm, J.-O.; Wallenberg, R.; Bovin, J.-O.; Zwiller, V.; Kotov, N. A. *J. Appl. Phys.* **2001**, *89*, 1120.
- (125) Zhu, X. Y. *Annu. Rev. Phys. Chem.* **1994**, *45*, 113.
- (126) Park, J. Y.; Somorjai, G. A. *J. Vac. Sci. Technol., B* **2006**, *24*, 1967.
- (127) Brus, L. *Acc. Chem. Res.* **2008**, *41*, 1742.
- (128) Gadzuk, J. W. *Phys. Rev. Lett.* **1996**, *76*, 4234.
- (129) Gaillard, F.; Sung, Y.-E.; Bard, A. J. *J. Phys. Chem. B* **1999**, *103*, 667.
- (130) Bonn, M.; Funk, S.; Hess, C.; Denzler, D. N.; Stampfl, C.; Scheffler, M.; Wolf, M.; Ertl, G. *Science* **1999**, *285*, 1042.
- (131) Nozik, A. J. *Annu. Rev. Phys. Chem.* **2001**, *52*, 193.
- (132) Ross, R. T.; Nozik, A. J. *J. Appl. Phys.* **1982**, *53*, 3813.
- (133) Anderson, N. A.; Lian, T. *Annu. Rev. Phys. Chem.* **2005**, *56*, 491.
- (134) Tisdale, W. A.; Williams, K. J.; Timp, B. A.; Norris, D. J.; Aydil, E. S.; Zhu, X. Y. *Science* **2010**, *328*, 1543.
- (135) Pandey, A.; Guyot-Sionnest, P. *J. Phys. Chem. Lett.* **2010**, *1*, 45.

- (136) Huang, J.; Huang, Z.; Yang, Y.; Zhu, H.; Lian, T. *J. Am. Chem. Soc.* **2010**, *132*, 4858.
- (137) Schmidt, M. E.; Blanton, S. A.; Hines, M. A.; Guyot-Sionnest, P. *Phys. Rev. B* **1996**, *53*, 12629.
- (138) Son, D. H.; Wittenberg, J. S.; Alivisatos, A. P. *Phys. Rev. Lett.* **2004**, *92*, 127406.
- (139) Chon, J. W. M.; Gu, M.; Bullen, C.; Mulvaney, P. *Appl. Phys. Lett.* **2004**, *84*, 4472.
- (140) Irvine, S.; Staudt, T.; Rittweger, E.; Engelhardt, J.; Hell, S. *Angew. Chem. Int. Ed.* **2008**, *47*, 2685.
- (141) Dreyhsig, J.; Allen, J. W. *J. Phys.: Condens. Matter* **1989**, *1*, 1087.
- (142) Taniguchi, M.; Fujimori, M.; Fujisawa, M.; Mori, T.; Souma, I.; Oka, Y. *Solid State Commun.* **1987**, *62*, 431.
- (143) Nazir, S.; Ikram, N.; Tanveer, M.; Shaukat, A.; Saeed, Y.; Reshak, A. H. *J. Phys. Chem. A* **2009**, *113*, 6022.
- (144) Norberg, N. S.; Kittilstved, K. R.; Amonette, J. E.; Kukkadapu, R. K.; Schwartz, D. A.; Gamelin, D. R. *J. Am. Chem. Soc.* **2004**, *126*, 9387.
- (145) Kushida, T.; Tanaka, Y.; Oka, Y. *Solid State Commun.* **1974**, *14*, 617.
- (146) Chen, T.-Y.; Hsia, C.-H.; Son, D. H. *J. Phys. Chem. C* **2008**, *112*, 10125.
- (147) Fisher, B.; Caruge, J.-M.; Chan, Y.-T.; Halpert, J.; Bawendi, M. G. *Chem. Phys.* **2005**, *318*, 71.
- (148) Asbury, J. B.; Hao, E.; Wang, Y.; Ghosh, H. N.; Lian, T. *J. Phys. Chem. B* **2001**, *105*, 4545.
- (149) Sheps, L.; Crowther, A. C.; Elles, C. G.; Crim, F. F. *J. Phys. Chem. A* **2005**, *109*, 4296.
- (150) Mills, A.; Wang, J. *J. Photochem. Photobiol., A* **1999**, *127*, 123.
- (151) Costi, R.; Saunders, A. E.; Elmalem, E.; Salant, A.; Banin, U. *Nano Lett.* **2008**, *8*, 637.
- (152) Huang, Y.; Sun, F.; Wang, H.; He, Y.; Li, L.; Huang, Z.; Wu, Q.; Yu, J. C. *J. Mater. Chem.* **2009**, *19*, 6901.

- (153) Fang, F.; Chen, L.; Chen, Y.-B.; Wu, L.-M. *J. Phys. Chem. C* **2010**, *114*, 2393.
- (154) Hall, A. R.; Falvo, M. R.; Superfine, R.; Washburn, S. *Nat. Nanotech.* **2007**, *2*, 413.
- (155) Lee, J.; Kim, H.; Kahng, S. J.; Kim, G.; Son, Y. W.; Ihm, J.; Kato, H.; Wang, Z. W.; Okazaki, T.; Shinohara, H.; Kuk, Y. *Nature* **2002**, *415*, 1005.
- (156) Lin, X.; He, X. B.; Yang, T. Z.; Guo, W.; Shi, D. X.; Gao, H.-J.; Ma, D. D. D.; Lee, S. T.; Liu, F.; Xie, X. C. *Appl. Phys. Lett.* **2006**, *89*, 043103.
- (157) Smith, A. M.; Mohs, A. M.; Nie, S. *Nat. Nanotech.* **2009**, *4*, 56.
- (158) Balet, L. P.; Ivanov, S. A.; Piryatinski, A.; Achermann, M.; Klimov, V. I. *Nano Lett.* **2004**, *4*, 1485.
- (159) Saada, A. S., *Elasticity theory and applications*. 2nd ed.; Malabar, Fla.: Krieger, 1993.
- (160) Rockenberger, J.; Troger, L.; Rogach, A. L.; Tischer, M.; Grundmann, M.; Eychmuller, A.; Weller, H. *J. Chem. Phys.* **1998**, *108*, 7807.
- (161) Traill, R. J.; Boyle, R. W. *Am. Mineral.* **1955**, *40*, 555.
- (162) Suyver, J. F.; Kelly, J. J.; Meijerink, A. *J. Lumin.* **2003**, *104*, 187.
- (163) Itskovich, E. M.; Ulstrup, J.; Vorotyntsev, M. A., Quantum Theory of Electronic and Vibrational Spectra of Impurity Molecules in Polar Media. In *The Chemical Physics of Solvation. Part B. Spectroscopy of Solvation*, Dogonadze, R. R.; Kalman, E.; Kornyshev, A. A.; Ulstrup, J., Eds. Elsevier: Amsterdam 1986.
- (164) Cortes, J.; Heitele, H.; Jortner, J. *J. Phys. Chem.* **1994**, *98*, 2527.
- (165) McCammon, C. *Phys. Chem. Miner.* **1991**, *17*, 636.
- (166) Chen, W.; Li, G.; Malm, J.-O.; Huang, Y.; Wallenberg, R.; Han, H.; Wang, Z.; Bovin, J.-O. *J. Lumin.* **2000**, *91*, 139.
- (167) Tallman, R. E.; Ritter, T. M.; Weinstein, B. A.; Cantarero, A.; Serrano, J.; Lauck, R.; Cardona, M. *Phys. Status Solidi B* **2004**, *241*, 491.
- (168) Cardona, M.; Kremer, R. K.; Lauck, R.; Siegle, G.; Muñoz, A.; Romero, A. H.; Schindler, A. *Phys. Rev. B* **2010**, *81*, 075207.

- (169) Dinger, A.; Hetterich, M.; Göppert, M.; Grün, M.; Klingshirn, C.; Weise, B.; Liang, J.; Wagner, V.; Geurts, J. *J. Cryst. Growth* **1999**, *200*, 391.
- (170) Guan, Z. P.; Fan, X. W.; Xia, H.; Jiang, S. S. *J. Appl. Phys.* **1995**, *78*, 4270.
- (171) Chen, W.; Su, F.; Li, G.; Joly, A. G.; Malm, J.-O.; Bovin, J.-O. *J. Appl. Phys.* **2002**, *92*, 1950.
- (172) Keil, T. H. *Phys. Rev.* **1965**, *140*, A601.
- (173) MacKay, J. F.; Becker, W. M.; Spaek, J.; Debska, U. *Phys. Rev. B* **1990**, *42*, 1743.
- (174) The shift of Mn luminescence peak position (E) due to thermal expansion is $(\partial E/\partial T)_p = (\partial E/\partial V)_T \cdot (\partial V/\partial T)_p = (\partial E/\partial P)_T \cdot (\partial P/\partial V)_T \cdot (\partial L^3/\partial T)_p$, where P, L, and V are pressure, length, and volume of the material. $(\partial E/\partial P)_T$ is the shift of E in Mn-doped ZnS under hydrostatic pressure, -30.4 meV/GPa from literature. $(\partial P/\partial V)_T$ is $-K \cdot V$, where K is the bulk modulus of ZnS, 77.1 GPa. $(\partial L^3/\partial T)_p = 3L^2 (\partial L/\partial T)_p = 3V/L (\partial L/\partial T)_p$, where $1/L (\partial L/\partial T)_p$ is the change of lattice parameter (-0.11%) in temperature (320-50 K).
- (175) Ashcroft, N. W.; Mermin, N. D., *Solid State Physics*. Holt, Rinehart and Winston: Orlando, FL, 1976.
- (176) Müller, E.; Gebhardt, W. *Phys. Status Solidi B* **1986**, *137*, 259.
- (177) Xue, J.; Ye, Y.; Medina, F.; Martinez, L.; Lopez-Rivera, S. A.; Girit, W. *J. Lumin.* **1998**, *78*, 173.
- (178) Balasubramanian, S.; Ceder, G.; Kolenbrander, K. D. *J. Appl. Phys.* **1996**, *79*, 4132.
- (179) Hill, R. *Proc. Phys. Soc. A* **1952**, *65*, 349.
- (180) Adachi, S., Elastic Properties. In *Properties of Group-IV, III-V and II-VI Semiconductors*, John Wiley & Sons, Ltd: 2005; pp 41.

APPENDIX A

A.1 Summary of Doping Yield

The doping yield of Mn^{2+} ions in the synthesis of Mn-doped CdS/ZnS nanocrystals following the procedures in section 3.1.3 is summarized in this section. The synthesis was done with the CdS core with diameter = 3.6 nm, bandedge absorption = 422-423 nm, and extinction coefficient at bandedge = $330,000 \text{ cm}^{-1} \text{ M}^{-1}$. The $\langle n_{\text{Mn}} \rangle$ calculated for the precursor added to the reaction solution vs $\langle n_{\text{Mn}} \rangle$ for the final Mn-doped CdS/ZnS nanocrystals from ICP-MS are compared below. Table A1 and Figure A1a are for Mn precursor A (oleylamine solution of manganese acetate). The doping yield is $\sim 35\%$. Table A2 and Figure A1b are for Mn precursor B (oleylamine solution of manganese diethyldithiolcarbamate). The doping yield is $\sim 55\%$.

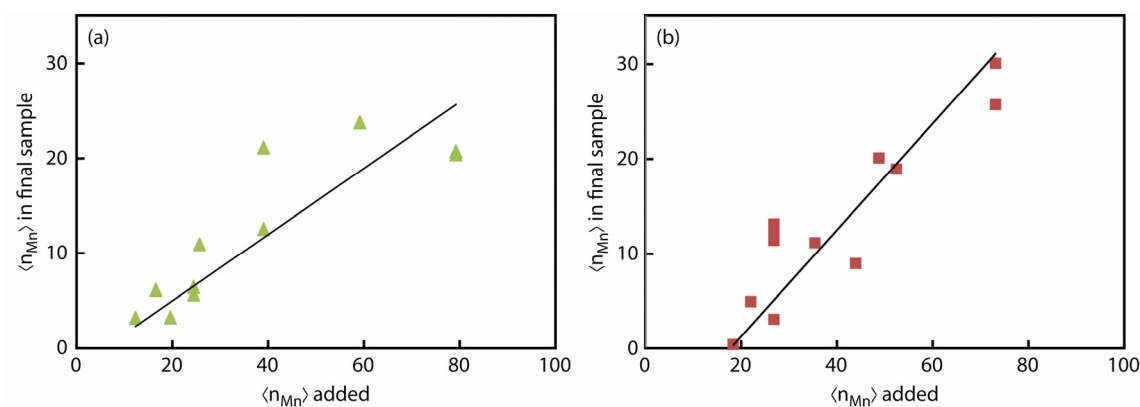


Figure A1. (a), (b) Comparison of $\langle n_{\text{Mn}} \rangle$ added to the synthesis vs the $\langle n_{\text{Mn}} \rangle$ in the final Mn-doped CdS/ZnS nanocrystals for precursor A and B, respectively.

Table A1. Comparison of $\langle n_{\text{Mn}} \rangle$ Added to the Synthesis vs the $\langle n_{\text{Mn}} \rangle$ in the Final Mn-Doped CdS/ZnS Nanocrystals for Precursor A

| Structure ^a | Sample synthesis date (code) | $\langle n_{\text{Mn}} \rangle$ precursor added | $\langle n_{\text{Mn}} \rangle$ from ICP-MS |
|------------------------|------------------------------|---|---|
| 1/1.5 | 090722C1 (I) | 79 | 20.4 |
| 1/1.5 | 090722C2 (H) | 24 | 5.6 |
| 1/1.5 | 090909C (G) | 12 | 3.2 |
| 1/1.5 | 090925C1 (M) | 39 | 21.1 |
| 1/1.5 | 090925C2 (K) | 19 | 3.2 |
| 2/4 | 110608C (P3S) | 16 | 6.1 |
| 2/4 | 110608D (P3U) | 59 | 23.8 |
| 2/4 | 110622D (P3W) | 26 | 10.9 |
| 4/2 | 110514B (P3O) | 24 | 6.4 |
| 4/2 | 110516C (P3P) | 39 | 12.5 |
| 4/2 | 110516D (P3Q) | 79 | 20.7 |

^a Number of monolayers of ZnS before/after doping the Mn²⁺ ions.

Table A2. Comparison of $\langle n_{\text{Mn}} \rangle$ Added to the Synthesis vs the $\langle n_{\text{Mn}} \rangle$ in the Final Mn-Doped CdS/ZnS Nanocrystals for Precursor B

| Structure ^a | Sample synthesis date (code) | $\langle n_{\text{Mn}} \rangle$ precursor added | $\langle n_{\text{Mn}} \rangle$ from ICP-MS |
|------------------------|------------------------------|---|---|
| 0/6 | 110519H (P3N) | 49 | 20 |
| 0/6 | 110520D(P3L) | 27 | 13 |
| 0/6 | 110520F(P3M) | 22 | 4.8 |
| 0/6 | 110516G | 27 | 11.3 |
| 0/6 | 110516H | 73 | 30 |
| 0/6 | 110519C | 27 | 12.2 |
| 0/6 | 110519D | 73 | 25.6 |
| 0/6 | 110519G | 18 | 0.3 |
| 0/2.5 | 100827C1 | 27 | 3.0 |
| 0/2.5 | 100827C2 | 35 | 11.0 |
| 0/2.5 | 100827C3 | 44 | 8.8 |

^a Number of monolayers of ZnS before/after doping the Mn²⁺ ions.

A.2 Summary of Mn Luminescence Lifetime

Mn luminescence lifetime vs $\langle n_{\text{Mn}} \rangle$ of Mn-doped CdS/ZnS nanocrystals with different doping structure is summarized in Figure A2 and listed in Table A3.

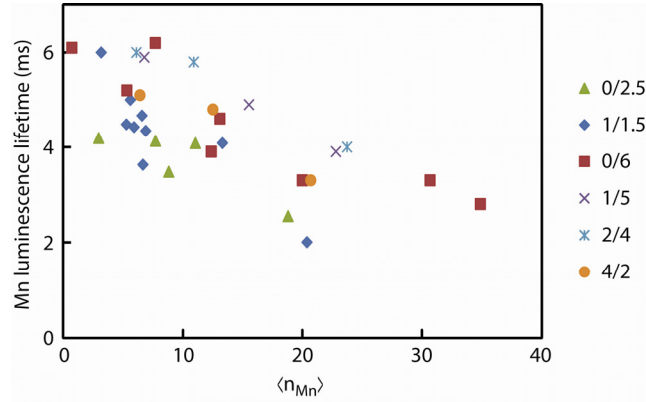


Figure A2. Mn luminescence lifetime vs $\langle n_{\text{Mn}} \rangle$ in Mn-doped CdS/ZnS nanocrystals. The legend indicates the number of monolayers of ZnS before/after doping the Mn²⁺ ions.

Table A3. $\langle n_{\text{Mn}} \rangle$ and Sample Structure-Dependent Mn Luminescence Lifetime in Mn-doped CdS/ZnS Nanocrystals

| Structure | Sample synthesis date (code) | $\langle n_{\text{Mn}} \rangle$ | Lifetime (ms) |
|-----------|------------------------------|---------------------------------|---------------|
| 1/1.5 | 090722C1 (I) | 20.4 | 2.0 |
| 1/1.5 | 090722C2 (H) | 5.6 | 5.0 |
| 1/1.5 | 090909C (G) | 3.2 | 6.0 |
| 1/1.5 | 100901B2 | 5.9 | 4.4 |
| 1/1.5 | 100901C2 | 5.3 | 4.5 |
| 1/1.5 | 100901D2 | 6.6 | 3.6 |
| 1/1.5 | 100904A2 | 6.6 | 4.7 |
| 1/1.5 | 100904B2 | 6.9 | 4.3 |
| 1/1.5 | 100904C2 | 13.3 | 4.1 |
| 0/2.5 | 100827C1 | 3.0 | 4.2 |
| 0/2.5 | 100827C2 | 11.0 | 4.1 |
| 0/2.5 | 100827C3 | 8.8 | 3.5 |
| 0/2.5 | 100827C4 | 18.8 | 2.5 |
| 0/2.5 | 100901A2 | 7.7 | 4.1 |
| 0/2.5 | 100827C3 | 8.8 | 3.5 |
| 0/2.5 | 100827C4 | 18.8 | 2.5 |
| 0/2.5 | 100901A2 | 7.7 | 4.1 |

Table A3. (Continued)

| Structure ^a | Sample synthesis date (code) | $\langle n_{\text{Mn}} \rangle$ | Lifetime (ms) |
|------------------------|------------------------------|---------------------------------|---------------|
| 0/6 | 100720E1 | 0.7 | 6.1 |
| 0/6 | 100720E2 | 12.4 | 3.9 |
| 0/6 | 100720E3 | 30.7 | 3.3 |
| 0/6 | 100720E4 | 66.1 | 1.7 |
| 0/6 | 100726C2 | 7.7 | 6.2 |
| 0/6 | 100726C3 | 34.9 | 2.8 |
| 0/6 | 110519H (P3N) | 20.0 | 3.3 |
| 0/6 | 110520D (P3L) | 5.3 | 5.2 |
| 0/6 | 110520F (P3M) | 13.1 | 4.6 |
| 1/5 | 100720C1 | 6.8 | 5.9 |
| 1/5 | 100720C2 | 15.5 | 4.9 |
| 1/5 | 100720C3 | 22.8 | 3.9 |
| 1/5 | 100720C4 | 78.5 | 2.3 |
| 2/4 | 110608C (P3S) | 6.1 | 6.0 |
| 2/4 | 110608D (P3U) | 23.8 | 4.0 |
| 2/4 | 110622D (P3W) | 10.9 | 5.8 |
| 4/2 | 110514B (P3O) | 6.4 | 5.1 |
| 4/2 | 110516C (P3P) | 12.5 | 4.8 |
| 4/2 | 110516D (P3Q) | 20.7 | 3.3 |

^a Number of monolayers of ZnS before/after doping the Mn²⁺ ions.